MISSION DESIGN APPLICATIONS IN THE EARTH-MOON SYSTEM: TRANSFER TRAJECTORIES AND STATIONKEEPING

A Thesis

Submitted to the Faculty

of

Purdue University

by

Thomas A. Pavlak

In Partial Fulfillment of the

Requirements for the Degree

of

Master of Science in Aeronautics and Astronautics

May 2010

Purdue University

West Lafayette, Indiana

To Mom, Dad, Kay, and Dan

ACKNOWLEDGMENTS

I must first thank my family for the unconditional support that they have always provided. They have been asking me, "How's school going?" for 20 years and I cannot express how much their continuing interest in my education and endless supply of encouraging words mean to me. I would also like to thank my fiancée, Amy, for being an unyielding force of optimism and stability during the course of my graduate studies. In times of self-doubt, she has enough confidence in me for both of us and I consider myself truly blessed.

My advisor, Professor Kathleen Howell, is also owed my deepest gratitude. She is a major reason that Purdue University was my choice for graduate school, and I feel very fortunate to have the opportunity to work with her. Her guidance has been invaluable, and the two projects discussed in this thesis came about as a direct result of her ideas and suggestions. Her enthusiasm for the subject matter cultivates an atmosphere of shared learning among the graduate students in her research group. I would also like to thank my other committee members, Professor James Longuski and Professor Daniel DeLaurentis, for the conversations we have shared during my time at Purdue and for reviewing my thesis. I am grateful to have had the opportunity to work with Professor DeLaurentis and members of his research group during two of my semesters at Purdue as well.

I must also extend my thanks to Daniel Grebow and Martin Ozimek. I have learned a great deal from them and am most appreciative of the help and advice that they have always been more than willing to provide. I have counted them as colleagues, role models, roommates, and friends during my time at Purdue and I sincerely hope that our paths may cross again in the future. Wayne Schlei, Cody Short, and Mar Vaquero must also be acknowledged. We joined Professor Howell's research group together and I have really enjoyed learning and sharing ideas with

them along the way. I am grateful for their friendship and very much look forward to continuing our academic journey together. The entire research group has been a tremendous source of knowledge and support and, for that, I am very thankful as well.

I became involved with the libration point orbit stationkeeping problem while interning at Goddard Space Flight Center during the summer of 2009 and owe a great deal of thanks to my program mentor, David Folta. My work in the manned Earth-Moon transfer problem is the direct result of a collaboration with Professor Belinda Marchand and Sara Scarritt at the University of Texas at Austin, and I thank them for their help and for involving me in the project.

Lastly, I would like to thank Purdue University, the Indiana Space Grant Consortium, Mr. David Folta of the Navigation and Mission Design Branch at Goddard Space Flight Center under NASA Grant Number NNX10AJ24G, and the Jet Propulsion Laboratory under Contract Number 1326038 for providing support during my time at Purdue.

TABLE OF CONTENTS

Page

LIST OF TABLES

LIST OF FIGURES

ABSTRACT

Pavlak, Thomas A. M.S.A.A., Purdue University, May 2010. Mission Design Applications in the Earth-Moon System: Transfer Trajectories and Stationkeeping. Major Professor: Kathleen C. Howell.

A renewed interest in the Moon over the last decade has created a need for robust mission design algorithms in the Earth-Moon system. Strategies for computing orbits within the context of the circular restricted three-body problem as well as higher-fidelity ephemeris models are adapted to fulfill a variety of mission objectives. To support future scientific and communications objectives, periodic and quasi-periodic orbits in the vicinity the collinear L_1 and L_2 libration points in the Earth-Moon system are discussed. Differential corrections algorithms are presented to compute the orbits and to transition them to the higher-fidelity ephemeris models. A control-point stationkeeping strategy is modified to maintain several L_2 libration point orbits and preliminary stationkeeping costs are computed.

As a result of the discovery of water ice at the lunar poles, these regions have emerged as a focus of future manned mission design efforts. The use of the circular restricted three-body problem as a preliminary design tool for this problem is explored. Families of planar and out-of-plane free return trajectories are computed in the three-body model and are included as part of a four-phase bi-elliptic transfer to the lunar poles. A differential corrections scheme to compute multi-burn Earth-Moon transfers in a higher-fidelity ephemeris model is developed as well. This algorithm offers flexibility in the mission design process and is used (i) to reduce total maneuver costs in a baseline trajectory, and (ii) to explore innovative solutions. A long-term goal in this analysis is an improved understanding of the dynamical environment in this region of space.

1. INTRODUCTION

The proximity of the Moon to the Earth has made it an object of interest throughout human existence. From early astronomers who attempted to accurately observe the motion of the Moon, to Newton and other physicists and mathematicians who sought to explain it, there has been an effort for many, many years to improve humanity's understanding of Earth's nearest celestial neighbor. Through dramatic advances in modern rocketry during the first half of the 20th century, led by Goddard, Von Braun, and others [1], the once far-fetched concept of sending a spacecraft to another celestial body became a realistic possibility. On September 12, 1959, the Soviet probe Luna 2 impacted the lunar surface and became the first man-made object to reach the Moon [1]. Nine years later, in December of 1968, the Apollo 8 module became the first manned vehicle to fly in the vicinity of the Moon, clearing the way for the first lunar landing by the Apollo 11 spacecraft on July 20, 1969.

Humans have not walked on the surface of the Moon since 1972, but there has been a renewed interest in manned lunar missions in recent years. Specifically, the lunar poles have emerged as a focus of manned mission design efforts due to the discovery and confirmation of water ice in these regions by the Chandrayaan [2] and the LCROSS [3] missions, respectively. The Earth-Moon transfer trajectories are true multi-body problems due to the fact that the gravitational influences of the Earth and Moon affect the spacecraft motion simultaneously and the solar gravity causes a considerable perturbation force. This multi-body gravitational model adds complexity to the design of Earth-Moon transfers. For example, robust computational schemes that converge rapidly are necessary during preliminary design phases and, in response to contingencies, if abort maneuvers are to be computed instantaneously onboard the spacecraft.

Orbits in the vicinity of the Earth-Moon libration points have also garnered interest in recent years because they can be used as both platforms for scientific observation and as part of a communications network to support manned facilities on the Moon, specifically at the lunar poles. The ISEE-3 spacecraft was launched in 1978 and was delivered to the vicinity of the Sun-Earth L_1 libration point to become the first spacecraft to use a libration point orbit [4]. Since ISEE-3, other scientific missions have also successfully operated near the collinear libration points including WIND [5], SOHO [6], ACE [7], MAP [8], and Genesis [9]. Other libration point missions are scheduled for launch in the coming decade, most notably the James Webb Space Telescope (JWST) which will make deep space observations from an orbit in the vicinity of the Sun-Earth L_2 libration point [10].

While there have been a number of successful Sun-Earth libration point missions, no spacecraft has ever included a libration point orbit as part of the trajectory design in the Earth-Moon system. However, in August of 2010, a spacecraft enters the vicinity of the Earth-Moon L_2 point as part of the Acceleration Reconnection and Turbulence and Electrodynamics of the Moon's Interaction with the Sun (ARTEMIS) mission [11]. ARTEMIS is an extension of the Time History of Events and Macroscale Interactions during Substorms (THEMIS) mission which was launched in 2007. The THEMIS mission consists of five spacecraft in elliptical orbits about Earth which take measurements of the magnetosphere [12]. The ARTEMIS mission originated in July 2009, when two of these spacecraft, termed P_1 and P_2, initiated a series of orbit-raising maneuvers and lunar fly-bys to eventually leave the vicinity of the Earth. Following near Sun-Earth and Earth-Moon manifolds, the two spacecraft arrive in Earth-Moon Lissajous orbits in late summer 2010. Like most libration point orbits, the L_1 and L_2 Lissajous orbits designed for the ARTEMIS mission are inherently unstable and must be maintained. Since both P_1 and P_2 are operating only on fuel remaining from the THEMIS mission, an efficient stationkeeping strategy is required [13].

1.1 Historical Review of the Three-Body Problem

The three-body problem has been a focus of mathematicians for centuries largely because, as stated concisely by Barrow-Green, "[t]his ancient problem – to describe the path of three bodies in mutual gravitational interaction – is one which is simple to pose but impossible to solve precisely" [14]. The general problem of three-bodies was first examined by Newton in the *Principia* in 1687 in which he also published his Law of Gravitation. Euler is credited with formulating the restricted three-body problem, however, and identified the three collinear equilibrium solutions in 1765. He first formulated the problem using a rotating reference frame in 1772. That same year, Lagrange determined the locations of the equilateral libration points.

The understanding of the restricted three-body problem was furthered significantly by Jacobi in 1836 when he demonstrated that a single integral of the motion exists for Euler's formulation of the problem (the Jacobian integral) [14]. In 1878, Hill demonstrated that the Jacobian integral, or Jacobi constant, can be used to determine the dynamical bounds on the motion of a spacecraft trajectory in the restricted three-body problem, i.e., zero velocity surfaces. Hill also approximated a family of periodic orbits about the Earth.

In 1899, Poincaré published his landmark, three-volume work, *Les Méthodes Nouvelles de la Mécanique Celeste*, which was heavily influenced by Hill's previous investigations. In *Méthodes Nouvelles*, Poincaré proves that an infinite number of periodic exist in the restricted three-body problem and proposed tools, such as the "surface of sections", that had not previously been suggested. In his ground-breaking work, he also proves that the general N-body problem cannot be solved in closed-form using the traditional approach involving analytical integration and integrals of the motion. Furthermore, Poincaré demonstrated that the Jacobi constant is the *only* integral of motion available in the restricted three-body problem [14].

The concepts introduced by Poincaré spurred further analytical and numerical investigations of periodic orbits in the restricted three-body problem by Darwin, Moul-

ton [15], and Strömgren [14] in the early part of the 20th century. With the advent of high-speed computing in the latter half of the 20th century, orbit computational capabilities increased dramatically. In 1967, Szebehely published the book, *Theory of Orbits* [16], which was perhaps the most complete compilation of information on the restricted three-body problem at its time of publication. As computing power and numerical methods continue to improve, the restricted three-body problem and its modern mission design applications make it a focal point of many researchers in the astrodynamics community.

1.2 Previous Contributions

Every mission design problem includes unique complexities and challenges. Two separate, but potentially related, aspects to missions in the Earth-Moon system include the stationkeeping of a spacecraft in the vicinity of an libration point as well as transfers between the Earth and Moon with application to manned space exploration.

1.2.1 Libration Point Orbit Stationkeeping

Libration point orbits are typically unstable and stationkeeping maneuvers must be implemented at regular intervals to maintain the orbit. In the 1970s, the use of collinear libration point orbits for lunar communications in the Earth-Moon system and the associated stationkeeping strategies and cost were explored by Farquhar [17] as well as Breakwell, Kamel, and Ratner [18]. Invariant manifold theory was later exploited to determine optimal stationkeeping maneuvers along halo orbits by Simó et al. [19], Howell and Keeter [20], and Gómez et al. [21]. In 2005, Janes and Beckman presented a candidate stationkeeping strategy for the James Webb Space Telescope (JWST) mission using a global search algorithm which does not rely on a baseline solution [22]. More recently, Grebow, Ozimek, Howell, and Folta analyzed "worst-case" stationkeeping costs associated with various libration point orbits in the Earth-Moon system [23]. In their study, control points from a baseline trajectory are targeted to

determine orbit maintenance costs in both the circular restricted three-body and full ephemeris models.

1.2.2 Earth-Moon Transfers

Earth-Moon transfers, with applications to manned space exploration, gained interest rapidly during the early years of the space race between the United States and the Soviet Union. Lunar free return trajectories were examined initially since such transfers guarantee passage to and from the vicinity of the Moon and were flown successfully during the Apollo 8, Apollo 10, and Apollo 11 missions. In 1963, techniques for computing free return trajectories in patched conic and circular restricted three-body models were explored by Penzo [24] and Schwaniger [25], respectively. Gibson combined the two approaches, also in 1963 [26]. More recently, an automated approach to lunar free return trajectory design was explored by Jesick and Ocampo [27]. For the next generation of manned missions to the lunar poles, robust onboard maneuver computation algorithms are desired. An initial guess strategy for such an autonomous process has been discussed by Ocampo and Saudemont [28] and numerical targeting strategies have also been explored by Marchand, Weeks, Smith, and Scarritt [29], Scarritt, Marchand, and Weeks [30], and Marchand et al. [31].

1.3 Current Work

The main objective of this analysis is the investigation of two phases of potential Earth-Moon missions. Both demonstrate the application of general differential corrections procedures in mission design problems. A control-point stationkeeping algorithm is applied to a variety of orbits in the vicinity of the L_2 libration point. Additionally, transfers from the Moon to the Earth are investigated with application to manned lunar mission design.

This analysis is organized as follows:

Chapter 2:

The background necessary to support Earth-Moon trajectory design is presented. The simplifying assumptions, geometry, and equations of motion in the circular restricted three-body problem are introduced. The equations of motion associated with an N-body ephemeris model are also presented. State transition matrices corresponding to orbits in both dynamical models are derived as a means of obtaining sensitivity information related to a numerically-determined reference trajectory. A generalized method of free variables and constraints is developed as a differential corrections procedure and is used throughout this analysis. Both single and multiple shooting algorithms are presented. Single-parameter and pseudo-arclength continuation are employed as a means of computing families of orbits and exploring the design space. Appropriate coordinate frame transformations are derived.

Chapter 3:

The differential corrections techniques introduced in Chapter 2 are used to compute orbits in the circular restricted three-body problem. Families of Lyapunov and halo orbits in the vicinity of the L_1 and L_2 collinear libration points are computed. Multiple shooting is employed to determine a quasi-periodic Lissajous orbit near the L_2 libration point. Families of free return trajectories are computed and incorporated as part of a bi-elliptic transfer strategy to develop a trajectory from low Earth orbit to a lunar polar orbit.

Chapter 4:

A general strategy for transitioning orbits from the circular restricted three-body problem to higher-fidelity ephemeris models is developed. Quasi-Lyapunov, quasi-halo, and Lissajous orbits are computed in the vicinity of L_2 in an Earth-Moon-Sun ephemeris model incorporating JPL DE405 ephemerides.

Chapter 5:

A control-point stationkeeping algorithm adapted from the work by Grebow et al. [23]

is used to maintain the L_2 Lissajous orbit designed for the ARTEMIS P_1 spacecraft for approximately 130 days. Several maneuver-placement strategies are explored and average ΔV costs associated with each approach are determined from Monte Carlo simulations. For purposes of comparison, stationkeeping costs are also computed for L_2 Lyapunov and halo orbits of comparable size to the ARTEMIS orbit.

Chapter 6:

A variable-time multiple shooting algorithm is developed and used to compute Moon-Earth transfers with applications to manned space exploration. The strategy allows for the insertion of an arbitrary number of ΔV maneuvers such that the total maneuver cost is constrained. Additionally, multiple Earth entry conditions are specified. The process is general and allows trajectories to be transitioned between the circular restricted three-body and ephemeris models which is particularly useful during the early stages of mission design. A known reference mission is numerically manipulated to significantly reduce ΔV costs and some solutions emerge that are not intuitive from two-body analysis.

Chapter 7:

The results of the analysis for both mission design problems are summarized. Recommendations for future work are presented.

2. BACKGROUND

Specific trajectory computation strategies and any accompanying results are dependent upon fundamental assumptions and the formulation of the problem. Thus, a critical first step is the establishment of the underlying framework for the problem and the development of the mathematical model. The Circular Restricted Three-Body Problem (CR3BP) is introduced along with the associated equations of motion; the N-body relative equations of motion that govern the behavior in a higher-fidelity ephemeris model are also derived. A basic numerical approach to incorporate free variables and constraints is developed as the foundation for differential corrections algorithms. Combining these algorithms with orbit continuation schemes form the basis for all trajectory design applications that appear. Useful coordinate frame transformations are also summarized.

2.1 The Circular Restricted Three-Body Problem

The region of space near the Earth and the Moon offers a unique dynamical environment in our solar system. The ratio between the mass of the Moon and the mass of the Earth is large relative to other known planet-moon systems. A consequence of this mass ratio is the fact that the motion of a spacecraft in the Earth-Moon region can often be influenced heavily by both bodies simultaneously. Thus, the circular restricted three-body problem serves as a particularly effective model and a powerful tool for mission design within the Earth-Moon system. Incorporating multiple gravity fields simultaneously, the CR3BP reflects the actual dynamical environment and also enables a transition to higher-fidelity models such that the final trajectories for actual flight retain desirable characteristics identified during the initial step in the

design process. The underlying assumptions in the model are initially introduced, the problem geometry is summarized, and the equations of motion are derived.

2.1.1 Assumptions

The problem formulation is based on a set of assumptions that are critical in gaining insight but retain the most significant dynamical features of the model. Initially, assume that all bodies are modeled as point masses. From Newton's Second Law, the motion of a particle P_i under the influence of N-1 gravitating bodies, P_j, is described by the following differential equation

$$m_i \boldsymbol{r_i''} = -\tilde{G} \sum_{\substack{j=1 \\ j \neq i}}^{n} \frac{m_i m_j}{r_{ji}^3} \boldsymbol{r_{ji}} \tag{2.1}$$

in which m_i represents the mass of the particle of interest and m_j identifies the other bodies that gravitationally influence its motion. The symbol $\tilde{G}$ is the gravitational constant expressed in dimensional units. The vectors $\boldsymbol{r_i}$ and $\boldsymbol{r_j}$ describe the position of these particles relative to an inertially fixed base point, and prime denotes differentiation with respect to dimensional time. Unless otherwise noted, boldface characters denote vector quantities. The same character in plain text represents the magnitude of the corresponding vector. The N-body model is simplified considerably by incorporating only three bodies ($N = 3$) and reduces equation (2.1) to the form

$$m_3 \boldsymbol{r_3''} = -\frac{\tilde{G} m_3 m_1}{r_{13}^3} \boldsymbol{r_{13}} - \frac{\tilde{G} m_3 m_2}{r_{23}^3} \boldsymbol{r_{23}} \tag{2.2}$$

where the particle of interest is arbitrarily selected to be P_3. A complete, closed-form solution to the three-body problem requires 18 integrals of the motion. Since there are only 10 known constants, an analytical solution is not currently known; the governing differential equations must be solved numerically. The geometry representing the general three-body problem appears in Figure 2.1. After reducing the N-body problem to three bodies, the problem is further simplified by assuming that the mass of the smallest body, m_3, is negligible in comparison to the masses of P_1

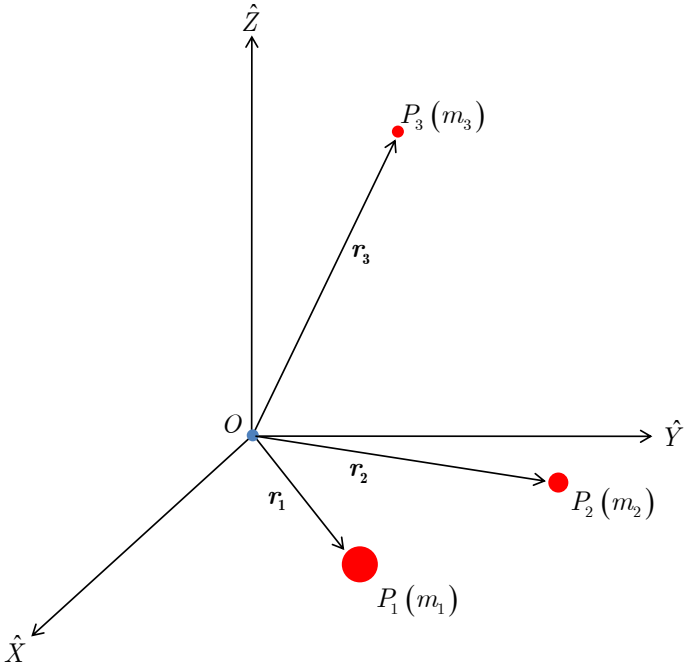

Figure 2.1. Geometry: General Three-Body Problem

and P_2, that is, m_1 and m_2 ($m_3 << m_1, m_2$). Consequently, the motion of P_3 does not influence the motion of either P_1 or P_2. As a result, the orbits of P_1 and P_2 are restricted and represented by conics in an isolated two-body system. For simplicity, it is also assumed that P_1 and P_2 move in circular orbits about their barycenter, B. The "primary system" consists of P_1 and P_2 which are labeled the "primaries". By convention, P_1 is the more massive particle.

2.1.2 Geometry of the Circular Restricted Three-Body Problem

Two coordinate frames are particularly significant in the formulation of the circular restricted three-body problem. An inertial reference frame, I, is centered at the barycenter, B, and is defined in terms of the unit vectors $\hat{X} - \hat{Y} - \hat{Z}$ where $\hat{Z}$ is aligned with the angular momentum vector of the orbiting primaries, P_1 and P_2. Since it is assumed that the primaries move in conic orbits, their motion is restricted

to the $\hat{X}-\hat{Y}$ plane. However, P_3 is not constrained to a plane and is free to move in any spatial direction. A rotating reference frame, R, also centered at B, is defined via unit vectors $\hat{x}-\hat{y}-\hat{z}$. The $\hat{z}$ axis, like $\hat{Z}$, is also aligned with the angular momentum vector of the orbiting primaries. The unit vector $\hat{x}$ is directed from the larger primary, P_1, toward the smaller body, P_2, and $\hat{y}$ completes the right-handed triad. The angle θ orients the rotating frame R relative to the inertial frame I. The geometry is illustrated in Figure 2.2. The positions of the primaries relative to the barycenter, B, are described by the vectors, $\boldsymbol{D_1}$ and $\boldsymbol{D_2}$. The relative position vectors, $\boldsymbol{D}$ and $\boldsymbol{R}$, define the position of the third body with respect to P_1 and P_2, respectively. Most importantly, the vector $\boldsymbol{p}$ denotes the location of P_3 with respect to the barycenter.

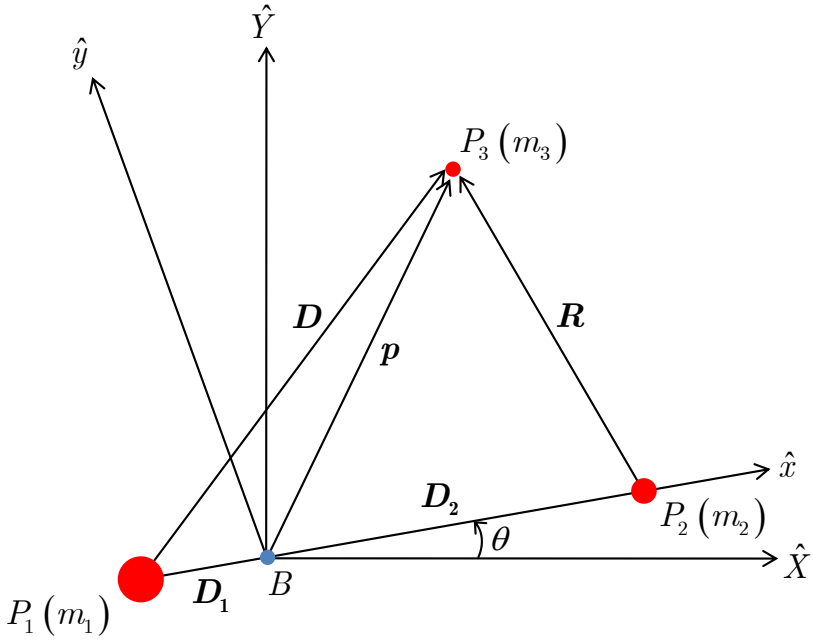

Figure 2.2. Geometry of the Circular Restricted Three-Body Problem

2.1.3 Equations of Motion

To compute trajectories in the CR3BP, it is first necessary to derive the appropriate equations of motion. Given the geometry of the CR3BP, apparent in Figure 2.2, equation (2.2) yields the following differential equation

$$m_3 \boldsymbol{p''} = -\frac{Gm_3m_1}{D^3}\boldsymbol{D} - \frac{Gm_3m_2}{R^3}\boldsymbol{R} \tag{2.3}$$

Despite the simplifying assumptions, a sufficient number of integrals of the motion are still not available to solve equation (2.3) analytically; numerical solutions are required to gain some understanding of the behavior. To better condition the differential equations of motion for either explicit or implicit numerical integration, it is useful to employ a straightforward nondimensionalization based on the characteristic quantities associated with length, mass, and time. The characteristic length, l^*, is defined to be the mean distance between the primaries, that is,

$$l^* = D_1 + D_2 \tag{2.4}$$

and the characteristic mass, m^*, is evaluated as the sum of the masses of the two primaries,

$$m^* = m_1 + m_2 \tag{2.5}$$

The characteristic time, τ^*, is deduced from Kepler's third law, i.e.,

$$\tau^* = \left(\frac{l^{*3}}{\tilde{G}m^*}\right)^{1/2} \tag{2.6}$$

and is defined such that the nondimensional gravitational constant, G, is unity. A conic definition of the dimensional mean motion, N, corresponding to the conic behavior of the primaries yields,

$$N = \left(\frac{\tilde{G}m^*}{l^{*3}}\right)^{1/2} \tag{2.7}$$

It follows that the nondimensional mean motion, n, is then written as,

$$n = N\tau^* = \left(\frac{\tilde{G}m^*}{l^{*3}}\right)^{1/2}\left(\frac{l^{*3}}{\tilde{G}m^*}\right)^{1/2} = 1 \tag{2.8}$$

Note that the nondimensional mean motion, n, is unity in the traditional formulation of the CR3BP. Consequently, the orbital period associated with the motion of the primaries about their common barycenter is 2π nondimensional time units.

Incorporating the characteristic quantities, the nondimensional position vectors, $\boldsymbol{r}$ and $\boldsymbol{d}$, mass parameter, μ, and nondimensional time parameter, t, are defined as follows

$$\boldsymbol{r} = \frac{\boldsymbol{R}}{l^*} \tag{2.9}$$

$$\boldsymbol{d} = \frac{\boldsymbol{D}}{l^*} \tag{2.10}$$

$$\mu = \frac{m_2}{m^*} \tag{2.11}$$

$$t = \frac{\tau}{\tau^*} \tag{2.12}$$

The nondimensional position vector, $\boldsymbol{\rho}$, representing the position of P_3 with respect to the barycenter and expressed in terms of rotating coordinates, is obtained by nondimensionalizing the position vector, $\boldsymbol{p}$, yielding the relationship,

$$\boldsymbol{\rho} = \frac{\boldsymbol{p}}{l^*} = x\hat{x} + y\hat{y} + z\hat{z} \tag{2.13}$$

The governing differential equation for the motion of P_3, that is, equation (2.3), is also nondimensionalized using the characteristic quantities. These nondimensional quantities are now substituted into equation (2.3) to obtain the nondimensional differential equation governing the motion of P_3, that is,

$$\ddot{\boldsymbol{\rho}} = -\frac{(1-\mu)\,\boldsymbol{d}}{d^3} - \frac{\mu \boldsymbol{r}}{r^3} \tag{2.14}$$

where dots indicate differentiation with respect to nondimensional time. From the geometry in Figure 2.2 and the definition of the center of mass, it is apparent that the nondimensional relative position vectors, $\boldsymbol{d}$ and $\boldsymbol{r}$, are determined respectively, as,

$$\boldsymbol{d} = (x+\mu)\,\hat{x} + y\hat{y} + z\hat{z} \tag{2.15}$$

$$\boldsymbol{r} = (x-1+\mu)\,\hat{x} + y\hat{y} + z\hat{z} \tag{2.16}$$

Much insight into the motion of P_3 is available through equation (2.14) from a kinetics perspective, but a kinematical relationship is also necessary to produce the scalar equations of motion. The derivative of $\boldsymbol{\rho}$ with respect to nondimensional time, as viewed by an inertial observer and expressed in terms of rotating coordinates is determined via the appropriate transformation relationship,

$$\frac{{}^{I}d\boldsymbol{\rho}}{dt} = \frac{{}^{R}d\boldsymbol{\rho}}{dt} + {}^{I}\boldsymbol{\omega}^{R} \times \boldsymbol{\rho} \tag{2.17}$$

$$\frac{{}^{I}d^2\boldsymbol{\rho}}{dt^2} = \frac{{}^{R}d^2\boldsymbol{\rho}}{dt^2} + 2{}^{I}\boldsymbol{\omega}^{R} \times \frac{{}^{R}d\boldsymbol{\rho}}{dt} + {}^{I}\boldsymbol{\omega}^{R} \times {}^{I}\boldsymbol{\omega}^{R} \times \boldsymbol{\rho} \tag{2.18}$$

where ${}^{I}\boldsymbol{\omega}^{R} = n\hat{z}$ represents the angular velocity of the rotating frame with respect to the inertial frame. Of course, $\frac{{}^{R}d\boldsymbol{\rho}}{dt}$ represents the change in the position vector as observed from the rotating frame, R. Thus, the kinematic expansion for inertial acceleration is written in the form,

$$\ddot{\boldsymbol{\rho}} = \left(\ddot{x} - 2n\dot{y} - n^2x\right)\hat{x} + \left(\ddot{y} + 2n\dot{x} - n^2y\right)\hat{y} + \ddot{z}\hat{z} \tag{2.19}$$

Note that the nondimensional mean motion, n, is equal to one in nondimensional units but is included for completeness. Substituting the kinematic expression from equations (2.14), (2.15), and (2.16) into equation (2.19) yields the three scalar, second-order differential equations of motion for P_3 in the CR3BP,

$$\ddot{x} - 2n\dot{y} - n^2x = -\frac{(1-\mu)(x+\mu)}{d^3} - \frac{\mu(x-1+\mu)}{r^3} \tag{2.20}$$

$$\ddot{y} + 2n\dot{x} - n^2y = -\frac{(1-\mu)y}{d^3} - \frac{\mu y}{r^3} \tag{2.21}$$

$$\ddot{z} = -\frac{(1-\mu)z}{d^3} - \frac{\mu z}{r^3} \tag{2.22}$$

where the scalar relative distances are,

$$d = \sqrt{(x+\mu)^2 + y^2 + z^2} \tag{2.23}$$

$$r = \sqrt{(x-1+\mu)^2 + y^2 + z^2} \tag{2.24}$$

and all derivatives are relative to a rotating observer. These equations of motion are written more compactly following the introduction of a pseudo-potential function,

$$U^* = \frac{1-\mu}{d} + \frac{\mu}{r} + \frac{1}{2}n^2\left(x^2 + y^2\right) \tag{2.25}$$

Equations (2.20)–(2.22) appear in a more succinct form as,

$$\ddot{x} - 2\dot{y} = \frac{\partial U^*}{\partial x} \tag{2.26}$$

$$\ddot{y} + 2\dot{x} = \frac{\partial U^*}{\partial y} \tag{2.27}$$

$$\ddot{z} = \frac{\partial U^*}{\partial z} \tag{2.28}$$

Equilibrium solutions in the CR3BP are determined in the next section. The form of equations (2.26)–(2.28) is very useful to identify particular solutions.

2.1.4 The Libration Points

Since the equations of motion are formulated within the context of a rotating reference frame, the equations of motion in the CR3BP are autonomous and the solutions are time-invariant. The equilibrium solutions to the equations of motion, consequently, are invariant as well and appear as constants relative to the rotating frame. At these equilibrium points, the velocity and acceleration relative to the rotating frame must be zero or, equivalently,

$$\nabla U^* = 0 \tag{2.29}$$

This gradient yields the following scalar requirements, i.e.,

$$\frac{\partial U^*}{\partial x} = -\frac{(1-\mu)(x_{eq}+\mu)}{d_{eq}^3} - \frac{\mu(x_{eq}-1+\mu)}{r_{eq}^3} + n^2 x_{eq} = 0 \tag{2.30}$$

$$\frac{\partial U^*}{\partial y} = -\frac{(1-\mu)\, y_{eq}}{d_{eq}^3} - \frac{\mu y_{eq}}{r_{eq}^3} + n^2 y_{eq} = 0 \tag{2.31}$$

$$\frac{\partial U^*}{\partial z} = -\frac{(1-\mu)\, z_{eq}}{d_{eq}^3} - \frac{\mu z_{eq}}{r_{eq}^3} = 0 \tag{2.32}$$

where x_{eq}, y_{eq}, and z_{eq} correspond to the Cartesian coordinates of the position vectors that locate the equilibrium solutions. From equation (2.32), it is clear that if $\frac{\partial U^*}{\partial z} = 0$, then $z_{eq} = 0$. Thus, all equilibrium solutions in the CR3BP lie in the $\hat{x} - \hat{y}$ plane. By inspection, it is also evident that some equilibrium solutions likely exist for $y_{eq} = 0$. Substituting $y_{eq} = z_{eq} = 0$ into equation (2.30) produces the equation,

$$-\frac{(1-\mu)(x_{eq}+\mu)}{|x_{eq}+\mu|^3} - \frac{\mu(x_{eq}+1-\mu)}{|x_{eq}-1+\mu|^3} + x_{eq} = 0 \tag{2.33}$$

which is quintic in x_{eq}, but possesses only three real solutions. This nonlinear equation is not solvable in closed-form, but solutions are available iteratively using a simple Newton's Method. While equation (2.33) can be used directly in such an iterative procedure, in practice, the problem is often better behaved numerically if the equation is rewritten in terms of the distance of each point relative to the closest primary, γ_i. This formulation results in a modified form of equation (2.33), i.e.,

$$-\frac{(1-\mu)(x_{eq} \pm \gamma_i + \mu)}{|x_{eq} \pm \gamma_i + \mu|^3} - \frac{\mu(x_{eq} \pm \gamma_i + 1 - \mu)}{|x_{eq} \pm \gamma_i - 1 + \mu|^3} + x_{eq} \pm \gamma_i = 0 \tag{2.34}$$

The equilibrium solutions are denoted the libration points and the equilibrium points located along the x-axis are specified as the collinear libration points. In fact, the collinear points were noted by Euler in 1765 [16]. Today, by convention, L_3 is positioned to the left of P_1, the equilibrium point on the far side of P_2 is denoted L_2, and L_1 lies between the two primaries.

Two additional equilibrium points also exist and their locations are determined by using algebraic manipulation to demonstrate that equations (2.30) and (2.31) are satisfied if $d = 1$ and $r = 1$. Since the nondimensional distance between the primaries is also 1, it is apparent that the two remaining equilibrium points form equilateral triangles with the two primaries. These solutions, first identified by Lagrange in 1772 [16], possess Cartesian coordinates $x_{eq} = \frac{1}{2} - \mu$, $y_{eq} = \pm\frac{\sqrt{3}}{2}$, $z_{eq} = 0$ and are termed the equilateral libration points. By convention, L_4 leads the smaller primary in its orbit by 60° and L_5 trails P_2 in its orbit by 60°. The locations of all five libration points appear in Figure 2.3. The positions of the equilibrium solutions and primaries are plotted to scale in the figure, relative to the Earth-Moon system, but the Earth and Moon as the primaries appear larger than their true relative size by a factor of 10.

2.2 The Ephemeris Model

While the assumptions associated with the circular restricted three-body problem produce a model that serves as a powerful tool for the study of the general dynam-

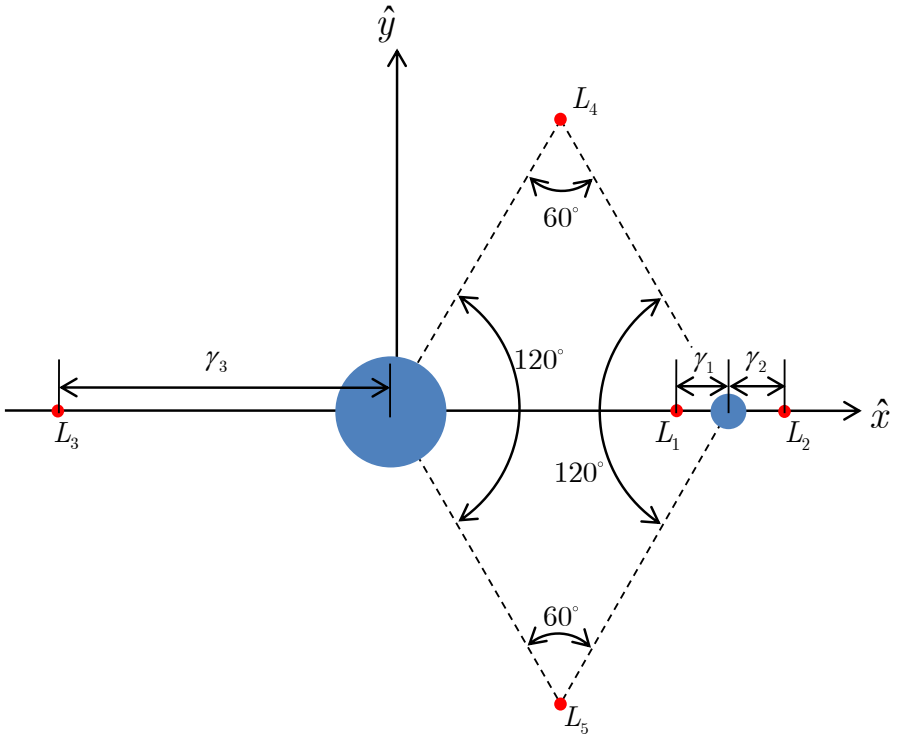

Figure 2.3. Locations of the Libration Points in the CR3BP, Scaled Consistent with the Earth and Moon as the Primaries

ical behavior of a system, the trajectories that are used to support actual missions must also be examined in higher-fidelity models that better simulate the true dynamical environment. Several applications included in this analysis require accuracies for which a mathematical model consistent with only the CR3BP is not sufficient. A higher-fidelity model is created using the Jet Propulsion Laboratory (JPL) DE405 planetary ephemerides to locate the positions of any celestial bodies included in the model during the course of the simulation. In the Earth-Moon system, for example, the incorporation of lunar eccentricities and perturbations due to solar gravity significantly improve the fidelity of a trajectory initially generated in a lower-fidelity model.

2.2.1 Relative Equations of Motion: N-Body Model

A set of differential equations that incorporates some of the more complex forces on a spacecraft is required to model the motion to a higher degree of accuracy. The goal is a representation of the behavior of the vehicle, P_i, in an N-body ephemeris model. Recall that the set of N-body differential equations, vector equation (2.1), is originally formulated such that the particle is located with respect to an arbitrary inertially fixed base point. In practice, it is much more useful to compute the motion of a spacecraft in inertial space relative to a central body. This relative formulation is illustrated in Figure 2.4, where the central body is denoted by q and the subscript i represents the body of interest (typically a spacecraft). All other gravitational bodies in the model are labeled j. To compute the motion of P_i relative to the central body, vector equation (2.1) is reformulated as a set of dimensional N-body relative equations of motion,

$$\boldsymbol{r}''_{\boldsymbol{qi}} + \frac{\tilde{G}\left(m_i + m_q\right)}{r_{qi}^3}\boldsymbol{r}_{\boldsymbol{qi}} = \tilde{G}\sum_{\substack{j=1 \\ j\neq i,q}}^{n} m_j \left(\frac{\boldsymbol{r}_{\boldsymbol{ij}}}{r_{ij}^3} - \frac{\boldsymbol{r}_{\boldsymbol{qj}}}{r_{qj}^3}\right) \tag{2.35}$$

where the vector $\boldsymbol{r}_{\boldsymbol{qj}}$ represents the position of each perturbing body with respect to the central body. These relative locations of the celestial bodies are delivered directly

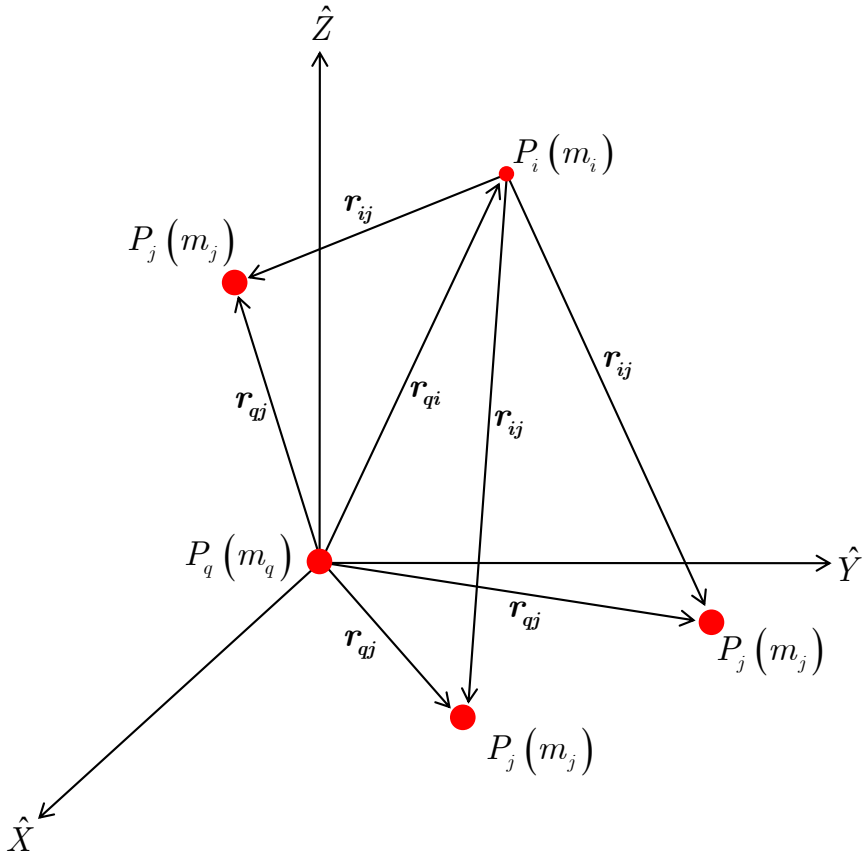

Figure 2.4. Geometry of the Relative N-Body Problem

from DE405 ephemeris data. The vector $\boldsymbol{r_{ij}}$ then corresponds to the position of each perturbing body relative to the body of interest, P_i, and are generated using the relationship,

$$\boldsymbol{r_{ij}} = \boldsymbol{r_{qj}} - \boldsymbol{r_{qi}} \tag{2.36}$$

which relates $\boldsymbol{r_{ij}}$ to the vectors that define the position of P_i relative to the central body, $\boldsymbol{r_{qi}}$, and the positions of the perturbing bodies relative to the central body, $\boldsymbol{r_{qj}}$; both types of vectors, that is, $\boldsymbol{r_{qi}}$ and $\boldsymbol{r_{qj}}$, are known. The information available from equations (2.35) and (2.36), in combination with the DE405 ephemerides, is sufficient to model the motion of P_i under the influence of N gravitational point masses. Note

that the fidelity of equation (2.35) is further improved if additional force models, such as solar radiation pressure and gravity harmonics, are incorporated.

2.3 Dynamical Sensitivities and Differential Corrections

As mentioned previously, closed-form analytical solutions are not available when the dynamical influences of more than two bodies are considered simultaneously. Numerical methods are necessary, not only to propagate the differential equations of motion, but also to manipulate, or correct, a trajectory arc to meet some desired set of objectives and potentially generate a particular solution to the differential equations of motion. Accomplishment of such goals is facilitated by exploring the dynamical sensitivities and numerical strategies to exploit the information for the computation of solutions. Consequently, numerical differential corrections schemes are an essential tool for designing trajectories in multi-body regimes.

2.3.1 Obtaining a Baseline Solution

To produce a trajectory with some set of desired characteristics, the initial propagation of a baseline arc is essential. For this analysis, all arcs are generated by numerically integrating the equations of motion, regardless of the dynamical system. For the computation of trajectories in either the CR3BP or ephemeris models, the second-order equations of motion are rewritten as a series of first-order differential equations in the form,

$$\dot{\boldsymbol{x}} = \boldsymbol{f}\left(t, \boldsymbol{x}, \boldsymbol{\lambda}\right) \tag{2.37}$$

where $\boldsymbol{x}$ is a six-dimensional state vector, $\boldsymbol{x} = \begin{bmatrix} r_x & r_y & r_z & v_x & v_y & v_z \end{bmatrix}^T$, which contains both position (r_x, r_y, r_z) and velocity (v_x, v_y, v_z) information. For application in the CR3BP, these specific states are $\boldsymbol{x} = \begin{bmatrix} x & y & z & \dot{x} & \dot{y} & \dot{z} \end{bmatrix}^T$. The state vector is similarly defined for the ephemeris model, i.e., $\boldsymbol{x} = \begin{bmatrix} X & Y & Z & \dot{X} & \dot{Y} & \dot{Z} \end{bmatrix}^T$. The vector $\boldsymbol{\lambda}$ contains additional parameters upon which the dynamical models depend

(e.g., μ in the CR3BP and epoch time in the ephemeris model). For the explicit numerical integration of the first-order equations of motion appropriate to any model, an initial condition and time interval must be specified. For example, consider an initial state $\boldsymbol{x_0} = \boldsymbol{x}(t_0)$ integrated from time t_0 to $t = t_0 + T$ to yield a final, numerically integrated state $\boldsymbol{x}(\boldsymbol{x_0}, t)$. This simple scenario is illustrated in Figure 2.5. Throughout this analysis, the differential equations of motion in both the CR3BP and the ephemeris model are propagated using variable-time Adams-Bashforth-Moulton integrators.

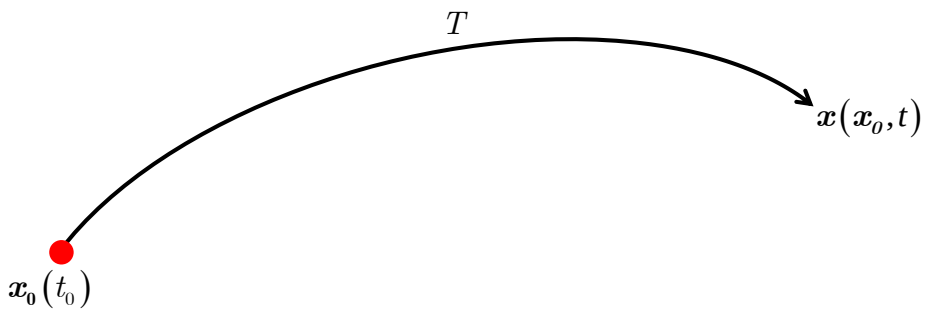

Figure 2.5. Example Baseline Arc

2.3.2 State Transition Matrix

For various types of numerical analysis, including the use of gradient-based differential corrections methods, a critical requirement is the availability of derivative information reflecting the sensitivity of a final integrated state, $\boldsymbol{x}(\boldsymbol{x_0}, t)$, to the initial state, $\boldsymbol{x_0}$, i.e., $\frac{\partial \boldsymbol{x}}{\partial \boldsymbol{x_0}}$. Since the final state is determined numerically and not analytically, these derivatives are not determined directly. Instead, a set of partials are associated with the first-order variational equations,

$$\delta \dot{\boldsymbol{x}} = A(t)\, \delta \boldsymbol{x} \tag{2.38}$$

where $A(t) = \frac{\partial \boldsymbol{f}}{\partial \boldsymbol{x}}$. To produce equation (2.38), the nonlinear equations of motion are expanded about a baseline solution and only the linear terms are retained [32]. The matrix $A(t)$ is the Jacobian matrix and relates changes in the vector field, $\boldsymbol{f}(t, \boldsymbol{x}, \boldsymbol{\lambda})$, to changes in the states, $\boldsymbol{x}(\boldsymbol{x_0}, t)$, that is, $\frac{\partial \boldsymbol{f}}{\partial \boldsymbol{x}}$. As a solution to the first-order variational equations in equation (2.38), the matrix derivative $\frac{\partial \boldsymbol{x}}{\partial \boldsymbol{x_0}}$ transforms variations in the initial state to variations in the state at time t, i.e.,

$$\delta \boldsymbol{x}(\boldsymbol{t}) = \left(\frac{\partial \boldsymbol{x}}{\partial \boldsymbol{x_0}}\right) \delta \boldsymbol{x}(\boldsymbol{t_0}) \tag{2.39}$$

As such, the matrix $\frac{\partial \boldsymbol{x}}{\partial \boldsymbol{x_0}}$ essentially predicts, in a linear sense, the downstream impact of variations at time t_0. To determine $\frac{\partial \boldsymbol{x}}{\partial \boldsymbol{x_0}}$, a first-order differential equation governing its behavior is written,

$$\frac{d}{dt}\left(\frac{\partial \boldsymbol{x}}{\partial \boldsymbol{x_0}}\right) = \frac{d}{d\boldsymbol{x_0}}\left(\frac{d\boldsymbol{x}}{dt}\right) \tag{2.40}$$

since $\boldsymbol{x_0}$ and t are independent. Rewriting the time derivative of $\boldsymbol{x}(\boldsymbol{x_0}, t)$ and substituting equation (2.37) yields equations,

$$\frac{d}{dt}\left(\frac{\partial \boldsymbol{x}}{\partial \boldsymbol{x_0}}\right) = \frac{d}{d\boldsymbol{x_0}}\dot{\boldsymbol{x}} \tag{2.41}$$

$$= \frac{d}{d\boldsymbol{x_0}}\boldsymbol{f}(t, \boldsymbol{x}, \boldsymbol{\lambda}) \tag{2.42}$$

$$= \frac{\partial \boldsymbol{f}}{\partial \boldsymbol{x}}\frac{d\boldsymbol{x}}{d\boldsymbol{x_0}} \tag{2.43}$$

Substituting the definition of the matrix, $A(t)$, from the variational equations in equation (2.38), equation (2.43) is rewritten,

$$\frac{d}{dt}\left(\frac{\partial \boldsymbol{x}}{\partial \boldsymbol{x_0}}\right) = A(t)\frac{\partial \boldsymbol{x}}{\partial \boldsymbol{x_0}} \tag{2.44}$$

The matrix derivative $\frac{\partial \boldsymbol{x}}{\partial \boldsymbol{x_0}}$ has wide-ranging applications and is labeled the State Transition Matrix (STM), $\Phi(t, t_0)$. Assuming application to the CR3BP and a state vector of length six, the scalar elements of the STM appear in the 6×6 matrix,

$$\Phi(t, t_0) = \begin{bmatrix} \frac{\partial x}{\partial x_0} & \frac{\partial x}{\partial y_0} & \frac{\partial x}{\partial z_0} & \frac{\partial x}{\partial \dot{x}_0} & \frac{\partial x}{\partial \dot{y}_0} & \frac{\partial x}{\partial \dot{z}_0} \\ \frac{\partial y}{\partial x_0} & \frac{\partial y}{\partial y_0} & \frac{\partial y}{\partial z_0} & \frac{\partial y}{\partial \dot{x}_0} & \frac{\partial y}{\partial \dot{y}_0} & \frac{\partial y}{\partial \dot{z}_0} \\ \frac{\partial z}{\partial x_0} & \frac{\partial z}{\partial y_0} & \frac{\partial z}{\partial z_0} & \frac{\partial z}{\partial \dot{x}_0} & \frac{\partial z}{\partial \dot{y}_0} & \frac{\partial z}{\partial \dot{z}_0} \\ \frac{\partial \dot{x}}{\partial x_0} & \frac{\partial \dot{x}}{\partial y_0} & \frac{\partial \dot{x}}{\partial z_0} & \frac{\partial \dot{x}}{\partial \dot{x}_0} & \frac{\partial \dot{x}}{\partial \dot{y}_0} & \frac{\partial \dot{x}}{\partial \dot{z}_0} \\ \frac{\partial \dot{y}}{\partial x_0} & \frac{\partial \dot{y}}{\partial y_0} & \frac{\partial \dot{y}}{\partial z_0} & \frac{\partial \dot{y}}{\partial \dot{x}_0} & \frac{\partial \dot{y}}{\partial \dot{y}_0} & \frac{\partial \dot{y}}{\partial \dot{z}_0} \\ \frac{\partial \dot{z}}{\partial x_0} & \frac{\partial \dot{z}}{\partial y_0} & \frac{\partial \dot{z}}{\partial z_0} & \frac{\partial \dot{z}}{\partial \dot{x}_0} & \frac{\partial \dot{z}}{\partial \dot{y}_0} & \frac{\partial \dot{z}}{\partial \dot{z}_0} \end{bmatrix} \tag{2.45}$$

The first-order differential equation governing its behavior in equation (2.44) is rewritten,

$$\dot{\Phi}(t, t_0) = A(t)\,\Phi(t, t_0) \tag{2.46}$$

where the elements of $\Phi(t, t_0)$ represent the 36 partials that are integrated simultaneously with the equations of motion to produce the STM at any time along the integrated trajectory. The STM is subject to the initial conditions,

$$\Phi(t_0, t_0) = I_{6\times 6} \tag{2.47}$$

where $I_{6\times 6}$ is a 6×6 identity matrix.

2.3.2.1 State Transition Matrix: Restricted Three-Body Problem

The STM, $\Phi(t, t_0)$, is a general relationship and equations (2.45), (2.46), and (2.47) are valid for a wide range of applications. The evaluation of the partials in the matrix, $A(t)$, however, depends entirely on the dynamical model. Recall that $A(t)$ is defined as

$$A(t) = \frac{\partial \boldsymbol{f}}{\partial \boldsymbol{x}} \tag{2.48}$$

Let the three scalar, second-order differential equations (2.20)–(2.22) that govern motion of P_3 in the CR3BP, serve as the basis for this application. If the second-

order equations are written in first-order form consistent with equation (2.37), then, using equation (2.48), $A(t)$ possesses the following form in the CR3BP,

$$A(t) = \begin{bmatrix} 0 & 0 & 0 & 1 & 0 & 0 \\ 0 & 0 & 0 & 0 & 1 & 0 \\ 0 & 0 & 0 & 0 & 0 & 1 \\ U^*_{xx} & U^*_{xy} & U^*_{xz} & 0 & 2 & 0 \\ U^*_{yx} & U^*_{yy} & U^*_{yz} & -2 & 0 & 0 \\ U^*_{zx} & U^*_{zy} & U^*_{zz} & 0 & 0 & 0 \end{bmatrix} \tag{2.49}$$

where, U^* denotes the pseudo-potential function and

$$U^*_{ij} = \frac{\partial^2 U^*}{\partial i \partial j} \tag{2.50}$$

Note that $A(t)$ can also be expressed more concisely using four 3×3 sub-matrices as,

$$A(t) = \begin{bmatrix} 0_{3\times3} & I_{3\times3} \\ U_{XX} & \Omega \end{bmatrix} \tag{2.51}$$

The STM, $\Phi(t, t_0)$, is readily computed in the CR3BP using equation (2.46) in conjunction with equations (2.47) and (2.49).

2.3.2.2 State Transition Matrix: Ephemeris Model

An identical procedure is used to generate the form of the matrix, $A(t)$, for application in the ephemeris model except that a different set of governing equations is employed. The N-body relative equations of motion in equation (2.35) are first expressed as a series of first-order differential equations. Then, deriving the expressions

for the partial derivatives with respect to the state, $\boldsymbol{x}$, yields the expression for $A(t)$ in the ephemeris model,

$$A(t) = \begin{bmatrix} 0 & 0 & 0 & 1 & 0 & 0 \\ 0 & 0 & 0 & 0 & 1 & 0 \\ 0 & 0 & 0 & 0 & 0 & 1 \\ \frac{\partial \ddot{X}}{\partial X} & \frac{\partial \ddot{X}}{\partial Y} & \frac{\partial \ddot{X}}{\partial Z} & 0 & 0 & 0 \\ \frac{\partial \ddot{Y}}{\partial X} & \frac{\partial \ddot{Y}}{\partial Y} & \frac{\partial \ddot{Y}}{\partial Z} & 0 & 0 & 0 \\ \frac{\partial \ddot{Z}}{\partial X} & \frac{\partial \ddot{Z}}{\partial Y} & \frac{\partial \ddot{Z}}{\partial Z} & 0 & 0 & 0 \end{bmatrix} \tag{2.52}$$

Note that two of the 3×3 sub-matrices in $A(t)$ are comprised entirely of zeros. These zero sub-matrices exist when $A(t)$ is evaluated in the ephemeris model because the N-body relative equations of motion are formulated in an inertial reference frame. Thus, no gyroscopic terms appear in the equations of motion. The STM, $\Phi(t, t_0)$, is obtainable in the N-body ephemeris model, as well, using equation (2.46) in conjunction with equations (2.47) and (2.52).

2.3.3 A Generalized Method of Free Variables and Constraints

Ultimately, a differential corrections algorithm for use in a multi-body dynamics problem is employed to solve a two-point boundary value problem (TPBVP). There are numerous ways to approach the computation of a numerical solution to a TPBVP, but a straightforward constraint-variable method based on a Newton approach is used exclusively throughout this analysis due to its simplicity and adaptability [21, 33]. The formulation is sufficiently general and readily applicable to a wide variety of problems in both the CR3BP and ephemeris models. The general method and its specific application to various shooting techniques are introduced.

Consider first a free variable vector, $\boldsymbol{X}$, comprised of n design variables,

$$\boldsymbol{X} = \begin{bmatrix} X_1 \\ \vdots \\ X_n \end{bmatrix} \tag{2.53}$$

Within the context of trajectory design, $\boldsymbol{X}$ typically consists of a number of state vectors, $\boldsymbol{x_i}$, and integration times, T_i. Other quantities, e.g., slack variables, are frequently included as well. To ensure that the trajectory possesses some desired characteristics, the free variable vector is subject to m scalar constraint equations satisfying $\boldsymbol{F}(\boldsymbol{X}) = \boldsymbol{0}$, that is,

$$\boldsymbol{F}(\boldsymbol{X}) = \begin{bmatrix} F_1(\boldsymbol{X}) \\ \vdots \\ F_m(\boldsymbol{X}) \end{bmatrix} = \boldsymbol{0} \tag{2.54}$$

In multi-body design problems, commonly constrained quantities include position, velocity, distances, and a variety of angles and rates. For this approach, the goal is the numerical computation of a solution $\boldsymbol{X^*}$ that satisfies the constraint equations, i.e., $\boldsymbol{F}(\boldsymbol{X^*}) = \boldsymbol{0}$, within some acceptable numerical accuracy. Given an initial free variable vector, $\boldsymbol{X^0}$, then $\boldsymbol{F}(\boldsymbol{X})$ can be expanded about $\boldsymbol{X^0}$ in a Taylor series and approximated to first-order, that is,

$$\boldsymbol{F}(\boldsymbol{X}) \approx \boldsymbol{F}\left(\boldsymbol{X^0}\right) + D\boldsymbol{F}\left(\boldsymbol{X^0}\right)\left(\boldsymbol{X} - \boldsymbol{X^0}\right) \tag{2.55}$$

where $D\boldsymbol{F}(\boldsymbol{X^0})$ is the m x n Jacobian matrix,

$$D\boldsymbol{F}\left(\boldsymbol{X^0}\right) = \frac{\partial \boldsymbol{F}(\boldsymbol{X^0})}{\partial \boldsymbol{X^0}} = \begin{bmatrix} \frac{\partial F_1}{\partial X_1} & \cdots & \frac{\partial F_1}{\partial X_n} \\ \vdots & \ddots & \vdots \\ \frac{\partial F_m}{\partial X_1} & \cdots & \frac{\partial F_m}{\partial X_n} \end{bmatrix} \tag{2.56}$$

As indicated, $D\boldsymbol{F}(\boldsymbol{X^0})$ includes the partial derivatives of the constraints with respect to the free variables and is evaluated at $\boldsymbol{X^0}$. From equation (2.54), $\boldsymbol{F}(\boldsymbol{X}) = \boldsymbol{0}$ which allows equation (2.55) to be reduced and generalized as

$$\boldsymbol{F}\left(\boldsymbol{X^j}\right) + D\boldsymbol{F}\left(\boldsymbol{X^j}\right)\left(\boldsymbol{X^{j+1}} - \boldsymbol{X^j}\right) = \boldsymbol{0} \tag{2.57}$$

where $\boldsymbol{X^j}$ and $\boldsymbol{X^{j+1}}$ represent the current and next iterations of the free variable vector, respectively. Note that, given a reasonable initial guess, the error, $\|\boldsymbol{F}(\boldsymbol{X})\|$, should generally be reduced in each iteration, i.e.,

$$\left\|\boldsymbol{F}\left(\boldsymbol{X^{j+1}}\right)\right\| < \left\|\boldsymbol{F}\left(\boldsymbol{X^j}\right)\right\| \tag{2.58}$$

Equation (2.57) is employed to iteratively solve for an $\boldsymbol{X^{j+1}}$ such that

$$\boldsymbol{F}\left(\boldsymbol{X^{j+1}}\right) = \boldsymbol{F}\left(\boldsymbol{X^{*}}\right) = \boldsymbol{0} \tag{2.59}$$

However, because this is a numerical procedure, in practice the problem is iterated until $\left\|\boldsymbol{F}\left(\boldsymbol{X^{j+1}}\right)\right\|$ is reduced below a specified convergence tolerance, ε, i.e.,

$$\left\|\boldsymbol{F}\left(\boldsymbol{X^{j+1}}\right)\right\| < \varepsilon \tag{2.60}$$

The actual implementation of this scheme to iteratively solve equation (2.57), however, depends on the manner in which the problem is formulated. If there exists an equal number of free variables and constraints, then $n = m$ and $D\boldsymbol{F}\left(\boldsymbol{X^{j}}\right)$ is square and invertible. Consequently, equation (2.57) possesses a single solution produced by a simple multi-variable Newton's Method,

$$\boldsymbol{X^{j+1}} = \boldsymbol{X^{j}} - D\boldsymbol{F}\left(\boldsymbol{X^{j}}\right)^{-1}\boldsymbol{F}\left(\boldsymbol{X^{j}}\right) \tag{2.61}$$

If the number of free variables exceeds the number of constraints, then $n > m$ and, generally, infinitely many solutions satisfy equation (2.57). The selection of a single solution from among many options requires the specification of some selection criteria. One very useful choice is a minimum norm solution, that is,

$$\boldsymbol{X^{j+1}} = \boldsymbol{X^{j}} - D\boldsymbol{F}\left(\boldsymbol{X^{j}}\right)^{T}\left[D\boldsymbol{F}\left(\boldsymbol{X^{j}}\right)D\boldsymbol{F}\left(\boldsymbol{X^{j}}\right)^{T}\right]^{-1}\boldsymbol{F}\left(\boldsymbol{X^{j}}\right) \tag{2.62}$$

The minimum norm solution is selected throughout this analysis because it minimizes the difference between $\boldsymbol{X^{j+1}}$ and the previous iteration, $\boldsymbol{X^{j}}$. Essentially, a minimum norm algorithm uses an orthogonal projection to compute the solution. Minimizing the difference between one update and the next is desirable because a converged solution, $\boldsymbol{X^{*}}$, is then close to the initial guess, $\boldsymbol{X^{0}}$. Typically, the converged solution retains most of the characteristics of the initial guess, as well.

This constraint-variable approach is employed to solve all numerical corrections problems in this analysis. The basic methodology is summarized in four straightforward steps:

1. Define all the problem variables and construct the free variable vector, $\boldsymbol{X}$
2. Define all the problem constraints and develop the constraint vector, $\boldsymbol{F}(\boldsymbol{X}) = \boldsymbol{0}$
3. Calculate the partial derivatives of the constraints with respect to the free variables and derive the Jacobian matrix, $D\boldsymbol{F}(\boldsymbol{X}) = \frac{\partial \boldsymbol{F}(\boldsymbol{X})}{\partial \boldsymbol{X}}$
4. Based on the size of the problem, iteratively solve for $\boldsymbol{X}^*$ using either equation (2.61) or (2.62) or a suitable alternative

This method represents a powerful design tool that can be formulated in many ways to solve a wide range of trajectory design problems.

2.4 Applications of the Generalized Method to Differential Corrections

The generalized constraint and free variable method serves as the basis for the single and multiple shooting differential corrections algorithms in this analysis [34]. Both fixed- and variable-time algorithms are discussed. These algorithms are integrated into single-parameter and pseudo-arclength continuation schemes to generate families of orbits and introduce maneuvers as required. All sample trajectories in this chapter are generated in the CR3BP, but the algorithms are adaptable to the ephemeris model with minimal adjustment.

2.4.1 Fixed-Time Single Shooting

The most basic differential corrections procedure is a fixed-time, single shooting algorithm. It is termed "single shooting" because only a single numerically integrated trajectory arc or segment is involved in the TPBVP. An infinite number of single shooting problems can be formulated, but a common, straightforward example is addressed here. First, consider a trajectory arc that is defined by an initial state vector, $\boldsymbol{x_0}$, at time t_0. Propagating this trajectory forward in time for a predetermined time interval, T, yields a final state, $\boldsymbol{x}(\boldsymbol{x_0}, t)$, at time $t = t_0 + T$. For simplicity, $\boldsymbol{x}(\boldsymbol{x_0}, t)$ is

abbreviated $\boldsymbol{x^t}$ which denotes the flow. This trajectory arc is considered the baseline solution for the differential corrections algorithm. Next, assume that the desired trajectory arc terminates at a prespecified target position, $\boldsymbol{r_d} = \begin{bmatrix} x_d & y_d & z_d \end{bmatrix}^T$, rather than the final state that is reached along the baseline solution. The time of flight (TOF) for both trajectories is fixed at T and the initial position state corresponding to this trajectory arc is fixed. This scenario is illustrated in Figure 2.6. Essentially, in

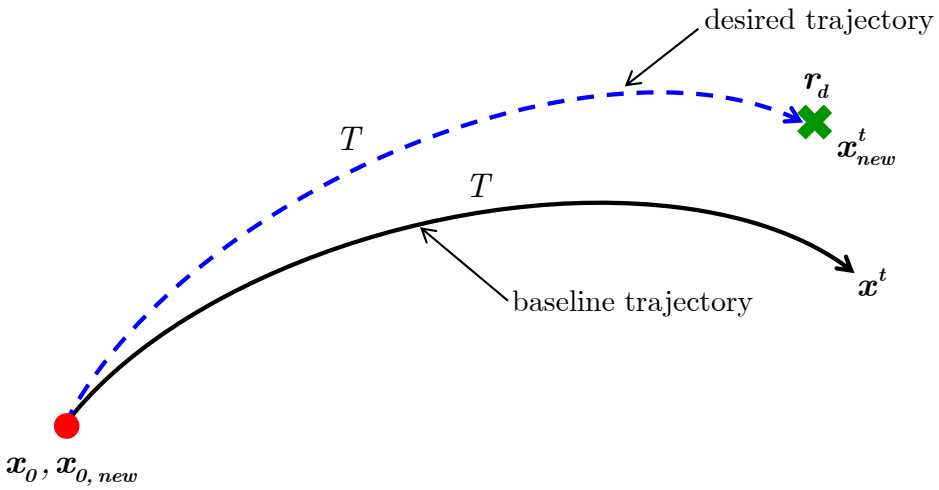

Figure 2.6. Fixed-Time, Single Shooting Algorithm

this problem formulation, the goal is the determination of the velocity vector at the initial location that delivers the trajectory to the desired target position in a specified length of time. In practical applications, this approach is equivalent to computing the impulsive ΔV maneuver to be implemented at the initial state to reach the target location. Given the general methodology described in Section 2.3.3, the first step to construct the fixed-time single shooting algorithm is the identification of the elements

of the free variable vector, $\boldsymbol{X}$. In this example, only the initial velocities are design variables, so $\boldsymbol{X}$ is represented by the three-element vector,

$$\boldsymbol{X} = \begin{bmatrix} \dot{x}_0 \\ \dot{y}_0 \\ \dot{z}_0 \end{bmatrix} \tag{2.63}$$

Next, the constraint equation vector, $\boldsymbol{F}(\boldsymbol{X})$, is derived. In this example, the only requirement on the trajectory arc is termination at the target position,

$$\boldsymbol{r_d} = \begin{bmatrix} x_d \\ y_d \\ z_d \end{bmatrix} \tag{2.64}$$

This requirement is enforced through the constraint vector, $\boldsymbol{F}(\boldsymbol{X})$, written in the following form,

$$\boldsymbol{F}(\boldsymbol{X}) = \begin{bmatrix} x^t - x_d \\ y^t - y_d \\ z^t - z_d \end{bmatrix} \tag{2.65}$$

to satisfactorily produce the constraint equation, $\boldsymbol{F}(\boldsymbol{X}) = \boldsymbol{0}$. After the constraints are formulated, the Jacobian matrix, $D\boldsymbol{F}(\boldsymbol{X})$, is computed. Applying equation (2.56) to this example yields,

$$D\boldsymbol{F}(\boldsymbol{X}) = \frac{\partial \boldsymbol{F}(\boldsymbol{X})}{\partial \boldsymbol{X}} = \begin{bmatrix} \frac{\partial F_1}{\partial X_1} & \frac{\partial F_1}{\partial X_2} & \frac{\partial F_1}{\partial X_3} \\ \frac{\partial F_2}{\partial X_1} & \frac{\partial F_2}{\partial X_2} & \frac{\partial F_2}{\partial X_3} \\ \frac{\partial F_3}{\partial X_1} & \frac{\partial F_3}{\partial X_2} & \frac{\partial F_3}{\partial X_3} \end{bmatrix} = \begin{bmatrix} \frac{\partial x^t}{\partial \dot{x}_0} & \frac{\partial x^t}{\partial \dot{y}_0} & \frac{\partial x^t}{\partial \dot{z}_0} \\ \frac{\partial y^t}{\partial \dot{x}_0} & \frac{\partial y^t}{\partial \dot{y}_0} & \frac{\partial y^t}{\partial \dot{z}_0} \\ \frac{\partial z^t}{\partial \dot{x}_0} & \frac{\partial z^t}{\partial \dot{y}_0} & \frac{\partial z^t}{\partial \dot{z}_0} \end{bmatrix} \tag{2.66}$$

The elements of $D\boldsymbol{F}(\boldsymbol{X})$ all relate a component of the final state, $\boldsymbol{x^t}$, to a component in the initial state, $\boldsymbol{x_0}$, and, therefore, all must be elements of the state transition matrix, $\Phi(t, t_0)$. Consequently, equation (2.66) is written in the form,

$$D\boldsymbol{F}(\boldsymbol{X}) = \begin{bmatrix} \Phi_{14} & \Phi_{15} & \Phi_{16} \\ \Phi_{24} & \Phi_{25} & \Phi_{26} \\ \Phi_{34} & \Phi_{35} & \Phi_{36} \end{bmatrix} \tag{2.67}$$

where Φ_{ij} represents element (i, j) of the STM. Since there are an equal number of free variables and constraints $(n = m)$, $D\boldsymbol{F}(\boldsymbol{X})$ is square. Assuming the baseline trajectory is "reasonably close" to the desired trajectory, Newton's Method in equation (2.61) is used to iteratively solve for the unique solution in this fixed-time single shooting example.

2.4.2 Variable-Time Single Shooting

The objective of a variable-time single shooting algorithm is identical to that of the corresponding fixed-time version. The formulation, however, is slightly modified since the integration time, T, is allowed to vary as illustrated in Figure 2.7. In the

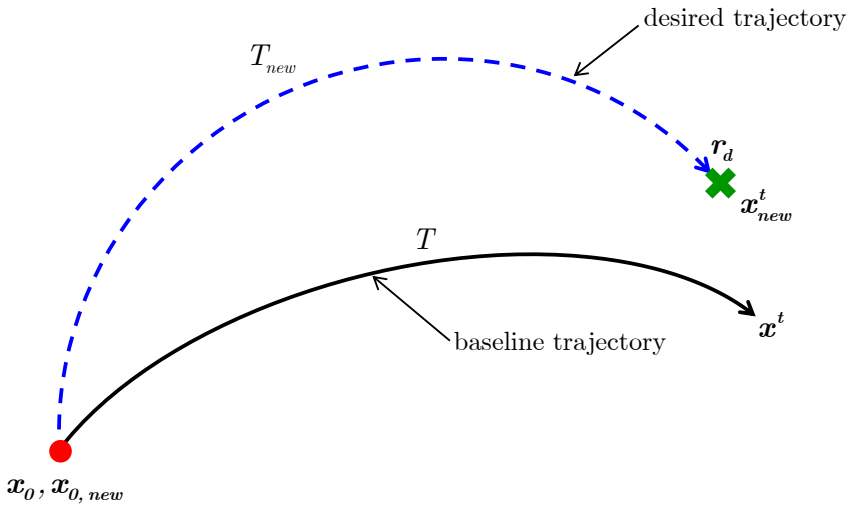

Figure 2.7. Variable-Time Single Shooting Algorithm

variable-time formulation, combining the initial velocity components as well as the integration time into the free variable vector, $\boldsymbol{X}$, yields,

$$\boldsymbol{X} = \begin{bmatrix} \dot{x}_0 \\ \dot{y}_0 \\ \dot{z}_0 \\ T \end{bmatrix} \tag{2.68}$$

The constraint vector is the same for both the fixed- and variable-time single shooting algorithms since the goal is identical, that is, deliver the trajectory to the desired position target location, $\boldsymbol{r_d}$. Thus,

$$\boldsymbol{F}(\boldsymbol{X}) = \begin{bmatrix} x^t - x_d \\ y^t - y_d \\ z^t - z_d \end{bmatrix} \tag{2.69}$$

The Jacobian matrix is not square, but each partial is still evaluated at the final time; the variation in time adds new partials as is apparent,

$$D\boldsymbol{F}(\boldsymbol{X}) = \frac{\partial \boldsymbol{F}(\boldsymbol{X})}{\partial \boldsymbol{X}} = \begin{bmatrix} \frac{\partial x^t}{\partial \dot{x}_0} & \frac{\partial x^t}{\partial \dot{y}_0} & \frac{\partial x^t}{\partial \dot{z}_0} & \frac{\partial x^t}{\partial T} \\ \frac{\partial y^t}{\partial \dot{x}_0} & \frac{\partial y^t}{\partial \dot{y}_0} & \frac{\partial y^t}{\partial \dot{z}_0} & \frac{\partial y^t}{\partial T} \\ \frac{\partial z^t}{\partial \dot{x}_0} & \frac{\partial z^t}{\partial \dot{y}_0} & \frac{\partial z^t}{\partial \dot{z}_0} & \frac{\partial z^t}{\partial T} \end{bmatrix} = \begin{bmatrix} \Phi_{14} & \Phi_{15} & \Phi_{16} & \dot{x}^t \\ \Phi_{24} & \Phi_{25} & \Phi_{26} & \dot{y}^t \\ \Phi_{34} & \Phi_{35} & \Phi_{36} & \dot{z}^t \end{bmatrix} \tag{2.70}$$

Note that the Jacobian matrix is rectangular since there are more free variables than constraints ($n > m$). From among an infinite number of possible solutions, the minimum norm solution to the variable-time single shooting problem is generated by iteratively solving equation (2.62).

2.4.3 Multiple Shooting: General Formulation

Multiple shooting algorithms are extremely powerful, but are still formulated using the simple method of constraints and free variables. Essentially, multiple shooting problems are a series of single shooting problems linked together. The difference between the schemes is the level of complexity, that is, multiple shooting algorithms

discretize a trajectory into a series of "patch points" and use *multiple* integrated segments to satisfy the trajectory constraints whereas single shooting algorithms use only one arc. Decomposing the trajectory into multiple segments, or arcs, offers key advantages over single shooting methods. First, both single and multiple shooting algorithms effectively exploit variational equations, that is, linear approximations relative to a baseline trajectory. As the variations are propagated, the linear approximation loses accuracy so using multiple arcs can substantially reduce the sensitivities typically associated with longer numerically integrated trajectory segments. Secondly, it is straightforward to apply path constraints at intermediate patch points in multiple shooting schemes to allow greater control over the shape of the trajectory as a whole. Constraints are easily added to the end points as well, if appropriate, as in the single shooting examples from the previous section. The general framework for a multiple shooting scheme appears in Figure 2.8. The vector, $\boldsymbol{x_i}$, represents the state at each patch point where each trajectory arc originates. The final integrated state along each segment, $\boldsymbol{x_i^t}\left(\boldsymbol{x_{i-1}}, T_{i-1}\right)$, is expressed in a shortened notation as $\boldsymbol{x_i^t}$. Note that the trajectory, as represented via a series of segments or arcs, is discontinuous, possibly in all seven states, at each patch point.

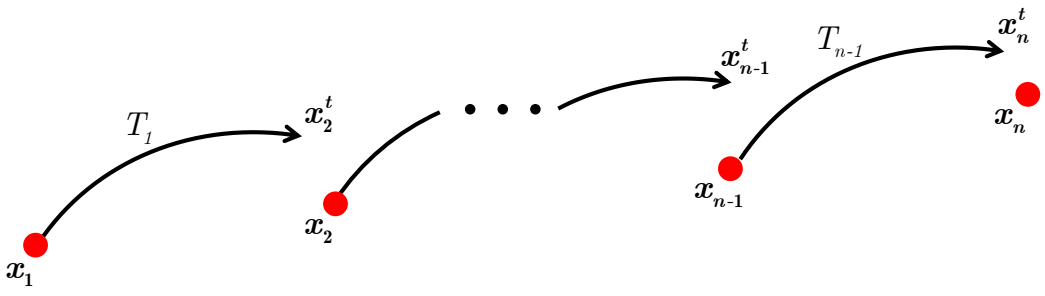

Figure 2.8. General Multiple Shooting Diagram

2.4.4 Fixed-Time Multiple Shooting

The fixed-time multiple shooting algorithm is derived much like the single shooting version, except that it employs multiple trajectory segments or arcs. To formulate the fixed-time, multiple shooting algorithm, the integration time corresponding to each segment, T_i, is fixed, so that the only free variables are the patch point states, $\boldsymbol{x_i}$. Stacking these states in the free variable vector yields,

$$\boldsymbol{X} = \begin{bmatrix} \boldsymbol{x_1} \\ \vdots \\ \boldsymbol{x_n} \end{bmatrix} \tag{2.71}$$

The vector $\boldsymbol{X}$ is configured as $6n \times 1$, where n denotes the number of patch points used to discretize the trajectory. In the general formulation of the multiple shooting problem, constraints are used only to enforce continuity between the end points. A discontinuity initially exists between the terminal state along each integrated segment and the state at the next patch point, i.e., the initial point on the next segment. The goal is to remove these discontinuities. These constraints are used to construct a constraint vector of length $6\,(n-1)$,

$$\boldsymbol{F}\,(\boldsymbol{X}) = \begin{bmatrix} \boldsymbol{x_2^t} - \boldsymbol{x_2} \\ \vdots \\ \boldsymbol{x_n^t} - \boldsymbol{x_n} \end{bmatrix} = \boldsymbol{0} \tag{2.72}$$

Satisfying these constraints produces a natural trajectory that is continuous in position and velocity to some desired tolerance. Formulating the Jacobian matrix again requires the appropriate partials relating variations in the constraints to changes in the free variables. For the general fixed-time, multiple shooting algorithm, a rectangular matrix results,

$$D\boldsymbol{F}\,(\boldsymbol{X}) = \begin{bmatrix} \frac{\partial \boldsymbol{x_2^t}}{\partial \boldsymbol{x_1}} & -\frac{\partial \boldsymbol{x_2}}{\partial \boldsymbol{x_2}} & & \\ & \ddots & \ddots & \\ & & \frac{\partial \boldsymbol{x_n^t}}{\partial \boldsymbol{x_{n-1}}} & -\frac{\partial \boldsymbol{x_n}}{\partial \boldsymbol{x_n}} \end{bmatrix} \tag{2.73}$$

The matrix is sized as $6(n-1) \times 6n$. The Jacobian is incorporated as part of an algorithm to iteratively compute a minimum norm solution, $\boldsymbol{X}^*$, to the fixed-time, multiple shooting problem. Substituting elements of the state transition matrix as appropriate, as well as 6×6 identity matrices, into equation (2.73) yields,

$$D\boldsymbol{F}(\boldsymbol{X}) = \begin{bmatrix} \Phi(t_2, t_1) & -I_{6x6} & & \\ & \ddots & \ddots & \\ & & \Phi(t_n, t_{n-1}) & -I_{6x6} \end{bmatrix} \tag{2.74}$$

Note that, for most multiple shooting formulations, $D\boldsymbol{F}(\boldsymbol{X})$ is a banded matrix whose sparse characteristics offer many numerical advantages, particularly when computing matrix inverses.

2.4.5 Variable-Time Multiple Shooting

The formulation of the general algorithm for variable-time multiple shooting is identical to that of the fixed-time algorithm except that the integration times, T_i, are allowed to vary. Adding these integration times to the free variable vector in equation (2.71) yields a new vector, $\boldsymbol{X}$, of length $7n$ ($6n$ patch point variables plus n time variables) represented as,

$$\boldsymbol{X} = \begin{bmatrix} \boldsymbol{x_1} \\ \vdots \\ \boldsymbol{x_n} \\ T_1 \\ \vdots \\ T_{n-1} \end{bmatrix} \tag{2.75}$$

The constraints are identical for the general fixed- and variable-time multiple shooting algorithms, so the constraint vector for the variable-time case is also written as,

$$\boldsymbol{F}(\boldsymbol{X}) = \begin{bmatrix} \boldsymbol{x_2^t} - \boldsymbol{x_2} \\ \vdots \\ \boldsymbol{x_n^t} - \boldsymbol{x_n} \end{bmatrix} = \boldsymbol{0} \tag{2.76}$$

The Jacobian matrix,

$$D\boldsymbol{F}(\boldsymbol{X}) = \begin{bmatrix} \frac{\partial \boldsymbol{x_2^t}}{\partial \boldsymbol{x_1}} & -\frac{\partial \boldsymbol{x_2}}{\partial \boldsymbol{x_2}} & & & \frac{\partial \boldsymbol{x_2^t}}{\partial T_1} & & \\ & \ddots & \ddots & & & \ddots & \\ & & \frac{\partial \boldsymbol{x_n^t}}{\partial \boldsymbol{x_{n-1}}} & -\frac{\partial \boldsymbol{x_n}}{\partial \boldsymbol{x_n}} & & & \frac{\partial \boldsymbol{x_n^t}}{\partial T_{n-1}} \end{bmatrix} \tag{2.77}$$

differs from that in the fixed-time case, however, because the partials associated with variations of the constraints are functions of each free variable, T_i, that is, the integration time. Note that $D\boldsymbol{F}(\boldsymbol{X})$ is a banded matrix in the variable-time algorithm as well. Lastly, the Jacobian is rewritten in terms of the elements of the various STMs, 6×6 identity matrices, and the time derivatives, $\dot{\boldsymbol{x}}_{\boldsymbol{i}}^{\boldsymbol{t}}$, i.e.,

$$D\boldsymbol{F}(\boldsymbol{X}) = \begin{bmatrix} \Phi(t_2, t_1) & -I_{6x6} & & & \dot{\boldsymbol{x}}_{\boldsymbol{2}}{}^t & & \\ & \ddots & \ddots & & & \ddots & \\ & & \Phi(t_n, t_{n-1}) & -I_{6x6} & & & \dot{\boldsymbol{x}}_{\boldsymbol{n}}{}^t \end{bmatrix} \tag{2.78}$$

These time derivatives are obtained by evaluating the vector field, $\boldsymbol{f}(\boldsymbol{x})$, at the final state along each integrated segment, $\boldsymbol{x_i^t}$. The Jacobian, $D\boldsymbol{F}(\boldsymbol{X})$ is again rectangular and of size $6(n-1) \times 7n$ so, consistent with the Jacobian defined in the fixed-time algorithm, the variable-time multiple shooting algorithm is solved iteratively and a minimum norm solution is computed.

2.4.6 Single-Parameter Continuation

While single and multiple shooting algorithms are useful for computing individual trajectories to meet some set of specifications, the converged trajectory that emerges is still only a point solution. It is generally beneficial to determine a range, or family, of related solutions whenever possible. Families of orbits offer insight into the general dynamical characteristics of a particular trajectory or arc as well as a glimpse into the dynamical framework in some region of space. Such families also provide various trajectory options in mission design scenarios. A variety of approaches are available to compute these families, but perhaps the simplest is a single or multiple shooting algorithm that is part of a single-parameter continuation scheme.

Single-parameter continuation schemes are very straightforward. First, any numerical differential corrections technique is applied to some initial guess and converges to a solution, this is, an orbit or trajectory arc. Then, a selected parameter associated with the converged solution is varied. Using the successful orbit with the perturbed parameter as a new guess, the differential corrections algorithm is applied again to produce a second converged solution. This process is repeated to construct an entire family of topologically related trajectories. Parameters commonly used in these schemes include energy, time of flight, or physical parameters such as one of the Cartesian coordinates that specify the initial position, i.e., x, y, or z position of a trajectory. To compute a family, the algorithm steps through increasing or decreasing values of the parameter. Single-parameter continuation schemes are general and are readily applicable to periodic or non-periodic orbits or trajectory arcs. A simple, representative family of arbitrary arcs appear in Figure 2.9; these example solutions can be generated through single-parameter continuation based on a parameter such as energy or time of flight.

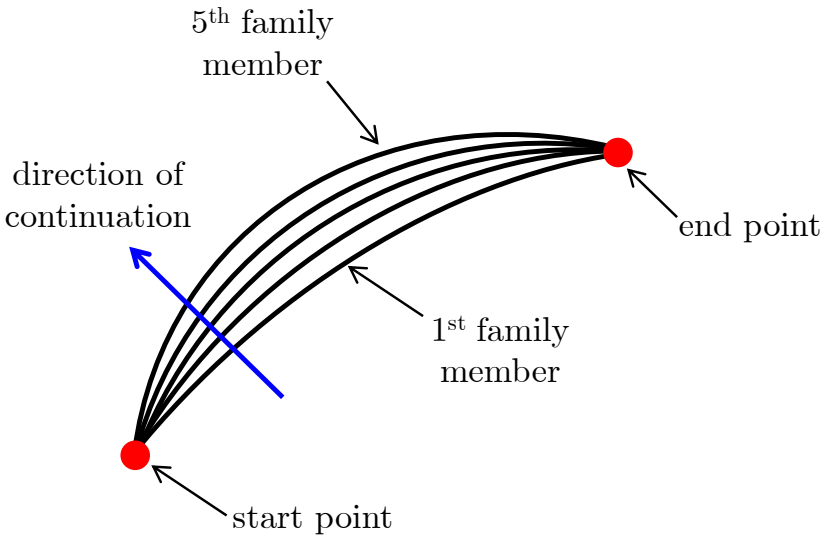

Figure 2.9. Arbitrary Continuation Example

2.4.7 Pseudo-Arclength Continuation

A special case of single-parameter continuation is the well-known pseudo-arclength continuation method [35, 36]. In typical single-parameter continuation schemes, the parameter selected to generate the family is generally simple and possesses some physical significance. Traditionally, then, a step represents a shift in a spatial direction or a gain/loss in some dynamical quantity such as orbital period or energy. In pseudo-arclength continuation schemes, however, a step is taken in a direction tangent to the family.

In basic single-parameter as well as pseudo-arclength continuation schemes, each new member, $\boldsymbol{X_i}$, of a family is computed based on the previously converged member of the family, $\boldsymbol{X^*_{i-1}}$. Note that both $\boldsymbol{X^*_{i-1}}$ and $\boldsymbol{X_i}$ represent free variable vectors within the context of a generalized differential corrections method. Recall that the original trajectory, $\boldsymbol{X^*_{i-1}}$, is a converged solution and satisfies the vector constraint equation,

$$\boldsymbol{F}\left(\boldsymbol{X^*_{i-1}}\right) = \boldsymbol{0} \tag{2.79}$$

For this application, there is one more free variable than constraint. Instead of stepping in a physical direction, or along a range of values associated with some dynamical quantity, as in conventional single-parameter continuation schemes, pseudo-arclength continuation schemes take steps of size Δs in a direction tangent to the family, i.e., in the direction of the next family member. The user-defined step size, Δs, typically does not possess any physical meaning. The tangent to the family has a dimension equal to the number of free variables in the problem. Given a converged family member, $\boldsymbol{X^*_{i-1}}$, a unit vector tangent to the family at $\boldsymbol{X^*_{i-1}}$ is obtained from the null vector, $\Delta\boldsymbol{X^*_{i-1}}$, of the Jacobian matrix, $D\boldsymbol{F}\left(\boldsymbol{X^*_{i-1}}\right)$. To require that the next family member, $\boldsymbol{X_i}$, is shifted by a step of size Δs along the family tangent vector, a pseudo-arclength constraint is added to the existing constraint vector, $\boldsymbol{F}\left(\boldsymbol{X_i}\right)$. This constraint is written as,

$$\left(\boldsymbol{X_i} - \boldsymbol{X^*_{i-1}}\right)^T \Delta\boldsymbol{X^*_{i-1}} - \Delta s = 0 \tag{2.80}$$

Thus, the constraint vector is augmented as follows,

$$\boldsymbol{G}\left(\boldsymbol{X_i}\right) = \begin{bmatrix} \boldsymbol{F}\left(\boldsymbol{X_i}\right) \\ \left(\boldsymbol{X_i} - \boldsymbol{X^*_{i-1}}\right)^T \Delta \boldsymbol{X^*_{i-1}} - \Delta s \end{bmatrix} = \boldsymbol{0} \tag{2.81}$$

The derivative of the augmented constraint vector, $\boldsymbol{G}\left(\boldsymbol{X_i}\right)$, with respect to the free variables, $\boldsymbol{X_i}$, yields an augmented Jacobian matrix,

$$D\boldsymbol{G}\left(\boldsymbol{X_i}\right) = \frac{\partial \boldsymbol{G}\left(\boldsymbol{X_i}\right)}{\partial \boldsymbol{X_i}} = \begin{bmatrix} D\boldsymbol{F}\left(\boldsymbol{X_i}\right) \\ \Delta \boldsymbol{X^*_{i-1}}^T \end{bmatrix} \tag{2.82}$$

which is square. A unique solution for the next member in the family, X_i^*, is generated via an iterative Newton's Method. The pseudo-arclength continuation approach is generally more robust than single-parameter continuation methods because it guarantees a unique family of solutions and requires no *a priori* knowledge regarding the evolution of the family from one member to the next. While Figure 2.9 is representative of an orbit family generated with either basic single-parameter or pseudo-arclength continuation, families generated using pseudo-arclength continuation schemes typically require less intuition.

2.5 Coordinate Frame Transformations

Coordinate frame transformations are often necessary to compute and view trajectories in multi-body regimes; alternate perspectives are frequently critical in design. For example, additional insight is available by viewing solutions from a circular restricted three-body problem in an inertial reference frame. Additionally, a converged solution in the CR3BP usually does not satisfy all the requirements if propagated in a higher-fidelity ephemeris model. Simulation in the ephemeris model requires that the trajectory first be transformed from the barycentered rotating frame to an inertial J2000 frame. The equations and methodologies required to implement both of these common coordinate frame transformations are detailed.

2.5.1 Transformation: Rotating Frame to Arbitrary Inertial Frame

To better understand trajectories designed in a CR3BP, it is often useful to view the path in a inertial reference frame as well. The transition between coordinate frames is achieved through a single transformation matrix. Recall that, by definition, the $\hat{x} - \hat{y}$ plane in the rotating frame is aligned with the inertial $\hat{X} - \hat{Y}$ plane for all time. Consequently, the position of P_3 in inertial coordinates is related to its position in rotating coordinates by a simple rotation about the $\hat{z}$ (or $\hat{Z}$) axis through the angle θ, as evidenced by the relationship

$$\begin{bmatrix} X \\ Y \\ Z \end{bmatrix} = \begin{bmatrix} \cos\theta & -\sin\theta & 0 \\ \sin\theta & \cos\theta & 0 \\ 0 & 0 & 1 \end{bmatrix} \begin{bmatrix} x \\ y \\ z \end{bmatrix} \tag{2.83}$$

where ${}^{I}C^{R}$ is the rotation matrix that transforms a vector from rotating coordinates to an inertial vector basis, that is,

$${}^{I}C^{R} = \begin{bmatrix} \cos\theta & -\sin\theta & 0 \\ \sin\theta & \cos\theta & 0 \\ 0 & 0 & 1 \end{bmatrix} \tag{2.84}$$

By convention, it is typically assumed that the rotating and inertial frames are initially aligned ($\theta = 0$ at $t = 0$), but this initial orientation is not required. However, if $\theta(0) \neq 0$, then the argument of the trigonometric functions is $(\theta - \theta_0)$ in the matrix ${}^{I}C^{R}$. To produce a relationship between the velocities, the kinematic derivative transformation equation,

$$\frac{{}^{I}d\boldsymbol{\rho}}{dt} = \frac{{}^{R}d\boldsymbol{\rho}}{dt} + {}^{I}\boldsymbol{\omega}^{R} \times \boldsymbol{\rho} \tag{2.85}$$

where ${}^{I}\boldsymbol{\omega}^{R} = n\hat{z}$, is first used to express the inertial velocity of P_3 in rotating coordinates,

$$\frac{{}^{I}d\boldsymbol{\rho}}{dt} = \dot{\boldsymbol{\rho}} = (\dot{x} - y)\,\hat{x} + (\dot{y} + x)\,\hat{y} + \dot{z}\hat{z} \tag{2.86}$$

where $\dot{\boldsymbol{\rho}}$ is a first derivative with respect to an inertial observer and is expressed in terms of unit vectors fixed in the rotating frame, R. Note that the nondimensional

mean motion, n, is not included in equation (2.86) since $n = 1$. Equation (2.83) is then used to express this velocity in terms of inertial coordinates. The expression relating the velocities can be combined with the expression relating positions to create a 6×6 transformation matrix,

$$\begin{bmatrix} X \\ Y \\ Z \\ \dot{X} \\ \dot{Y} \\ \dot{Z} \end{bmatrix} = \begin{bmatrix} \cos\theta & -\sin\theta & 0 & 0 & 0 & 0 \\ \sin\theta & \cos\theta & 0 & 0 & 0 & 0 \\ 0 & 0 & 1 & 0 & 0 & 0 \\ -\sin\theta & -\cos\theta & 0 & \cos\theta & -\sin\theta & 0 \\ \cos\theta & -\sin\theta & 0 & \sin\theta & \cos\theta & 0 \\ 0 & 0 & 0 & 0 & 0 & 1 \end{bmatrix} \begin{bmatrix} x \\ y \\ z \\ \dot{x} \\ \dot{y} \\ \dot{z} \end{bmatrix} \tag{2.87}$$

This matrix transforms a complete six-dimensional state with respect to an observer in frame R and expressed in terms of rotating coordinates, i.e., $\boldsymbol{x} = \begin{bmatrix} x & y & z & \dot{x} & \dot{y} & \dot{z} \end{bmatrix}^T$ to an inertial state expressed in inertial coordinates, i.e., $\boldsymbol{x} = \begin{bmatrix} X & Y & Z & \dot{X} & \dot{Y} & \dot{Z} \end{bmatrix}^T$ in a single step. Equation (2.87) is expressed more succinctly in the form,

$$\begin{bmatrix} X \\ Y \\ Z \\ \dot{X} \\ \dot{Y} \\ \dot{Z} \end{bmatrix} = \begin{bmatrix} {}^{I}C^{R} & 0_{3x3} \\ {}^{I}\dot{C}^{R} & {}^{I}C^{R} \end{bmatrix} \begin{bmatrix} x \\ y \\ z \\ \dot{x} \\ \dot{y} \\ \dot{z} \end{bmatrix} \tag{2.88}$$

Conveniently, the transformation in equation (2.88) is applicable for any base point in the CR3BP, e.g., either primary or their barycenter. If primary-centered inertial states are desired, the barycentered states from the CR3BP are simply translated to primary-centered states before the transformation is applied. Note that the inverse of the 6×6 transformation matrix is used to transform inertial states to rotating states. The entire transformation procedure is summarized in two simple steps below.

1. Shift CR3BP rotating state to desired base point
2. Apply transformation matrix in equation (2.87)

To transform an entire solution from the CR3BP to an inertial frame, steps 1 and 2 are repeated at each point along the integrated trajectory.

2.5.2 Transformation: Rotating Frame to Inertial J2000 Frame

To transition a six-dimensional state from the CR3BP to the ephemeris model, it is first necessary to translate the CR3BP data to an origin located at one of the primaries. Originally defined relative to the center of mass, the P_1-P_2 barycenter now holds no advantage since it is not fixed relative to either body in an ephemeris model. Additionally, if the ultimate goal is to transition the states and integrate in an ephemeris model, the vehicle and the gravitational forces must all be located relative to a central body. Once the data is expressed in terms of the appropriate set of unit vectors, the position and velocity states are also dimensionalized using the characteristic quantities defined in Section 2.1.3. The primary-centered, dimensional position vector, $\boldsymbol{r_{PC}}$, expressed in terms of unit vectors fixed in R, is then defined as,

$$\boldsymbol{r_{PC}} = \begin{bmatrix} x_{PC} \\ y_{PC} \\ z_{PC} \end{bmatrix} \tag{2.89}$$

Additional information is necessary to dimensionalize the velocity states. Ephemeris data (from the JPL DE405 ephemerides, for example) is used to construct an instantaneous rotating frame defined in terms of unit vectors expressed relative to the inertial J2000 frame. The instantaneous rotating axes are defined,

$$\hat{\hat{\boldsymbol{x}}} = \frac{\boldsymbol{R}}{R} \tag{2.90}$$

$$\hat{\hat{\boldsymbol{z}}} = \frac{\boldsymbol{R} \times \boldsymbol{V}}{\|\boldsymbol{R} \times \boldsymbol{V}\|} \tag{2.91}$$

$$\hat{\hat{\boldsymbol{y}}} = \hat{\hat{\boldsymbol{z}}} \times \hat{\hat{\boldsymbol{x}}} \tag{2.92}$$

where the symbols $\boldsymbol{R}$ and $\boldsymbol{V}$ are expressed in inertial J2000 coordinates and represent the ephemeris position and velocity vectors, respectively, of P_2 relative to P_1 as obtained directly from the ephemerides. For purposes of this derivation, a tilde denotes

any quantity that is defined instantaneously. These axes are defined in the inertial J2000 frame and, expressed as column vectors, are used to construct an instantaneous rotation matrix,

$$ {}^{I}C^{\tilde{R}} = \begin{bmatrix} \hat{\tilde{\boldsymbol{x}}} & \hat{\tilde{\boldsymbol{y}}} & \hat{\tilde{\boldsymbol{z}}} \end{bmatrix} = \begin{bmatrix} C_{11} & C_{12} & C_{13} \\ C_{21} & C_{22} & C_{23} \\ C_{31} & C_{32} & C_{33} \end{bmatrix} \tag{2.93} $$

where C_{ij} simply denotes the element (i, j) of the matrix ${}^{I}C^{\tilde{R}}$. This matrix transforms primary-centered positions expressed in a rotating frame to primary-centered states expressed in terms of an inertial J2000 frame, i.e.,

$$ \begin{bmatrix} X_{PC} \\ Y_{PC} \\ Z_{PC} \end{bmatrix} = \begin{bmatrix} C_{11} & C_{12} & C_{13} \\ C_{21} & C_{22} & C_{23} \\ C_{31} & C_{32} & C_{33} \end{bmatrix} \begin{bmatrix} x_{PC} \\ y_{PC} \\ z_{PC} \end{bmatrix} \tag{2.94} $$

The instantaneous angular velocity, $\dot{\tilde{\theta}}$, is derived from a two-body definition,

$$ \dot{\tilde{\theta}} = \frac{\tilde{h}}{R^2} = \frac{\|\boldsymbol{R} \times \boldsymbol{V}\|}{R^2} \tag{2.95} $$

Note that, because ephemeris information is dimensional, the instantaneous angular velocity has units of rad/s. The derivative frame transformation relationship is again employed for the kinematic expansion to rewrite the inertial velocity of P_3, expressed in primary-centered coordinates,

$$ \frac{{}^{I}d\boldsymbol{r_{PC}}}{dt} = \frac{{}^{R}d\boldsymbol{r_{PC}}}{dt} + {}^{I}\boldsymbol{\omega}^{\tilde{R}} \times \boldsymbol{r_{PC}} \tag{2.96} $$

$$ = \left(\dot{x}_{PC} - \dot{\tilde{\theta}} y_{PC}\right) \hat{\tilde{x}} + \left(\dot{y}_{PC} + \dot{\tilde{\theta}} x_{PC}\right) \hat{\tilde{y}} + \dot{z}_{PC} \hat{\tilde{z}} \tag{2.97} $$

where ${}^{I}\boldsymbol{\omega}^{\tilde{R}} = \dot{\tilde{\theta}}\hat{\tilde{z}}$. The inertial velocity of P_3 expressed in J2000 coordinates, i.e., $\begin{bmatrix}\dot{X} & \dot{Y} & \dot{Z}\end{bmatrix}^T$, is produced by transforming the velocity from equation (2.97) to J2000 coordinates via the transformation in equation (2.93), that is,

$$\begin{bmatrix}\dot{X}\\ \dot{Y}\\ \dot{Z}\end{bmatrix} = \begin{bmatrix}\dot{\tilde{\theta}}C_{12} & -\dot{\tilde{\theta}}C_{11} & 0 & C_{11} & C_{12} & C_{13}\\ \dot{\tilde{\theta}}C_{22} & -\dot{\tilde{\theta}}C_{21} & 0 & C_{21} & C_{22} & C_{23}\\ \dot{\tilde{\theta}}C_{32} & -\dot{\tilde{\theta}}C_{31} & 0 & C_{31} & C_{32} & C_{33}\end{bmatrix} \begin{bmatrix}x_{PC}\\ y_{PC}\\ z_{PC}\\ \dot{x}_{PC}\\ \dot{y}_{PC}\\ \dot{z}_{PC}\end{bmatrix} \tag{2.98}$$

Combining the transformation matrices in equations (2.93) and (2.98) results in a 6×6 transformation matrix that transforms a six-dimensional state from rotating to inertial J2000 coordinates in a single step, i.e.,

$$\begin{bmatrix}X\\ Y\\ Z\\ \dot{X}\\ \dot{Y}\\ \dot{Z}\end{bmatrix} = \begin{bmatrix}C_{11} & C_{12} & C_{13} & 0 & 0 & 0\\ C_{21} & C_{22} & C_{23} & 0 & 0 & 0\\ C_{31} & C_{32} & C_{33} & 0 & 0 & 0\\ \dot{\tilde{\theta}}C_{12} & -\dot{\tilde{\theta}}C_{11} & 0 & C_{11} & C_{12} & C_{13}\\ \dot{\tilde{\theta}}C_{22} & -\dot{\tilde{\theta}}C_{21} & 0 & C_{21} & C_{22} & C_{23}\\ \dot{\tilde{\theta}}C_{32} & -\dot{\tilde{\theta}}C_{31} & 0 & C_{31} & C_{32} & C_{33}\end{bmatrix} \begin{bmatrix}x_{PC}\\ y_{PC}\\ z_{PC}\\ \dot{x}_{PC}\\ \dot{y}_{PC}\\ \dot{z}_{PC}\end{bmatrix} \tag{2.99}$$

Since the elements in the lower left sub-matrix are dimensional, it is necessary that all states be dimensionalized before the application of the transformation. Additionally, the inverse transformation matrix transforms an inertial state expressed in inertial J2000 coordinates to a state expressed in rotating coordinates and viewed by a rotating observer.

Numerically, it is typical and frequently preferable to integrate the N-body relative equations of motion using nondimensional quantities. Thus, the last step is to nondimensionalize the inertial J2000 state obtained from the transformation using the instantaneous values of characteristic quantities length and time based on the instantaneous distance, R, between the two primaries of interest. The entire transformation procedure is summarized below:

1. Shift the rotating state from the CR3BP to a primary-centered rotating state
2. Dimensionalize the primary-centered rotating state using the standard characteristic quantities for the CR3BP
3. Apply the transformation matrix in equation (2.99)
4. Nondimensionalize the inertial J2000 state using instantaneously defined characteristic quantities

Steps 1–4 are applied to each point along a numerically integrated trajectory in the CR3BP to transform an entire solution to an inertial J2000 reference frame.

3. ORBIT COMPUTATION IN THE CIRCULAR RESTRICTED THREE-BODY PROBLEM

A wide variety of trajectories and orbits can be computed in the circular restricted three-body problem using only basic differential corrections algorithms. Families of periodic Lyapunov and halo orbits are generated using a single shooting strategy and pseudo-arclength continuation. A sample quasi-periodic Lissajous orbit in the vicinity of the L_2 libration point is generated in the Earth-Moon system using a simple technique that exploits the versatility of multiple shooting algorithms. Planar and out-of-plane free return trajectories between the Earth and Moon are determined using an initial guess from a conic two-body model. A planar free return trajectory is incorporated into the design of a four-phase mission that delivers a spacecraft from low Earth orbit into a lunar polar orbit. The total ΔV cost is presented.

3.1 Computation of Symmetric Periodic Orbits

Based fundamentally on the symmetric properties that exist across the $\hat{x}-\hat{z}$ plane in the CR3BP, simple single shooting algorithms are used to compute both planar Lyapunov orbits and non-planar halo orbits in the vicinity of the collinear libration points. Differential corrections algorithms are then augmented to compute families of periodic orbits by means of pseudo-arclength continuation. While an infinite number of planar and non-planar periodic orbits exist near all five libration points in the CR3BP, L_1 and L_2 generate the most immediate interest for mission applications in the Earth-Moon system and are the focus of this analysis.

3.1.1 Determining Planar Lyapunov Families: General Approach

Periodic, two-dimensional Lyapunov orbits are determined numerically using a variable-time single shooting algorithm that exploits both the planar and symmetric nature of the desired periodic solution to simplify the corrections process. Consider a trajectory with an initial state, $\boldsymbol{x_0}$, on the $\hat{x}$-axis and in the vicinity of a collinear libration point. This initial state lies in the $\hat{x} - \hat{z}$ plane such that the only non-zero components of the initial six-dimensional state vector are the x position, x_0, and y-component of velocity, $\dot{y}_0$, i.e.,

$$\boldsymbol{x_0} = \begin{bmatrix} x_0 & 0 & 0 & 0 & \dot{y}_0 & 0 \end{bmatrix}^T \tag{3.1}$$

Given this guess for an initial state, the goal is to determine a nearby solution with initial values x_0 and $\dot{y}_0$ such that the trajectory arrives perpendicularly at its next crossing of the $\hat{x} - \hat{z}$ plane. If both plane crossings are perpendicular, then symmetry is guaranteed and the second half of the orbit is determined by simply reflecting the solution across the $\hat{x} - \hat{z}$ plane. Figure 3.1 represents an initial guess and final numerically-determined, periodic orbit near L_1, but the same strategy is applicable to Lyapunov orbits about any of the collinear points. A complete Lyapunov orbit in the vicinity of L_1 appears in Figure 3.2.

3.1.2 Strategy for Computing Planar Lyapunov Families

To construct a variable-time single shooting algorithm to compute Lyapunov orbits, free variables are first identified. For each of the libration points, the initial x-position, x_0, initial y-velocity, $\dot{y}_0$, and integration time, T, are all allowed to vary. Additionally, the y-component of velocity, $\dot{y}^t$, corresponding to the state along the integrated path at the next plane crossing, must be constrained to ensure that the trajectory crosses the $\hat{x} - \hat{z}$ plane in the proper direction. About L_1, for example,

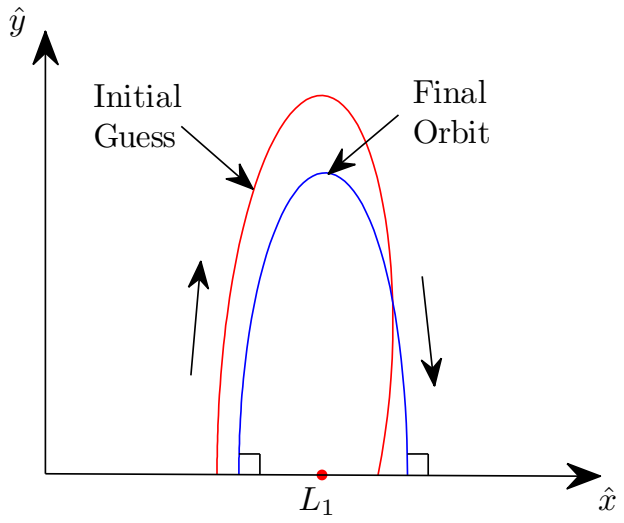

Figure 3.1. Strategy for Computing Lyapunov Orbits

Figure 3.1 indicates that when the trajectory next reaches the x-axis, it must cross in the -y direction. Thus, the inequality constraint,

$$\dot{y}^t < 0 \tag{3.2}$$

is applied. In practice, all constraints must be formulated such that $\boldsymbol{F}(\boldsymbol{X}) = \boldsymbol{0}$, so equation (3.2) is rewritten as the equality constraint,

$$\dot{y}^t + \beta^2 = 0 \tag{3.3}$$

where β is a slack variable. Including the slack variable with the other three design variables produces the free variable vector,

$$\boldsymbol{X} = \begin{bmatrix} x_0 & \dot{y}_0 & T & \beta \end{bmatrix}^T \tag{3.4}$$

The constraint equations, $\boldsymbol{F}(\boldsymbol{X}) = \boldsymbol{0}$, must also be determined. The requirements that the orbit terminate at the $\hat{x} - \hat{z}$ plane and that it arrives perpendicularly yields the following two constraint equations, respectively,

$$y^t = 0, \tag{3.5}$$

$$\dot{x}^t = 0 \tag{3.6}$$

Combining these equations with equation (3.3) results in the three-element constraint vector,

$$\boldsymbol{F}(\boldsymbol{X}) = \begin{bmatrix} y^t & \dot{x}^t & \dot{y}^t + \beta^2 \end{bmatrix}^T = \mathbf{0} \tag{3.7}$$

The derivatives of the scalar constraint expressions with respect to the free variables yields the rectangular Jacobian matrix,

$$D\boldsymbol{F}(\boldsymbol{X}) = \frac{\partial \boldsymbol{F}(\boldsymbol{X})}{\partial \boldsymbol{X}} = \begin{bmatrix} \Phi_{21} & \Phi_{25} & \dot{y}^t & 0 \\ \Phi_{41} & \Phi_{45} & \ddot{x}^t & 0 \\ \Phi_{51} & \Phi_{55} & \ddot{y}^t & 2\beta \end{bmatrix}, \tag{3.8}$$

where Φ_{ij} represents element (i, j) of the state transition matrix $\Phi(t, t_0)$ and $t = t_0 + T$. Note that the elements of the third column of $D\boldsymbol{F}(\boldsymbol{X})$ are determined by evaluating the equations of motion at the final state along the integrated trajectory, $\boldsymbol{x^t}$. A complete Lyapunov orbit in the vicinity of L_1 that is converged via a Newton's Method appears in Figure 3.2.

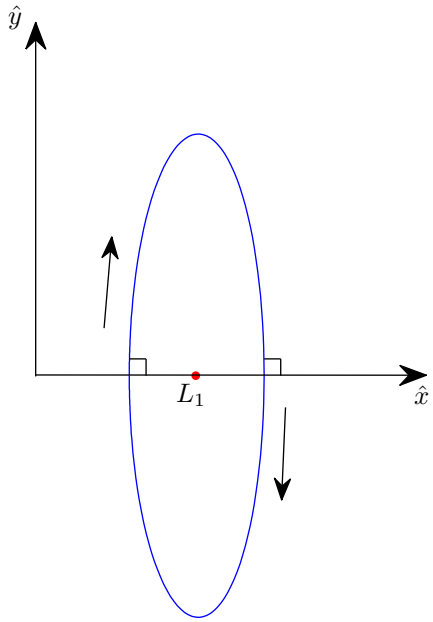

Figure 3.2. Converged Lyapunov Orbit Near L_1

The differential corrections process is initiated with a first guess obtained from well-known linear solutions relative to the collinear points [16]. These approximations analytically represent Lyapunov orbits in the immediate vicinity of the libration points. Using the analytical initial guess, a converged L_1 Lyapunov orbit is with an orbital period of 11.69 days and a maximum y-amplitude of 0.00576 nondimensional units (2200 km) is obtained iteratively using a minimum norm solution. Once a single periodic orbit is available, subsequent members of a Lyapunov family are obtained using the pseudo-arclength continuation method discussed in Section 2.4.7. Implementing the continuation scheme requires only a slight modification to the variable-time single shooting algorithm. The pseudo-arclength constraint is enforced with the augmented constraint vector,

$$\boldsymbol{G}(\boldsymbol{X}) = \begin{bmatrix} \boldsymbol{F}(\boldsymbol{X}) \\ \left(\boldsymbol{X_i} - \boldsymbol{X^*_{i-1}}\right)^T \Delta \boldsymbol{X^*_{i-1}} - \Delta s \end{bmatrix} = \boldsymbol{0} \tag{3.9}$$

where the size of the pseudo-arclength step, Δs, is typically determined by user experience and may vary based on the collinear libration point of interest. The augmented Jacobian matrix,

$$D\boldsymbol{G}(\boldsymbol{X}) = \frac{\partial \boldsymbol{G}(\boldsymbol{X})}{\partial \boldsymbol{X}} = \begin{bmatrix} D\boldsymbol{F}(\boldsymbol{X}) \\ \Delta \boldsymbol{X^*_{i-1}}^T \end{bmatrix} \tag{3.10}$$

is square so a simple Newton's Method is used to compute subsequent members of the Lyapunov families.

3.1.3 Numerical Examples: L_1 and L_2 Lyapunov Families

Using an analytical initial guess and suitable pseudo-arclength step size, Δs, many members of the L_1 and L_2 Lyapunov families are computed. By analyzing the changes in stability across these periodic families, bifurcations with other families of periodic orbits are detected [36, 37]. In each Lyapunov family, there exists a well-known bifurcation with a corresponding family of periodic halo orbits, and thus, about each libration point, there is a periodic orbit that is common to both a Lyapunov and a

halo family. Figures 3.3 and 3.4 illustrate families of Lyapunov orbits in the vicinity of both the L_1 and L_2 points, respectively. Note that each family includes an infinite number of periodic orbits, so only a portion of each family, that is, a finite number of orbits, appears. The libration points are red and orbits that bifurcate with a corresponding halo family are indicated in green. The size of the Moon is pictured to scale, as well. The Lyapunov orbits in both families move in a clockwise direction about their respective libration points as indicated. The smallest L_1 Lyapunov orbit that appears in Figure 3.3 possesses a maximum y-amplitude equal to 0.00576 nondimensional units (2200 km) and an orbital period of 11.69 days. The largest Lyapunov orbit in the figure is measured with a maximum y-amplitude of 0.520 nondimensional units (200,000 km) and a period of 26.47 days. Similarly, the maximum y-amplitudes for the portion of the orbits in the L_2 Lyapunov family in Figure 3.4 range from 0.00473 to 0.524 nondimensional units (1800 to 201,000 km); the corresponding orbital periods vary from 14.65 to 28.13 days.

3.1.4 Strategy for Computing Halo Families

Using the same algorithm that is employed to compute the Lyapunov families, it is straightforward to compute the halo families as well. Starting from the bifurcating Lyapunov orbit, there are a variety of numerical techniques for following the branch of the bifurcation diagram associated with the halo family [36]. Perhaps the simplest way to initiate the computation of the halo family, however, is to perturb the bifurcating Lyapunov orbit slightly in the $\pm z$-direction and compute a new symmetric periodic orbit. A perturbation in the $+z$ direction leads to solutions in a northern halo family while perturbing in the $-z$ direction produces orbits that belong a southern halo family.

In practice, the algorithm is straightforward. First, the initial condition corresponding to a bifurcating Lyapunov orbit is perturbed by a small amount in the $+z$-direction (for a northern halo family). Equations (3.4), (3.7), and (3.8) – previ-

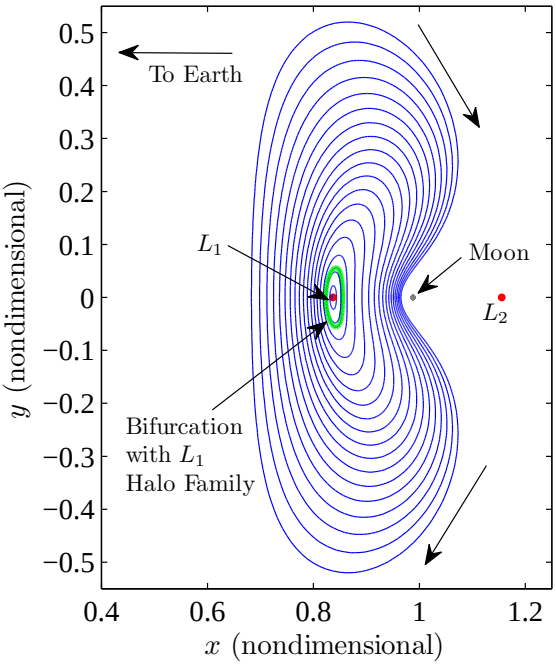

Figure 3.3. L_1 Lyapunov Family

ously used to generate Lyapunov orbits – are then used to generate a periodic halo orbit, as well. This new orbit represents the first out-of-plane member of the halo family. Lastly, equations (3.4), (3.9), and (3.10) are employed to compute a family of halo orbits via the pseudo-arclength continuation method.

3.1.5 Numerical Examples: L_1 and L_2 Halo Families

Exploiting the general nature of the differential corrections algorithms, families of halo orbits in the vicinity of L_1 and L_2 are generated using the identical numerical methods that successfully created the L_1 and L_2 Lyapunov families. Northern L_1 and L_2 halo families appear in the following figures. Figures 3.5 and 3.6 illustrate three-dimensional and orthogonal views of the L_1 northern halo family, respectively. The same information is presented for the family of northern L_2 halo orbits in Figures

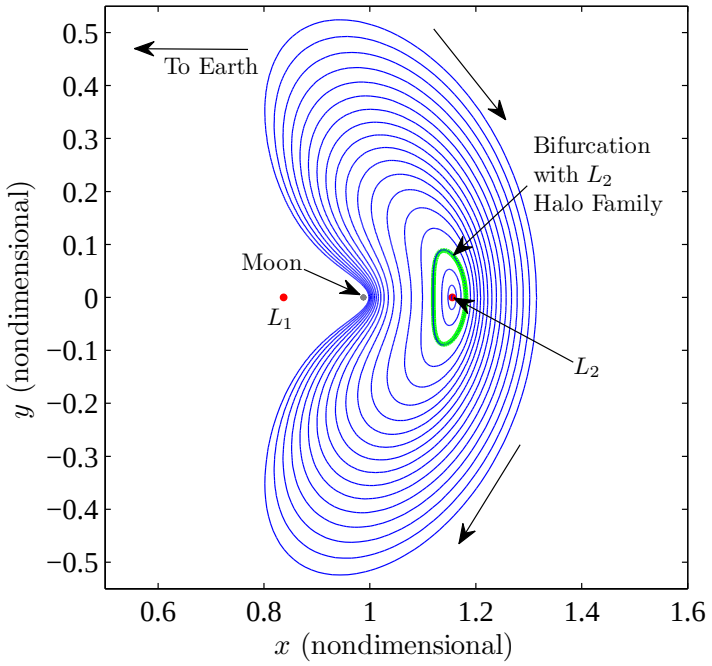

Figure 3.4. L_2 Lyapunov Family

3.7 and 3.8. For both families, the positions of the Moon and libration points are indicated, as well, along with the bifurcating orbits that are shared with the corresponding Lyapunov families. For the L_1 halo orbits that appear in Figures 3.5 and 3.6, the maximum z-amplitudes range from 0 to 0.720 nondimensional units (0 to 277,000 km) while the orbital periods vary from 11.92 days to 12.99 days. For the L_2 halo family, the bifurcating orbit that is shared with the planar L_2 Lyapunov family has an orbital period of 14.84 days. The final member of the L_2 halo family that appears in the figure possesses a maximum z-amplitude of 0.170 nondimensional units (65,000 km) and an orbital period of 5.71 days.

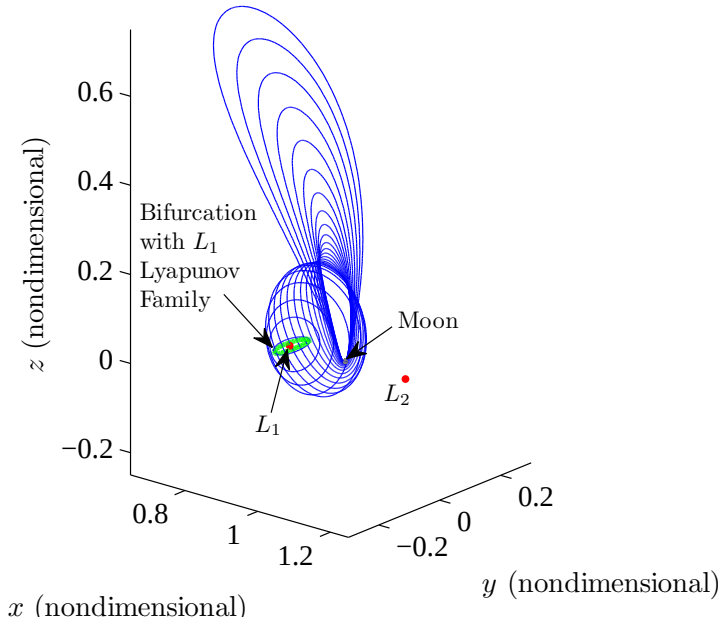

Figure 3.5. A Portion of the Northern L_1 Halo Family

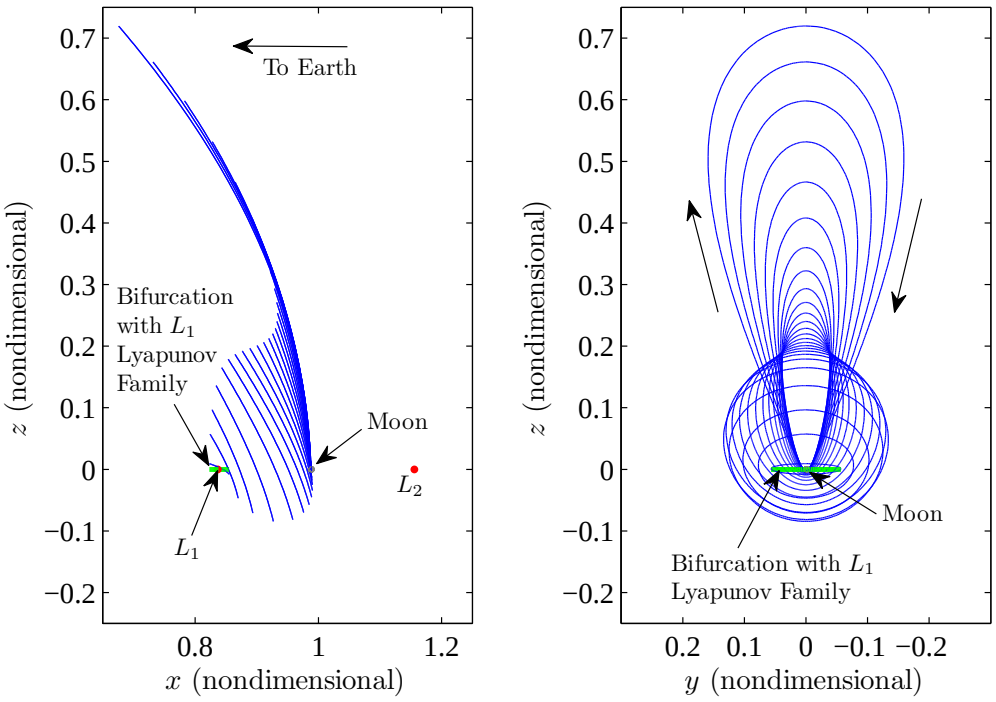

Figure 3.6. Orthogonal Views of the Northern L_1 Halo Family

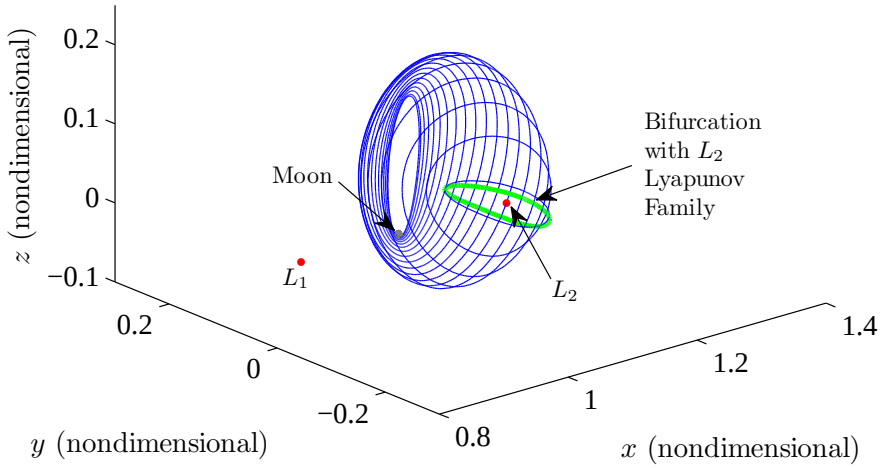

Figure 3.7. A Portion of the Northern L_2 Halo Family

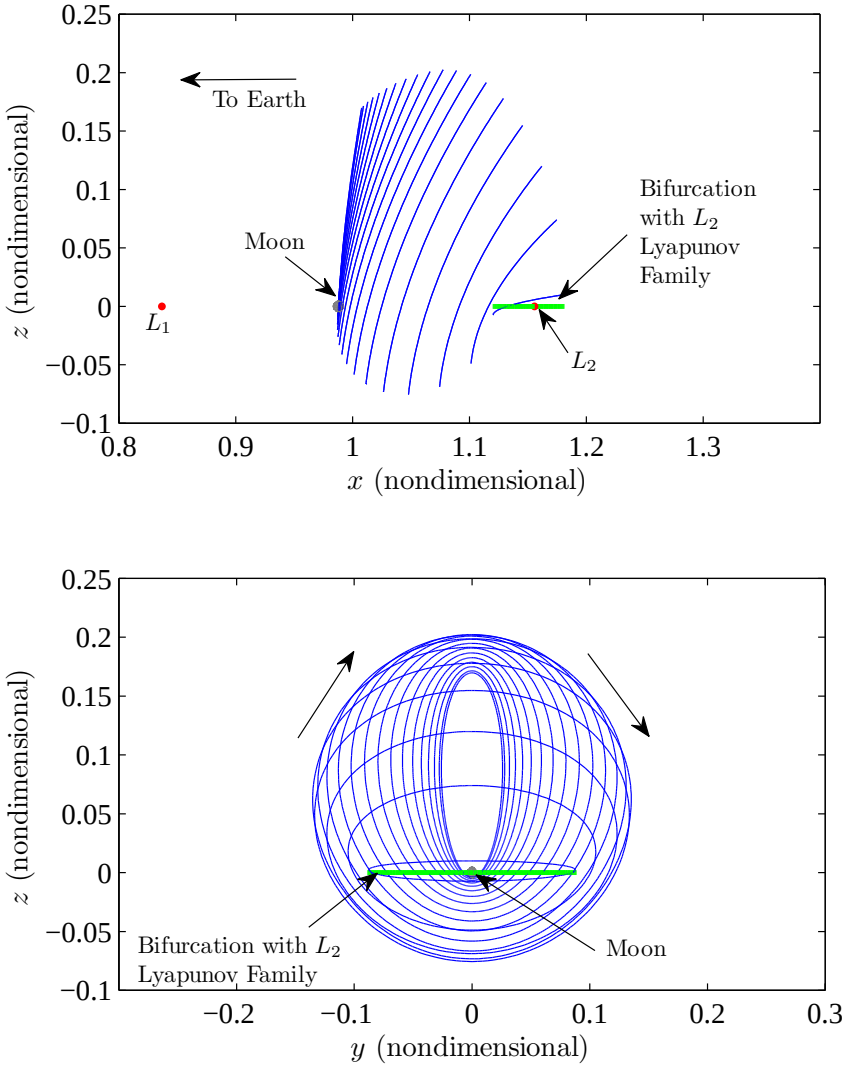

Figure 3.8. Orthogonal Views of the Northern L_2 Halo Family

3.2 Computation of Quasi-Periodic Lissajous Orbits

Lissajous orbits are bounded, quasi-periodic solutions associated with periodic orbits in the CR3BP. Because these orbits can possess a wide range of in-plane and out-of-plane amplitudes, Lissajous orbits are desirable for mission design applications because they can greatly increase the design space. However, since these trajectories are quasi-periodic and do not repeat exactly, Lissajous orbits are generally more difficult to compute than perfectly periodic orbits.

As with the design of many types of trajectories in multi-body regimes, the main difficulty resides in obtaining a suitable initial guess. Traditionally, analytical approximations about the collinear libration points are frequently employed as a means for delivering initial conditions to a differential corrections procedure. First-, third-, and fourth-order analytical solutions are discussed in references [38–40]. Of course, as with all linearizations, these solutions are most accurate in the immediate vicinity of the libration points. Thus, these analytical approximations present difficulties when computing larger amplitude Lissajous orbits. More recently, Olikara and Howell have demonstrated computational methods and continuation schemes for computing Lissajous orbits of any size by directly generating the invariant tori that define them [41]. Neither approach is trivial to implement, however. Thus, the emphasis of this section is on a simple, pragmatic approach to compute Lissajous orbits, an approach that can easily be extended to higher-fidelity models. A straightforward strategy relying on previously presented numerical methods and minimal user intuition is discussed. Numerical examples are presented.

3.2.1 Strategy for Computing Lissajous Orbits

While Lissajous orbits have been successfully determined by both (i) computing invariant tori directly and (ii) using analytical approximations to determine an initial guess for a differential corrections procedure, it is often possible to calculate them using only user intuition and a straightforward multiple shooting algorithm as well.

The first step is the selection of the maximum y- and z-amplitudes for the desired orbit, that is, A_y and A_z, respectively. A planar Lyapunov orbit, with the appropriate y-amplitude, is then identified and discretized into an appropriate number of patch points. For this application, four to eight patch points is typically sufficient. These patch points are stacked to create a Lyapunov orbit with a desired number of revolutions.

To compute a Lissajous orbit, then, the basic fixed-time multiple shooting algorithm, as discussed in Section 2.4.3, is used with one addition. To control the general shape of the orbit, a single constraint is added to fix the z-amplitude at a patch point along the first revolution of the Lyapunov orbit; the patch point corresponds to a location along the first revolution that coincides with a point of maximum y-amplitude. The multiple shooting algorithm enforces this constraint along with continuity at the internal patch points to produce a natural quasi-periodic solution. In Figure 3.9, two plots appear. A baseline discretized L_2 Lyapunov orbit is plotted and the patch points are indicated (top). Then, one patch point is modified by adding a z-component to the position vector. The modified guess appears in Figure 3.9 (bottom), and is used to control the z-amplitude so that the algorithm delivers the desired Lissajous orbit. A simple continuation scheme, based on z-amplitude as the continuation parameter, is used to construct Lissajous orbits with a wide range of A_z values.

3.2.2 Numerical Example: L_2 Lissajous Orbit

To demonstrate the strategy to compute quasi-periodic orbits, a Lissajous trajectory of size $A_y \approx 0.16$ and $A_z \approx 0.08$ (nondimensional units) is generated relative to the L_2 libration point, without the use of analytical approximations or a more complex dynamical systems approach. Beginning with the Lyapunov orbit in Figure 3.9 which is planar with $A_y \approx 0.16$, the z-amplitude of the patch point corresponding to the location of maximum $+y$-amplitude on the first revolution is increased. Then, a fixed-time multiple shooting algorithm and single-parameter continuation are im-

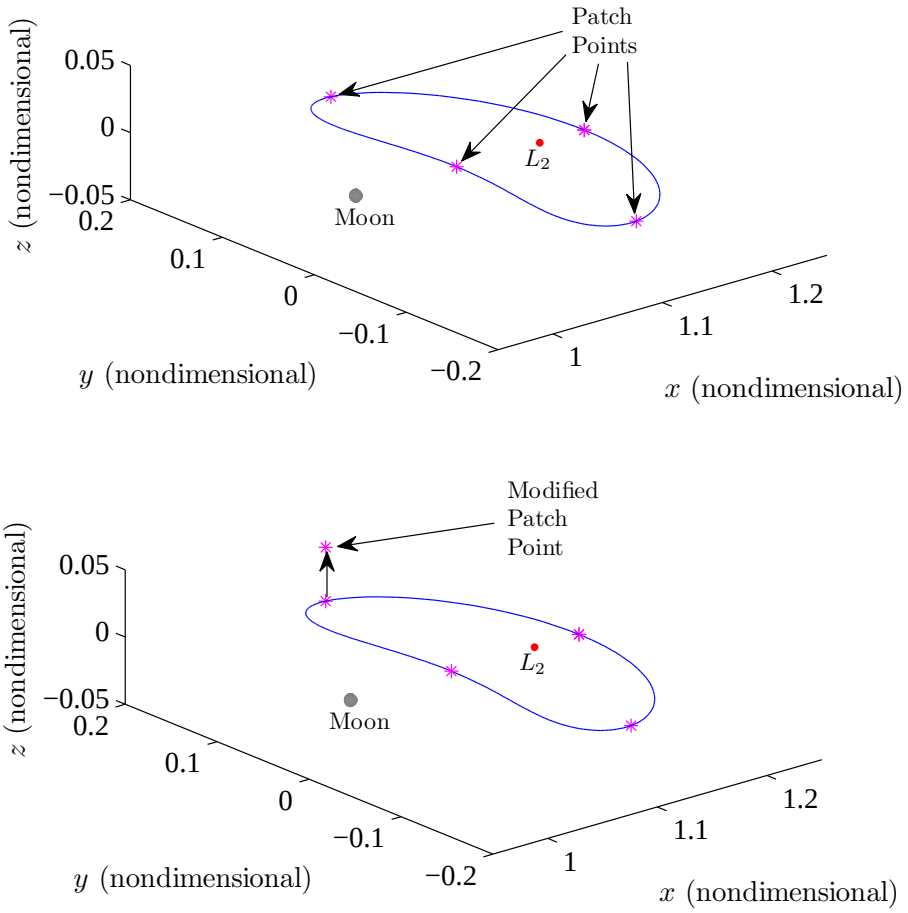

Figure 3.9. Patch Point Selection to Compute L_2 Lissajous Orbit via Multiple Shooting

plemented. Only two continuation steps are required to obtain the desired Lissajous orbit with a z-amplitude of $A_z \approx 0.08$.

The converged L_2 Lissajous orbit appears in Figure 3.10; *ten* revolutions are incorporated. Selected orthogonal views are plotted in Figure 3.11. As a means of comparison, this orbit is similar in both size and shape to the proposed L_2 Lissajous orbit for the ARTEMIS P_2 spacecraft. Note that this orbit is intended only as a simple example and additional constraints can be added to further control the size and shape of a desired Lissajous orbit.

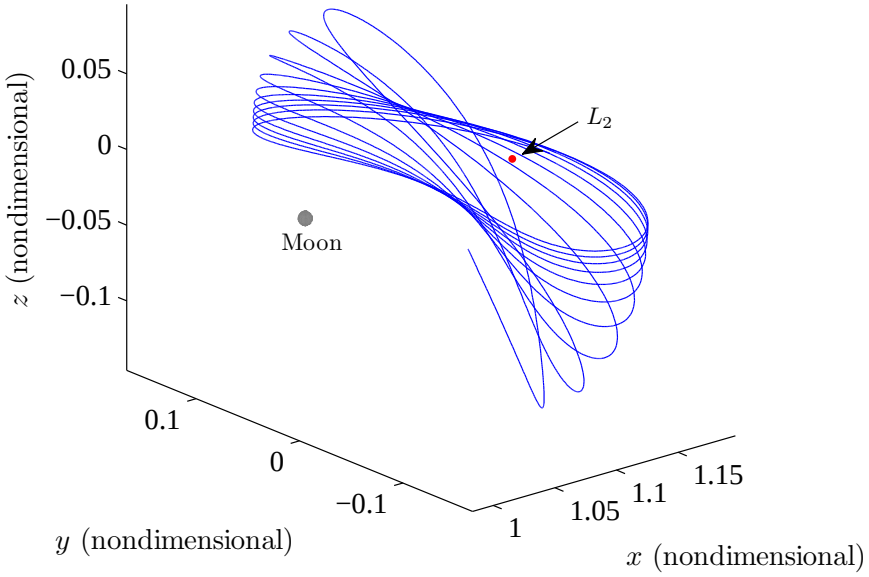

Figure 3.10. Final L_2 Lissajous Orbit in CR3B Model

3.3 Computation of Lunar Free Return Trajectories

Free return trajectories offer one possible Earth-Moon transfer option and have been been studied for decades because of their applicability to manned space flight. Free returns were successfully employed as the basic trajectory design concept for several Apollo missions during the 1960s. These types of transfers are ideal from a safety perspective because, in the event of communication difficulties or crew emer-

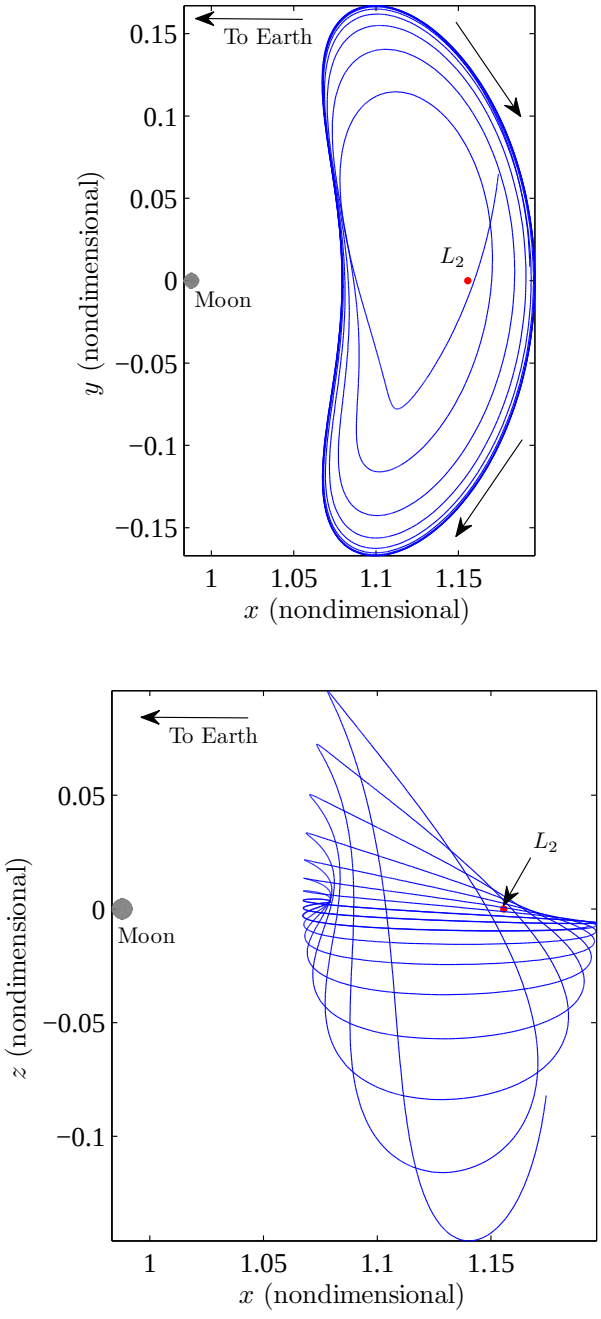

Figure 3.11. Orthogonal Views of a L_2 Lissajous Orbit

gencies, free returns guarantee safe passage back toward the Earth from the vicinity of the Moon. Fortunately, free return transfers are desirable from a computational standpoint as well, because robust algorithms exist for generating initial conditions that allow for the convergence of free return trajectories in multi-body dynamical models. This section uses patched conic models to determine initial conditions for symmetric free return trajectories in the CR3BP. Two-body analysis does not always produce initial conditions which converge to trajectories that retain desirable design characteristics in the full ephemeris model. Thus, the CR3BP serves as an important intermediate step. From a two-body initial guess, multiple shooting and single-parameter continuation schemes are used to produce planar and three-dimensional families of free return trajectories in the circular restricted three-body problem.

3.3.1 Obtaining an Initial Guess from Two-Body Analysis

Patched conic solutions to the Earth-Moon free return problem, and strategies to transition these solutions to multi-body regimes, have been known for many years [24, 25, 27]. In reference [27], Jesick and Ocampo detail an automated procedure for generating free return orbits in the CR3BP by first obtaining an initial guess from two-body analysis. This section is intended to summarize their procedure, but the reference should be consulted for a more detailed discussion.

The goal with this procedure is the determination of the trans-lunar injection (TLI) conditions near Earth that result in a trajectory that travels to the vicinity of the Moon and returns to Earth without any additional ΔV maneuvers. From a patched conic perspective, the objective is to link an Earth-centered departure ellipse and a Moon-centered hyperbola that shifts the velocity vector by the precise the amount required to place the spacecraft on a return trajectory to Earth. Essentially, the Earth-centered ellipse and Moon-centered hyperbola are patched together at the lunar sphere of influence (LSOI) which approximates the region where lunar gravity

is the dominant force on the spacecraft. The radius of the LSOI, R_{LSOI}, is roughly $66,400$ kilometers, as calculated from the equation,

$$R_{LSOI} = l^* \left(\frac{\mu_M}{\mu_E} \right)^{2/5} \tag{3.11}$$

where μ_M and μ_E represent the gravitational parameters of the Moon and Earth, respectively.

The algorithm discussed in [27] is capable of generating free return trajectories with prograde or retrograde Earth departures and either cislunar or circumlunar passages. Cislunar trajectories possess lunar periapses that occur on the near side of the Moon. Conversely, the lunar periapses along circumlunar trajectories are located on the far side of the Moon. Since they are most relevant to manned space applications, only circumlunar free return trajectories with prograde departures are considered here. A patched conic representation of a prograde circumlunar free return trajectory, adapted from reference [27], appears in Figure 3.12; assume that the trajectory is two-dimensional. Note that the figure is not drawn to scale.

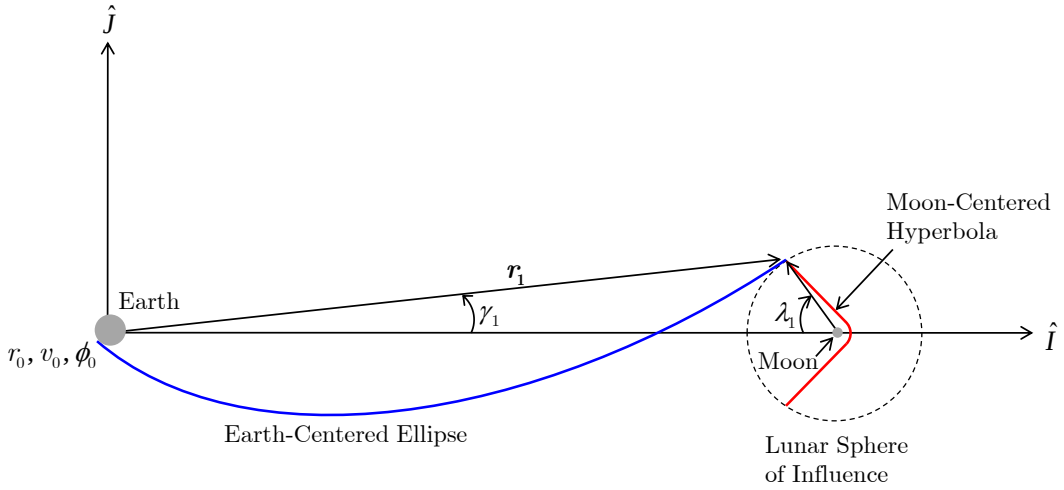

Figure 3.12. Patched Conic Model for Computing Free Return Trajectories

The Earth-centered inertial coordinate frame is defined such that the $\hat{I}$-axis is coincident with the Earth-Moon line when the spacecraft reaches the lunar sphere

of influence. The plane of motion is defined as the inertial $\hat{I}$-$\hat{J}$ plane. Thus, the Moon and the LSOI appear in the figure at this instant, that is, the time of entry to the lunar sphere of influence (LSOI). The spacecraft initial conditions along the blue, Earth-centered ellipse are denoted with a subscript "0" and include the Earth-centered orbital radius, r_0, velocity magnitude, v_0, and flight path angle, ϕ_0 at TLI. The Earth-centered position vector, $\boldsymbol{r_1}$, LSOI entry angle, λ_1, and the angle between $\boldsymbol{r_1}$ and the $\hat{I}$-axis, γ_1, are all denoted with a subscript "1" to signify that they exist at the LSOI entry condition. Of course, once the spacecraft enters the LSOI, its path relative to the Moon is hyperbolic. It is assumed that, when computing the hyperbolic orbit plotted in red, that the Moon is fixed while the spacecraft is within the LSOI.

To determine the TLI conditions that are necessary for a lunar free return trajectory, the size and orientation of the Earth-centered ellipse are defined by four of the parameters mentioned previously, r_0, v_0, and the angles ϕ_0 and λ_1. The initial geocentric radius, r_0, is a user-selected variable so the value is known. The flight path angle at TLI, ϕ_0, is set to 0° to reduce the complexity of the problem. Once the LSOI entry angle, λ_1, is selected, the orbital radius at LSOI entry with respect to the Earth, r_1, is determined from the law of cosines, i.e.,

$$r_1 = \sqrt{R_{LSOI}^2 + l^{*2} - 2R_{LSOI}l^* \cos\lambda_1} \tag{3.12}$$

Equation (3.12) is then used to compute the minimum TLI velocity, v_0, that is, the velocity necessary to reach the lunar sphere of influence,

$$v_0 = \sqrt{2\mu_E \left(\frac{1}{r_0} - \frac{1}{r_0 + r_1}\right)} \tag{3.13}$$

Of course, equation (3.13) is a function of λ_1 through the distance r_1. To determine a free return trajectory in the patched conic model, a root finding algorithm, such as bisection, is then used to compute the LSOI entry angle, λ_1. The desirable entry angle is that one that drives the argument of periapsis defined for the hyperbola relative to $\hat{I}$, to a value that is approximately 0°. Satisfying this condition ensures a symmetric

free return trajectory. By convention, λ_1 is set to 90° to initiate the process. Jesick and Ocampo then transform the initial TLI state into a barycentered rotating frame for use as an initial guess in a differential corrections algorithm to compute a free return trajectory in the circular restricted-three body problem. It is only necessary to focus on the outbound leg since the free return trajectory is symmetric in this formulation and the inbound leg is easily obtained by reflection across the $\hat{x} - \hat{z}$ plane in the CR3BP. This entire procedure is summarized below:

1. Select r_0
2. Set $\phi_0 = 0°$
3. Guess λ_1
4. Calculate r_1 and v_0
5. Calculate argument of periapsis for the lunar hyperbola
6. Iterate on steps 3–5 to drive argument of perilune $\approx 0°$
7. Transform TLI initial condition to barycentered rotating frame
8. Compute CR3BP free return trajectory using differential corrections procedure

This concludes the summary of [27] and a modified strategy used to compute free returns throughout this analysis is now introduced.

The process to compute a free return trajectory in the CR3BP is shortened considerably if, instead of computing a free return in the patched conic model first, this step is skipped entirely and a root finding algorithm is, instead, used to determine a free return trajectory directly in the CR3BP. To shorten the procedure, the initial TLI condition is transformed directly to the CR3BP immediately after completing steps 1–4 above. The initial condition is integrated forward in time until it returns to the x-axis in the vicinity of the Moon. The final x-velocity, $\dot{x}_f$, at the x-axis crossing is now known and a bisection algorithm varies the LSOI entry angle, λ_1, until $\dot{x}_f \approx 0$.

The outbound leg of a symmetric free return trajectory in the CR3BP is achieved once this condition is satisfied. This abbreviated process is summarized in the list below:

1. Select r_0
2. Set $\phi_0 = 0°$
3. Guess λ_1
4. Calculate r_1 and v_0
5. Transform TLI initial condition to barycentered rotating frame
6. Integrate trajectory in CR3BP to obtain $\dot{x}_f$
7. Iterate on steps 3–6 to produce $\dot{x}_f \approx 0$ in the CR3BP

This modified scheme is analogous to the method in [27], but requires less conic analysis to generate free return trajectories in the circular restricted three-body problem. The outbound leg of a lunar free return trajectory in the CR3BP, with an initial Earth altitude of 185 kilometers, appears in Figure 3.13. Note that this trajectory actually impacts the lunar surface since altitude constraints have not yet been imposed.

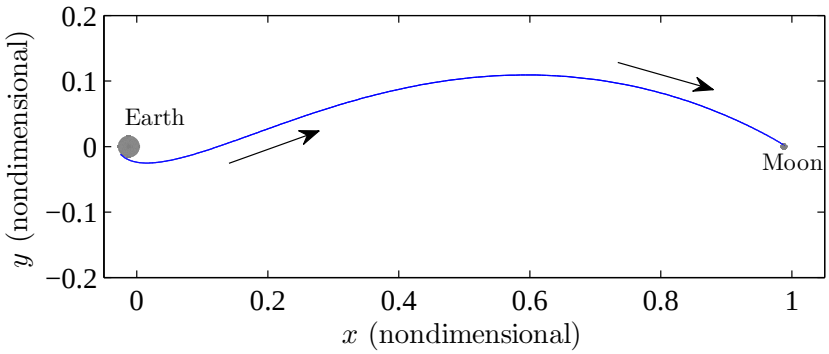

Figure 3.13. Outbound Leg of Free Return Trajectory in the CR3BP

3.3.2 Constraining Altitude and Flight Path Angle

If free return trajectories in the CR3BP are required only to be symmetric, undesired consequences might result, such as the impact trajectory in Figure 3.13. Thus, additional constraints are required. Formulating the problem within the context of a multiple shooting scheme, the constraints can easily be incorporated. To construct families of free return trajectories, assume that perilune altitude, Earth departure altitude, and flight path angle at Earth departure are included as constraints. To formulate the altitude constraint, the position of the spacecraft is first expressed relative to the primaries. Illustrated in Figure 3.14, the vector relationships are apparent between the position vectors $\boldsymbol{r_{E-s/c}}$ and $\boldsymbol{r_{M-s/c}}$, which represent the position of the spacecraft relative to the Earth and Moon, respectively, and the known position of the spacecraft with respect to the barycenter, $\boldsymbol{r_{BC-s/c}}$. The barycenter is again denoted

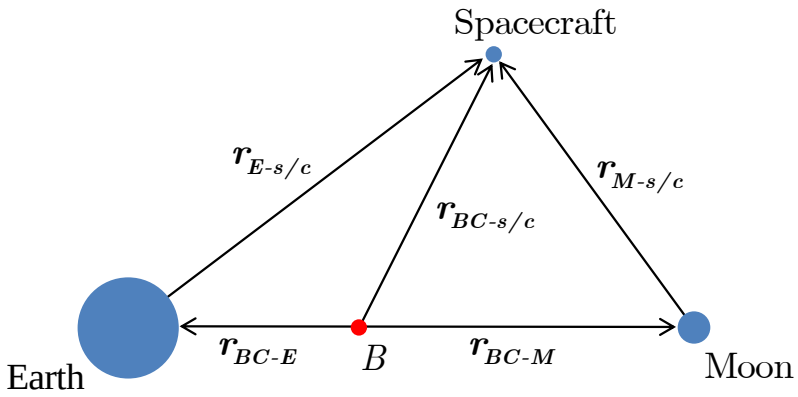

Figure 3.14. Vector Diagram: Earth-Moon System

as B. The positions of the Earth relative to the barycenter, $\boldsymbol{r_{BC-E}}$, and the Moon relative to the barycenter, $\boldsymbol{r_{BC-M}}$, are known from the problem geometry in the CR3BP. Using the figure and simple vector relationships, the geocentric spacecraft position is,

$$\boldsymbol{r_{E-s/c}} = \boldsymbol{r_{BC-s/c}} - \boldsymbol{r_{BC-E}} \tag{3.14}$$

and the position of the spacecraft with respect to the Moon by the following,

$$\boldsymbol{r_{M-s/c}} = \boldsymbol{r_{BC-s/c}} - \boldsymbol{r_{BC-M}} \tag{3.15}$$

Since multiple shooting is used to solve this problem, the Earth altitude constraint is enforced only at the first patch point, $\boldsymbol{x_i}$ for $i = 1$,

$$\boldsymbol{x_1} = \begin{bmatrix} x_1 & y_1 & z_1 & \dot{x}_1 & \dot{y}_1 & \dot{z}_1 \end{bmatrix}^T \tag{3.16}$$

The lunar altitude constraint is enforced only at the final patch point, $\boldsymbol{x_i}$ for $i = n$,

$$\boldsymbol{x_n} = \begin{bmatrix} x_n & y_n & z_n & \dot{x}_n & \dot{y}_n & \dot{z}_n \end{bmatrix}^T \tag{3.17}$$

To simplify the partial differentiation process, the altitude constraints are equivalently expressed using the square of the radial distances as in the following equations,

$$F_{alt,E}\left(\boldsymbol{x_1}\right) = r_{E-s/c}^2 - r_{E-s/c,d}^2 = 0 \tag{3.18}$$

$$F_{alt,M}\left(\boldsymbol{x_n}\right) = r_{M-s/c}^2 - r_{M-s/c,d}^2 = 0 \tag{3.19}$$

Recall that the subscript "d" denotes a desired or target quantity. Substituting known quantities into these expressions yields,

$$F_{alt,E}\left(\boldsymbol{x_1}\right) = \left(x_1 + \mu\right)^2 + y_1^2 + z_1^2 - r_{E-s/c,d}^2 = 0 \tag{3.20}$$

$$F_{alt,M}\left(\boldsymbol{x_n}\right) = \left(x_n + \mu - 1\right)^2 + y_n^2 + z_n^2 - r_{M-s/c,d}^2 = 0 \tag{3.21}$$

The corresponding blocks in the Jacobian matrix are written as

$$DF_{alt,E}\left(\boldsymbol{x_1}\right) = \frac{\partial F_{alt,E}\left(\boldsymbol{x_1}\right)}{\partial \boldsymbol{x_1}} = \begin{bmatrix} 2\left(x_1 + \mu\right) & 2y_1 & 2z_1 & 0 & 0 & 0 \end{bmatrix}, \tag{3.22}$$

$$DF_{alt,M}\left(\boldsymbol{x_n}\right) = \frac{\partial F_{alt,M}\left(\boldsymbol{x_n}\right)}{\partial \boldsymbol{x_n}} = \begin{bmatrix} 2\left(x_n + \mu - 1\right) & 2y_n & 2z_n & 0 & 0 & 0 \end{bmatrix}. \tag{3.23}$$

As illustrated in Figure 3.15, the Earth departure flight path angle, ϕ, is defined as the angle between the spacecraft velocity vector, $\boldsymbol{v_{E-s/c}}$ and the local horizon, indicated as a dashed line. Note that, given the time-invariant nature of the CR3BP, $\boldsymbol{v_{E-s/c}}$ is equal to the known velocity vector $\boldsymbol{v_{BC-s/c}}$ when they are both expressed

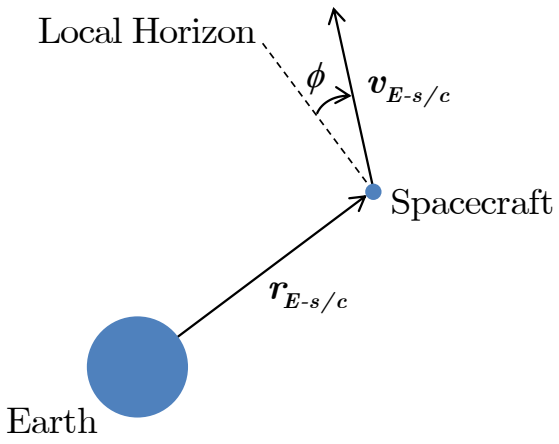

Figure 3.15. Flight Path Angle Definition

in terms of rotating coordinates. From the figure, it is clear that the flight path angle is related to the geocentric position and velocity vectors through the dot product,

$$\boldsymbol{r_{E-s/c}} \cdot \boldsymbol{v_{E-s/c}} = \cos\left(90^\circ - \phi\right) = \sin\left(\phi\right) \tag{3.24}$$

Thus, the flight path angle constraint at Earth departure, consistent with the first patch point, $\boldsymbol{x_1}$, is

$$F_{\phi,E}\left(\boldsymbol{x_1}\right) = \boldsymbol{r_{E-s/c}} \cdot \boldsymbol{v_{E-s/c}} - \sin\left(\phi_d\right) \tag{3.25}$$

where ϕ_d denotes the desired flight path angle. Substituting known quantities into equation (3.25) yields,

$$F_{\phi,E}\left(\boldsymbol{x_1}\right) = \begin{bmatrix} x_1 + \mu & y_1 & z_1 \end{bmatrix}^T \cdot \begin{bmatrix} \dot{x}_1 & \dot{y}_1 & \dot{z}_1 \end{bmatrix}^T - \sin\left(\phi_d\right) \tag{3.26}$$

The derivatives of the flight path angle constraint with respect to the free variables associated with the first patch point results in the corresponding block of the Jacobian matrix,

$$DF_{\phi,E}\left(\boldsymbol{x_1}\right) = \frac{\partial F_{\phi,E}\left(\boldsymbol{x_1}\right)}{\partial \boldsymbol{x_1}} = \begin{bmatrix} \dot{x} & \dot{y} & \dot{z} & x + \mu & y & z \end{bmatrix} \tag{3.27}$$

To complete the development of the multiple shooting algorithm, the constraints are combined with the continuity constraints imposed at internal patch points that are discussed in Section 2.4.3.

3.3.3 Strategy for Computing Planar Free Return Trajectories

In the circular restricted three-body problem, symmetric free return trajectories exist both in and out of the $\hat{x}-\hat{y}$ plane. The planar family of Earth-Moon free return trajectories is determined first using the variable-time multiple shooting algorithm. In this problem, the free variable vector, $\boldsymbol{X}$, contains the six-dimensional state vectors, $\boldsymbol{x_i}$ associated with each of the n patch points as well as the integration times, T_i, along each integrated segment, i.e.,

$$\boldsymbol{X} = \begin{bmatrix} \boldsymbol{x_1} \\ \vdots \\ \boldsymbol{x_n} \\ T_1 \\ \vdots \\ T_{n-1} \end{bmatrix} \tag{3.28}$$

In addition to imposing continuation constraints at the internal patch points, constraints are added to enforce a desired altitude at lunar arrival and desired altitude and flight path angle at Earth departure. To guarantee symmetry, constraints to enforce a perpendicular $\hat{x}-\hat{z}$ plane crossing near the Moon are added as well. Thus, the constraint vector is written,

$$\boldsymbol{F}(\boldsymbol{X}) = \begin{bmatrix} \boldsymbol{x_2^t} - \boldsymbol{x_2} \\ \vdots \\ \boldsymbol{x_n^t} - \boldsymbol{x_n} \\ r_{E-s/c}^2 - r_{E-s/c,d}^2 \\ r_{M-s/c}^2 - r_{M-s/c,d}^2 \\ \boldsymbol{r_{E-s/c}} \cdot \boldsymbol{v_{E-s/c}} - \sin(\phi_d) \\ y_n^t \\ \dot{x}_n^t \end{bmatrix} = \boldsymbol{0} \tag{3.29}$$

The Jacobian matrix, $D\boldsymbol{F}(\boldsymbol{X})$, associated with the general variable-time multiple shooting method is augmented with the additional blocks from Section 3.3.2. To

initiate the differential corrections procedure, the free return trajectory in Figure 3.13 is discretized into a series of patch points and imported as an initial guess.

For numerical reasons and, considering the sensitivities of this problem, it is often advantageous to target the free return trajectories in "backward time" beginning from the Moon rather than in "forward time" beginning from the Earth. Also, to exploit the symmetry of the trajectories, only half of each trajectory is targeted. To build up the planar free return family, single-parameter continuation is implemented to gradually increase the perilune altitude. This particular parameter is an arbitrary choice; continuation can be formulated in terms other parameters as well, such as Earth altitude, flight path angle, or time of flight.

Given the trajectory in Figure 3.13 as an initial guess, single-parameter continuation in perilune altitude is employed to generate a portion of the planar, symmetric Earth-Moon free return family. All of the orbits in the family are constrained to an Earth departure altitude of 185 kilometers and flight path angle, ϕ, of 0°. Representative orbits from this family, neglecting lunar impact trajectories, appear in Figure 3.16. The perilune altitudes for the orbits in the figure vary from 100 to 30,000 kilometers with corresponding Earth-to-Moon or Moon-to-Earth times of flight ranging from 2.86 to 4.91 days. The Earth and Moon are plotted to scale.

3.3.4 Strategy for Computing Out-of-Plane Free Return Trajectories

The out-of-plane, symmetric free return families are computed using an algorithm similar to that employed to generate the planar family. However, rather than a continuation process in terms of perilune altitude, the continuation process steps along inclination angle at perilune; perilune altitude remains constant across each family. The perilune inclination is defined as the angle between the Moon-centered spacecraft position vector at perilune and the $\hat{x}-\hat{y}$ plane. For each family member, the z-coordinate at perilune is defined based on the perilune altitude and inclination and is included with the other constraints in the variable-time multiple shooting algorithm.

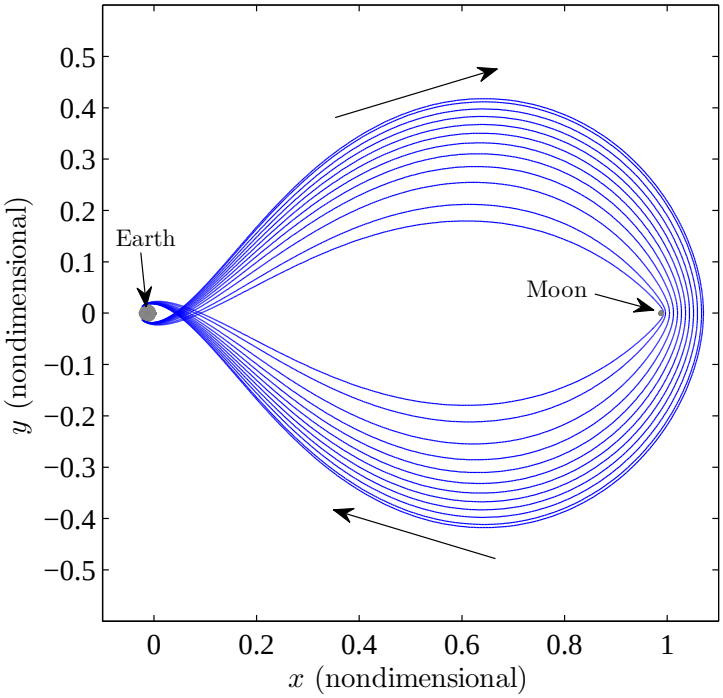

Figure 3.16. Planar Free Return Family

An orbit from the planar free return family, one that possesses the desired perilune altitude, is defined as the first member of the out-of-plane free return family. Single-parameter continuation proceeds with perilune inclination angle as the continuation parameter until a specified angle or number of orbits is reached.

A family of three-dimensional free return trajectories, with a perilune altitude of 16,000 kilometers, is generated and appears in Figure 3.17. Projections of the family onto the $\hat{x} - \hat{y}$ and $\hat{x} - \hat{z}$ planes are plotted in Figure 3.18. The perilune inclinations of the trajectories in the figures vary from $-60°$ to $60°$. The Earth-to-Moon or Moon-to-Earth flight times range from 4.35 days at $0°$ inclination to 4.67 days at perilune inclinations of $\pm 60°$.

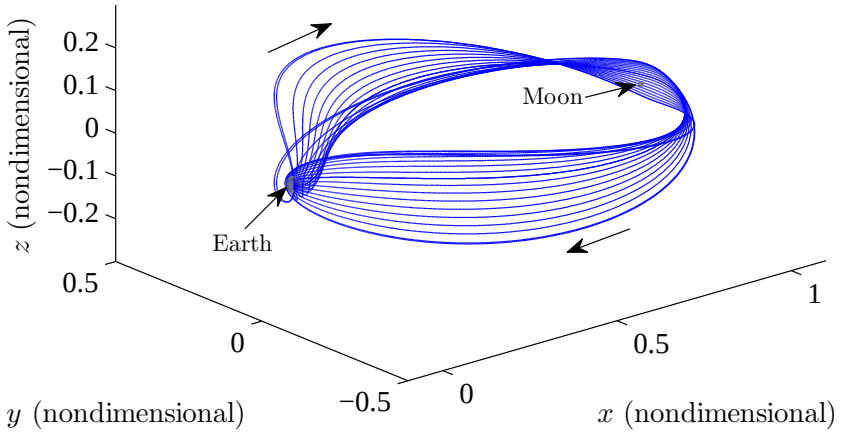

Figure 3.17. Out-of-Plane Free Return Family

3.4 Computation of Bi-Elliptic Transfers to/from Lunar Polar Orbits

In recent years, increased attention has focused on the polar regions of the Moon as potential landing sites for future manned exploration missions. The recent confirmation of the existence of water ice near the lunar south pole by NASA's Lunar Crater Observation and Sensing Satellite (LCROSS) has increased interest [3]. Inserting a manned spacecraft into lunar polar orbit, as well as departing such an orbit to return to Earth, is a nontrivial problem, however. High maneuver costs can be incurred due to the large changes in orbital inclination required. To reduce the ΔV costs and maintain reasonable times of flight, the current strategy for a manned mission to the lunar poles uses bi-elliptic transfers to and from a low altitude, polar lunar orbit [42, 43]. To assess the costs, an outbound trajectory from the Earth to a polar orbit about the Moon is computed in the CR3BP. Since an inbound trajectory is obtained if the process is reversed, the return cost is equal to the cost of arrival.

Insertion into a low lunar, polar orbit requires a capture maneuver, but a maneuver is also necessary to perform a plane change of approximately 90°. Plane change maneuvers are generally very costly so, to mitigate this problem, a bi-elliptic transfer first captures into a large ellipse about the Moon that is coplanar with the Earth-Moon

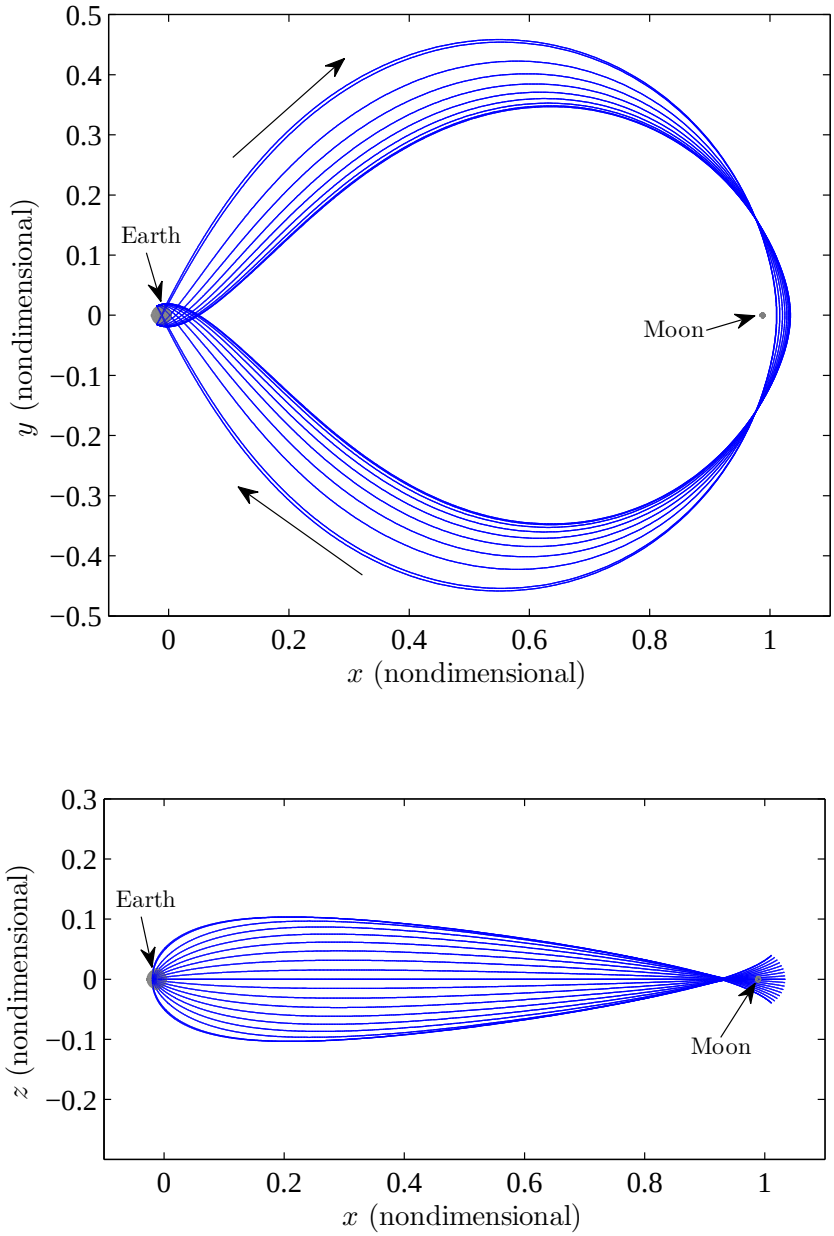

Figure 3.18. Orthogonal Views of an Out-of-Plane Free Return Family

transfer orbit. The plane change maneuver occurs at apolune in the intermediate transfer orbit to reduce the ΔV cost. Following the plane change maneuver, the spacecraft returns to the vicinity of the Moon along an intermediate transfer ellipse at 90° inclination and a maneuver at perilune circularizes the orbit. Bi-elliptic transfers are typically discussed within the context of conic two-body models, but the purpose of this section is determine an equivalent transfer in the circular restricted three-body problem.

3.4.1 Strategy for Computing Bi-Elliptic Transfer in the CR3BP

The transfer is designed to depart low Earth orbit and arrive in a polar low lunar orbit. This objective is accomplished by decomposing the transfer into four phases:

1. Outbound phase from Earth to lunar vicinity
2. In-plane, Moon-centered intermediate transfer arc from perilune to apolune
3. 90° out-of-plane, Moon-centered intermediate transfer arc from apolune to perilune
4. Circular, polar orbit

The orbital characteristics during the outbound phase are based on the size of the in-plane intermediate transfer ellipse, selected as 100 km x 15,925 km (altitude) orbit based on reference [43]. For phase 1, a planar free return trajectory with an Earth departure altitude of 185 kilometers and a perilune altitude of 100 kilometers is selected. Note that the Earth-to-lunar vicinity transfer in phase 1 appears in Figure 3.19 as it approaches the Moon.

As apparent in Figure 3.19, phase 1 shifts to phase 2 at perilune. To compute the orbit in phase 2, that is, the in-plane intermediate transfer ellipse, the final state at perilune along the free return trajectory from phase 1 is first transformed to an arbitrary inertial reference frame. From the inertial state vector, the direction of the

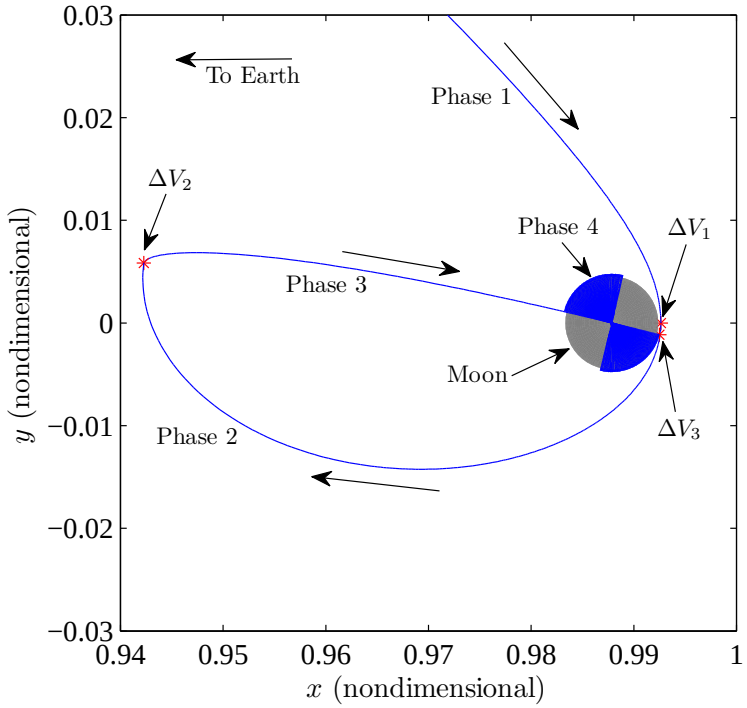

Figure 3.19. Converged Bi-Elliptic Transfer - Phases 1-4

velocity vector in inertial space is determined. The velocity at perilune along the intermediate transfer ellipse is determined from two-body analysis as,

$$v = \sqrt{2\mu_M \left(\frac{1}{r_{M-s/c}} - \frac{1}{2a_t} \right)} \tag{3.30}$$

where the spacecraft's orbital radius with respect to the Moon, $r_{M-s/c}$, and the semi-major axis of the intermediate transfer arc, a_t, are known. This conic velocity is oriented such that it is parallel to the velocity at the end free return trajectory. The initial state at perilune for the phase 2 arc is then transformed back into the CR3BP. Phase 2 terminates at apolune of the intermediate transfer ellipse. Thus, the predicted time of flight for phase 2 is chosen to be half of the two-body orbital period given by,

$$\mathbb{P} = 2\pi \sqrt{\frac{a_t^3}{\mu_M}} \tag{3.31}$$

The intermediate transfer arc, from perilune to apolune, is computed in the three-body model using a variable-time single shooting algorithm with patch points at the

beginning, $\boldsymbol{x_1}$, and end, $\boldsymbol{x_2}$, of the phase 2 trajectory arc. The patch point at the end of this integrated segment is included to simplify some of the expressions needed to enforce the constraints. The 13 free variables necessary for the shooting method are listed below. The numbers of free variables associated with each item appear in parenthesis.

1. Initial states at perilune (6)
2. End states at apolune (6)
3. Time of flight (1)

The corresponding free variable vector, $\boldsymbol{X}$, is written,

$$\boldsymbol{X} = \begin{bmatrix} \boldsymbol{x_1} \\ \boldsymbol{x_2} \\ T_1 \end{bmatrix} \tag{3.32}$$

The 13 constraints below are used to ensure that the phase 2 trajectory is the correct size, is continuous in position with the end of the phase 1 free return trajectory, and terminates at apoapsis. The numbers of constraints associated with each item also appear in parenthesis.

1. Fixed initial position (3)
2. At initial condition, $\dot{x}_1 = \dot{z}_1 = 0$ (2)
3. Continuity at end point (6)
4. Desired altitude met at final patch point (1)
5. Final patch point occurs at apoapsis ($\boldsymbol{r} \cdot \boldsymbol{v} = 0$) (1)

Thus, the constraint vector is formulated as,

$$\boldsymbol{F}(\boldsymbol{X}) = \begin{bmatrix} x_1 - x_{1,d} \\ y_1 - y_{1,d} \\ z_1 - z_{1,d} \\ \dot{x}_1 \\ \dot{z}_1 \\ \boldsymbol{x_2^t - x_2} \\ r^2_{M-s/c} - r^2_{M-s/c,d} \\ \boldsymbol{r_{M-s/c} \cdot v_{M-s/c}} \end{bmatrix} = \mathbf{0} \tag{3.33}$$

where the subscripts 1 and 2 denote the beginning and end points of the trajectory segment, respectively. The Moon-centered position and velocity vectors correspond to the end phase 2 trajectory arc. There are an equal number of constraints and free variables so the phase 2 arc is iteratively solved with a simple Newton's Method. The converged phase 2 trajectory is presented in Figure 3.19 as well.

The phase 3 trajectory arc possesses the same apolune and perilune altitudes as the phase 2 arc but is oriented approximately 90° out of the Earth-Moon orbital plane. An initial guess for the velocity at the start of the third phase is obtained by computing the two-body inertial apolune velocity from equation (3.30), orienting the velocity vector in the $+\hat{Z}$ inertial direction and transforming the inertial state back to the CR3BP. To differentially correct the out-of-plane intermediate transfer arc, a variable-time single shooting algorithm, with two patch points, is again implemented in conjunction with the same set of variables that is used to target the in-plane transfer ellipse. Constraints are added to produce an orbit of the correct size and to ensure that it terminates in a polar orbit at the $\hat{x} - \hat{y}$ plane by forcing the inertial components of velocity in the $\hat{X}$ and $\hat{Z}$ directions to zero. The 13 constraints are listed below:

1. Fixed initial position (3)

2. Continuity at end point (6)

3. Desired altitude met at final patch point (1)

4. Final patch point is in $\hat{x} - \hat{y}$ plane (1)

5. Orbit is polar with respect to Moon at final patch point (2)

The associated constraint vector is written,

$$\boldsymbol{F}(\boldsymbol{X}) = \begin{bmatrix} x_1 - x_{1,d} \\ y_1 - y_{1,d} \\ z_1 - z_{1,d} \\ \boldsymbol{x_2^t - x_2} \\ r^2_{M-s/c} - r^2_{M-s/c,d} \\ z_2 \\ \dot{X}_2 \\ \dot{Y}_2 \end{bmatrix} = \mathbf{0} \tag{3.34}$$

The phase 3 trajectory arc, plotted in Figure 3.19, is also computed using a Newton's Method. For both phases 2 and 3, the two-body analysis supplies quality initial guesses that quickly converge to trajectories in the CR3BP.

The computation of a state vector to initiate the phase 4 polar orbit originates with the two-body circular velocity,

$$v = \sqrt{\frac{\mu_M}{r}} \tag{3.35}$$

where r is the desired radius of the circular polar orbit. This velocity is applied parallel to the velocity vector at the termination of the phase 3 trajectory. The polar orbit is then numerically integrated for a specified length of time in the CR3BP. A circular polar orbit, integrated for approximately 7 days, appears in Figure 3.19, as well.

3.4.2 Numerical Example: Bi-Elliptic Transfer to a Lunar Polar Orbit

Using a series of two-body analytical approximations as initial guesses, a four-phase mission from an Earth parking orbit to a polar lunar orbit, using a bi-elliptic

orbit, is successfully computed in the circular restricted three-body problem. Additional views of the four converged trajectory arcs in Figure 3.19 appear in Figure 3.20.

The maneuvers for the three bi-elliptic transfer burns, in terms of ΔVs are determined simply by calculating the velocity discontinuities between the end point of one phase and the starting point along the next phase. The translunar injection maneuver is computed by first transforming the initial state on the free return trajectory to an inertial coordinate frame. The velocity magnitude is compared to the circular two-body velocity associated with a 185-kilometer low Earth parking orbit. The translunar injection maneuver is represented as ΔV_{TLI}. In both Figure 3.19 and 3.21, the ΔV maneuver locations are identified by red asterisks. The maneuver between Phases 1 and 2 is termed ΔV_1. The burns between Phases 2 and 3 and Phases 3 and 4 are denoted ΔV_2 and ΔV_3, respectively. The total lunar orbit insertion cost, ΔV_{LOI}, is simply equal to the sum of the three bi-elliptic transfer burns.

Table 3.1 compares the ΔV budget for the final converged trajectory in the CR3BP to the cost summary in reference [42]. Dashes indicate information that is not avail-

Table 3.1 ΔV (in km/s) Cost Comparison for Polar Lunar Mission

Maneuver	CR3BP Trajectory	CEV Trajectory [42]
ΔV_{TLI}	3.1618	3.1500
ΔV_1	0.3597	–
ΔV_2	0.3252	–
ΔV_3	0.5643	–
ΔV_{LOI}	1.2492	1.2500
$\boldsymbol{\Delta V_{tot}}$	**4.4110**	**4.4000**

able. Note that the reference ΔV numbers are associated with a trajectory computed in a full ephemeris model. However, the results in the table illustrate that, knowing

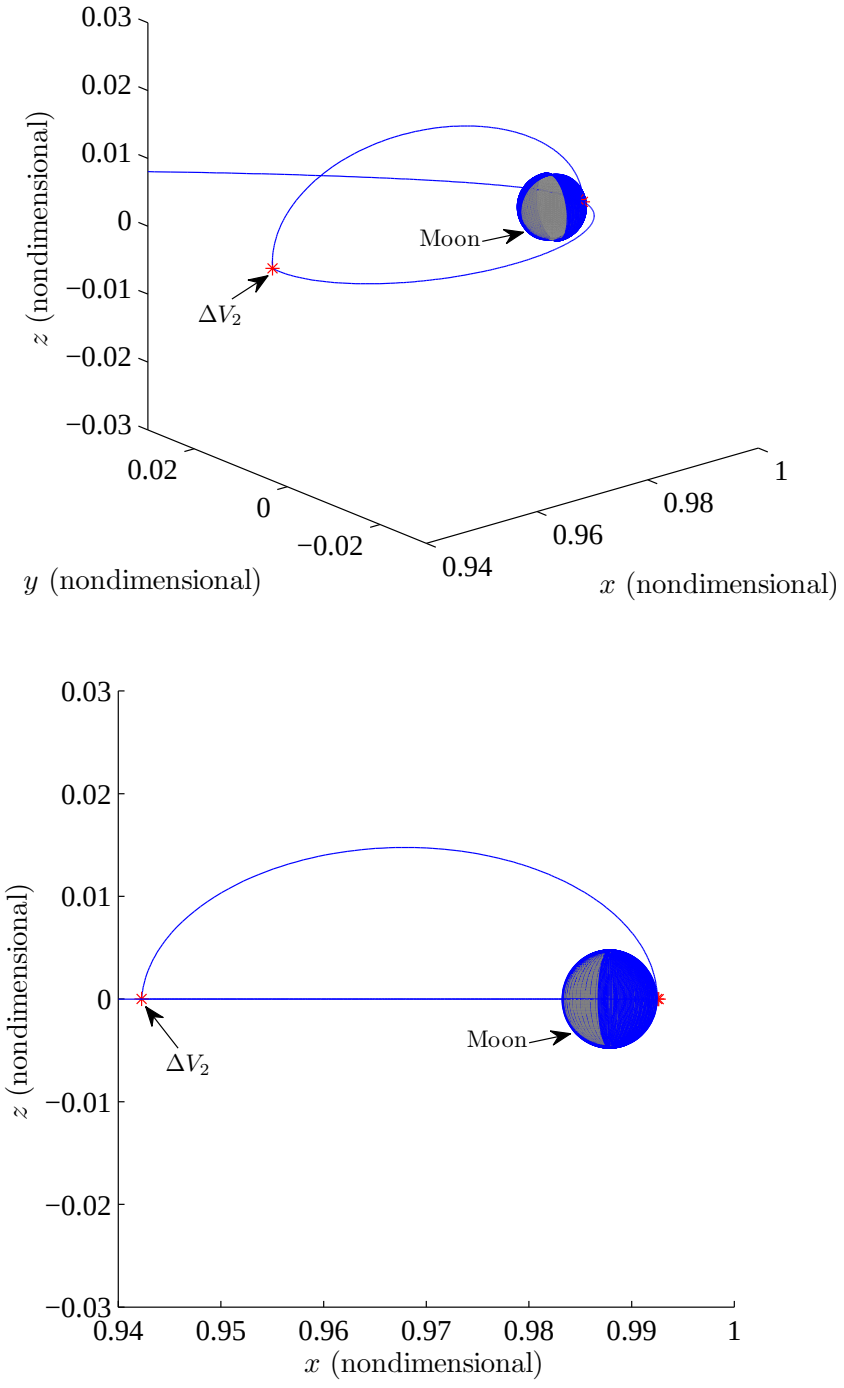

Figure 3.20. Converged Bi-Elliptic Transfer - Lunar Vicinity

only the dimensions of the intermediate transfer ellipse, the dynamical model in the circular restricted three-body problem produces a reasonable estimate of the ΔV cost associated with departure from an Earth parking orbit and delivery into a low lunar polar orbit. Isometric and projected views of the entire four-burn mission appear in Figure 3.21.

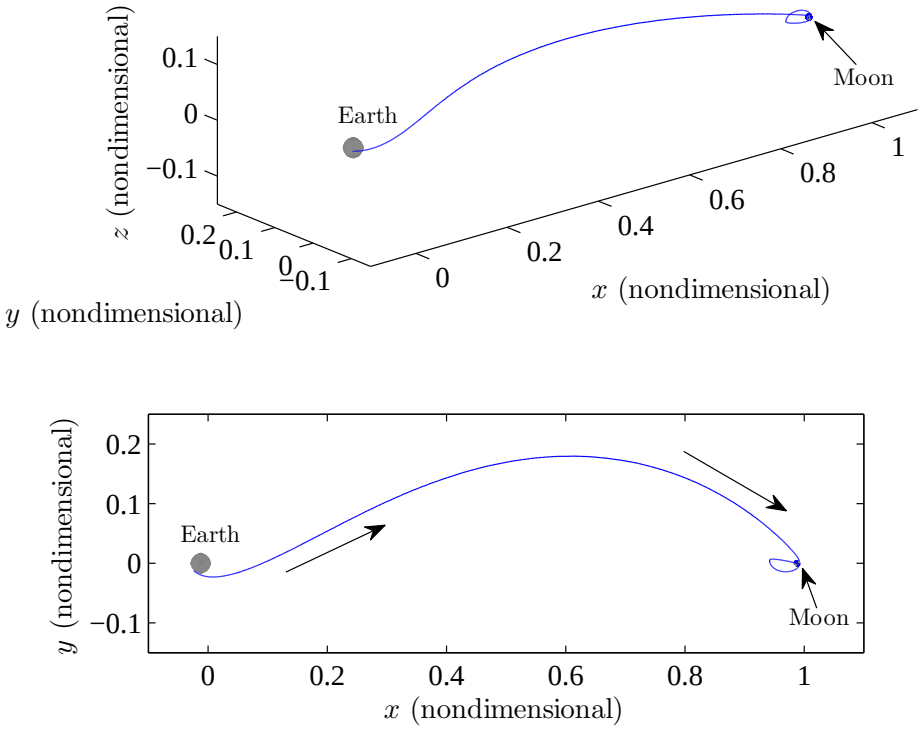

Figure 3.21. Converged Bi-Elliptic Transfer

4. TRANSITIONING TO AN EPHEMERIS MODEL

The time-invariant nature of the circular restricted three-body problem, coupled with the incorporation of multiple gravity fields simultaneously, makes it a powerful tool during the early stages of mission design in multi-body regimes. To ensure that the mission requirements are satisfied in the true dynamical environment, however, it is necessary to examine the trajectories in higher-fidelity models. A general method for transitioning orbits from the circular restricted three-body problem to an N-body model, incorporating JPL DE405 ephemerides, is discussed. Sample Lyapunov, halo, and Lissajous trajectories are transitioned from the CR3BP to an Earth-Moon-Sun ephemeris model.

4.1 Strategy to Transition from the CR3BP to an Ephemeris Model

The generalized differential corrections procedure employing constraints and free variables is applicable to trajectory design problems in any dynamical model. For greater flexibility and to reduce numerical sensitives, fixed- and variable-time multiple shooting algorithms are incorporated in the process to transition trajectories between the CR3BP and ephemeris models throughout this analysis.

To transition a solution to the ephemeris model, begin with a converged trajectory in the CR3BP. Then, the first step is to discretize the solution into a series of patch points. A patch point is comprised of the time and the six-dimensional state vector at a point along the trajectory. The number of patch points depends on the type of orbit under consideration, i.e., more sensitive solutions require a larger number of patch points. These patch points are then transformed into a primary-centered, inertial Earth J2000 coordinate frame using the transformation algorithm in Section 2.5.2 and a desired initial Julian date. Then, a new, slightly modified trajectory

is sought such that all of the constraints are satisfied in the ephemeris model. To deliver a converged solution, the N-body relative equations motion and the STM information in Sections 2.2.1 and 2.3.2.2, respectively, are implemented within a multiple shooting algorithm. Steps from Section 2.5.2 are incorporated into a general CR3BP-to-Ephemeris transition procedure and summarized as follows:

1. Compute the desired orbit in the CR3BP
2. Discretize the solution into patch points
3. Shift the CR3BP rotating states to primary-centered rotating states
4. Dimensionalize the primary-centered rotating states using the standard characteristic quantities associated with the CR3BP
5. Apply the transformation matrix in equation (2.99)
6. Nondimensionalize the inertial J2000 states using instantaneously defined characteristic quantities
7. Reconverge the solution in an N-body ephemeris model

Note that step 7 can be completed using either fixed- or variable-time multiple shooting techniques.

4.2 Quasi-Periodic Orbits in an Earth-Moon-Sun Ephemeris Model

Periodic orbits near libration points in the circular restricted three-body problem exist as quasi-periodic trajectories when transitioned to higher-fidelity models. To transition a periodic libration point orbit in the CR3BP to an ephemeris model, the orbit is first discretized into a series of patch points that are then "stacked" to construct an orbit with a desired number of revolutions. Then, the CR3BP-to-Ephemeris procedure is implemented to shift either a periodic or quasi-periodic

solution in the CR3BP to the desired ephemeris model using a fixed-time multiple shooting algorithm.

In the following examples, constraints are added only to enforce continuity at the intermediate patch points, but it is straightforward to include additional constraints. In each example, the orbits from the CR3BP are transitioned to an Earth-Moon-Sun ephemeris model and are integrated in a Moon-centered inertial frame. For comparison purposes, all orbits are plotted in a Moon-centered rotating frame, however. Note that, for each orbit type, the general characteristics of the orbit in the CR3BP are well-preserved in the ephemeris model.

4.2.1 Numerical Examples: Quasi-Lyapunov Ephemeris Trajectories

From the families of Lyapunov orbits generated in the CR3BP in Section 3.1.3, L_1 and L_2 orbits of approximately the same y-amplitude, 0.16 nondimensional units (62,000 km), are plotted in Figure 4.1 (top). These orbits are discretized into five patch points per revolution which are subsequently stacked to generate 10 revolutions. Using the procedure from Section 4.2, two Lyapunov orbits from the CR3BP are transitioned to an Earth-Moon-Sun ephemeris model. These quasi-Lyapunov orbits also appear in Figure 4.1 (bottom).

4.2.2 Numerical Examples: Quasi-Halo Ephemeris Trajectories

Quasi-halo trajectories are also generated in an ephemeris model using the procedure summarized in Section 4.2. Halo orbits in the vicinity of L_1 and L_2 with approximately equal out-of-plane z-amplitudes, that is, of 0.04 nondimensional units (15,000 km), are selected from the families of halo orbits in the CR3BP presented in Section 3.1.5. These orbits appear in red in Figures 4.2 and 4.3 (top). Both orbits are discretized into four patch points which, like the Lyapunov orbits, are stacked for 10 revolutions. Using the CR3BP-to-Ephemeris transition procedure, the solutions are reconverged in an Earth-Moon-Sun ephemeris model. Isometric and orthogonal

views of the ephemeris L_1 and L_2 quasi-halo orbits appear in blue in Figures 4.2 and 4.3, respectively.

4.2.3 Numerical Example: Lissajous Ephemeris Trajectory

As a final example, the L_2 Lissajous orbit generated in the CR3BP in Section 3.2.2 is transitioned to an ephemeris model as well. Figure 4.4 includes the CR3BP orbit in red (top) and the corresponding ephemeris trajectory in blue (bottom). Note that, since the orbit is quasi-periodic in the CR3BP, the converged Lissajous orbit in the ephemeris model resembles its analogue from the restricted problem very closely. The trajectory characteristics designed within the context of the circular restricted three-body problem are well preserved in the transition to the ephemeris model.

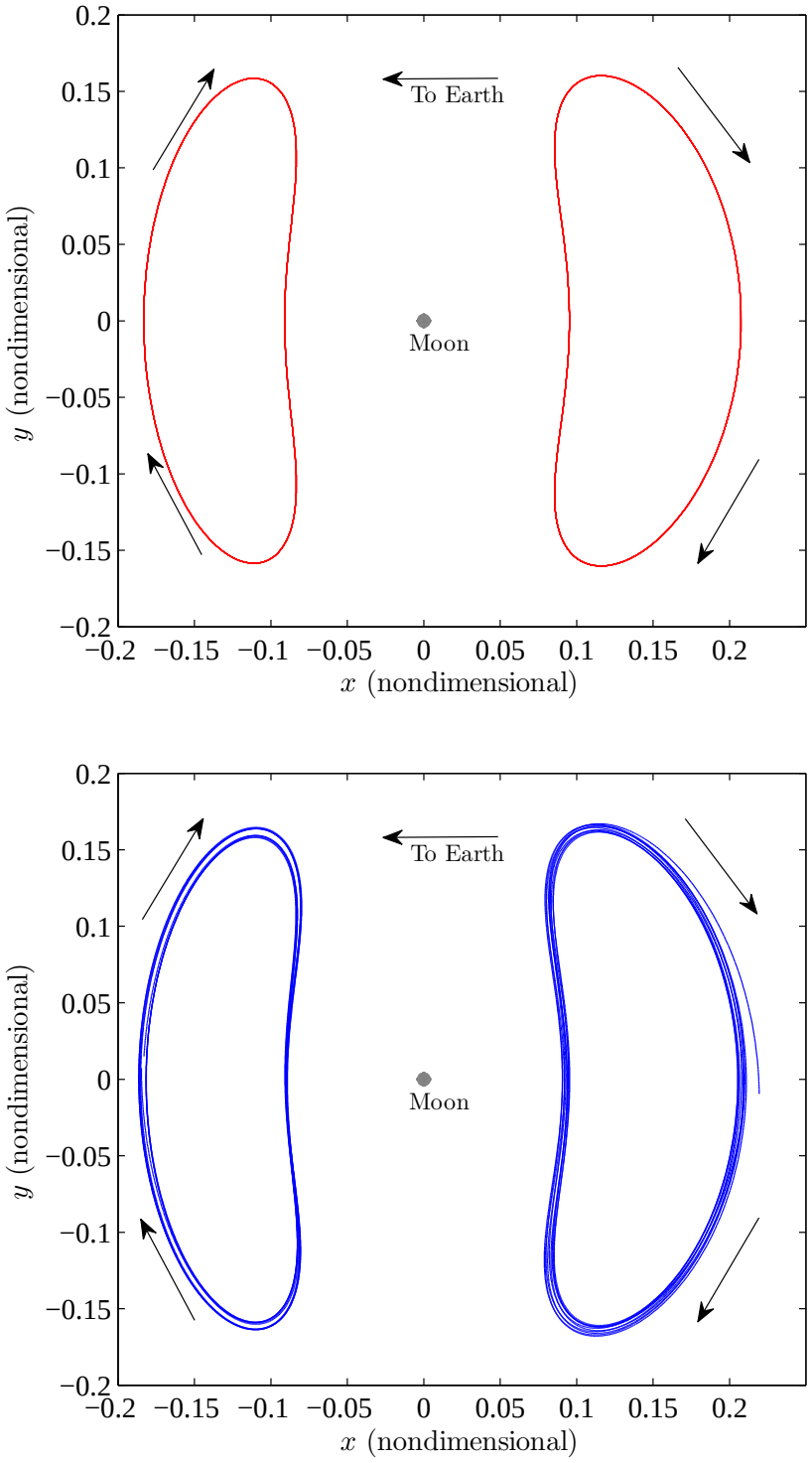

Figure 4.1. L_1 and L_2 CR3BP and Ephemeris Lyapunov Orbits

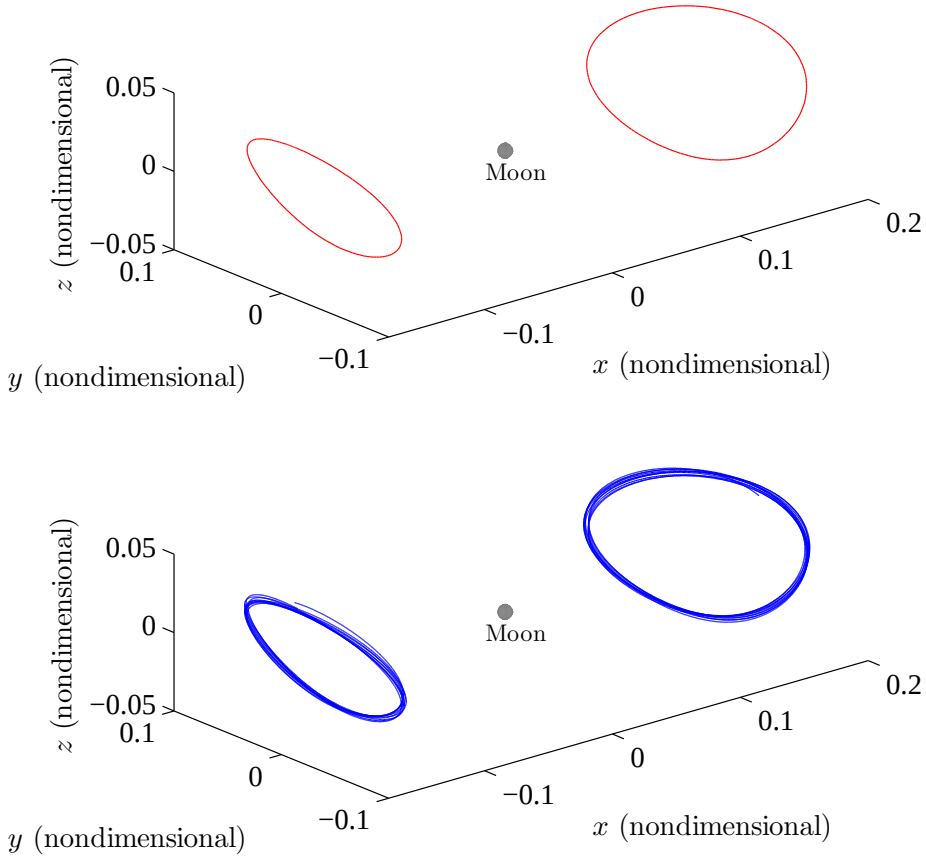

Figure 4.2. L_1 and L_2 CR3BP and Ephemeris Halo Orbits

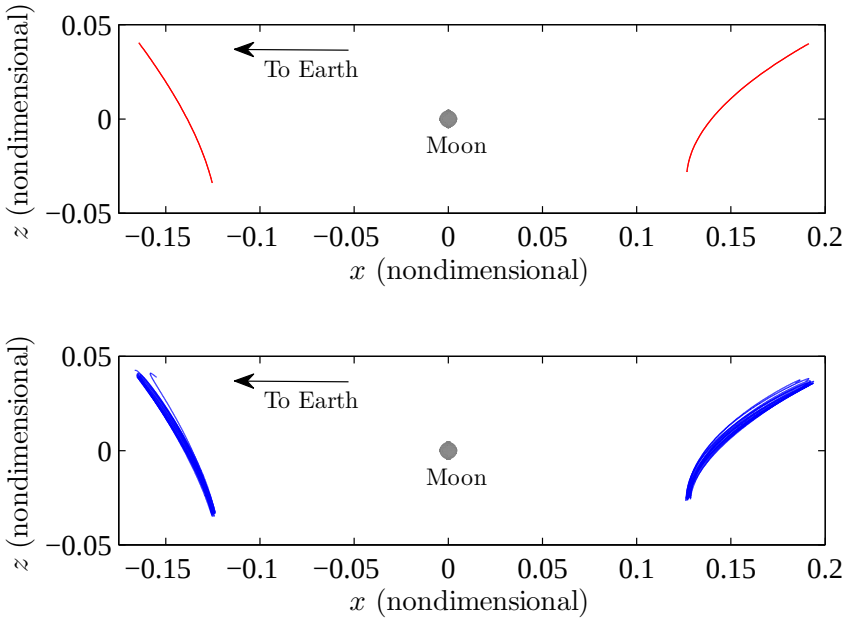

Figure 4.3. Orthogonal Views of L_1 and L_2 CR3BP and Ephemeris Halo Orbits

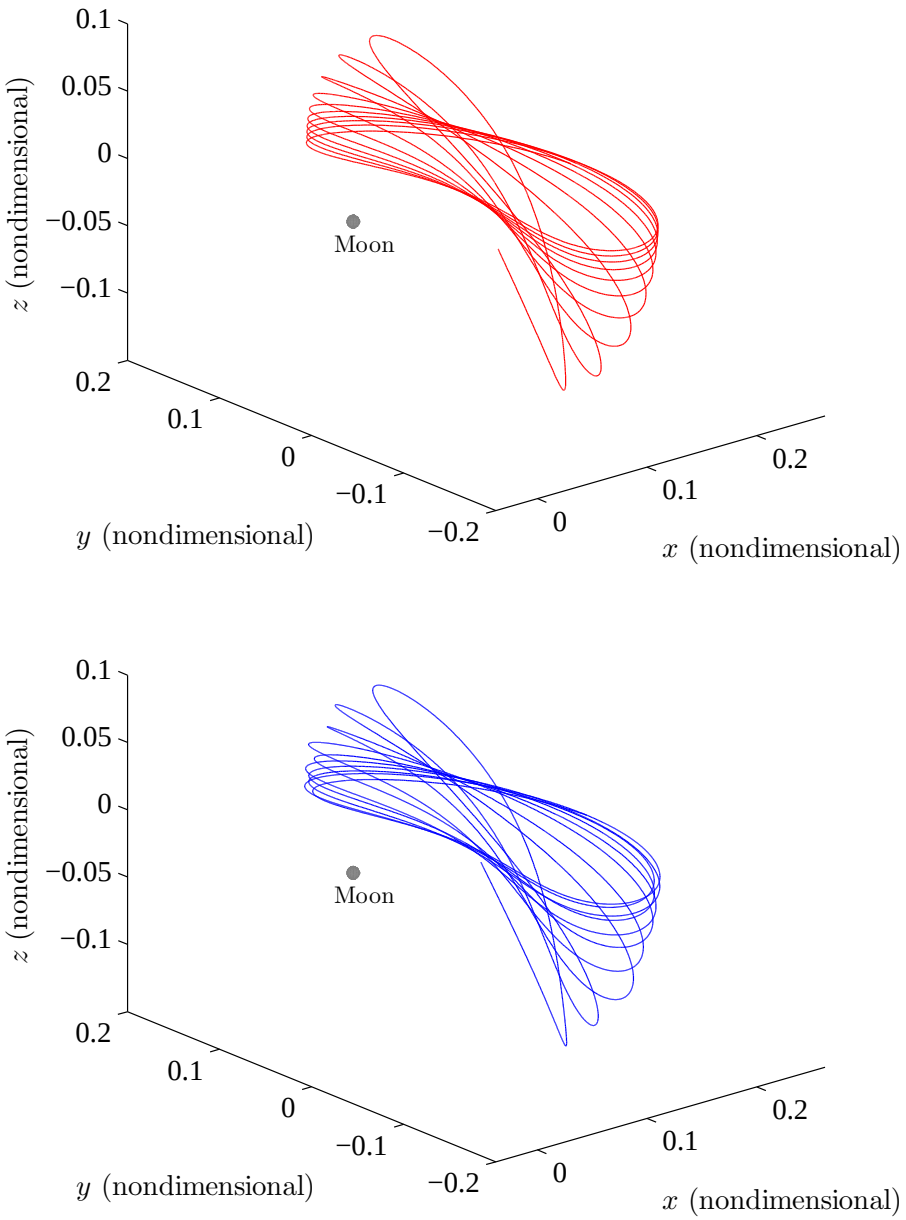

Figure 4.4. L_2 CR3BP and Ephemeris Lissajous Orbit

5. MISSION APPLICATION: LIBRATION POINT ORBIT STATIONKEEPING PROBLEM

Most useful orbits near the collinear libration points, including quasi-periodic Lissajous trajectories, are inherently unstable and must be controlled. A variety of stationkeeping strategies have previously been investigated for Sun-Earth system applications, but fewer studies have considered trajectories near the Earth-Moon libration points. Orbit maintenance is more challenging in the Earth-Moon system than in the Sun-Earth system, in part because of the shorter time scales, the larger orbital eccentricity of the secondary, and the fact that the Sun acts as a significant perturbing body both in terms of the gravitational force as well as solar radiation pressure. To accurately assess the impact of these significant differences, the analysis is modeled as a true four-body problem.

Besides the inherent issues associated with the Earth-Moon system, there are also unique stationkeeping considerations for the ARTEMIS mission, in particular. Although a baseline trajectory is defined to design the mission, there is no true reference motion that is required. Since the two spacecraft were originally designed for a different mission and are already flying, fuel is now extremely limited. Thus, with the unique operational constraints, accomplishment of the maintenance goals with the minimum cost in terms of fuel is the highest priority. Presently, stationkeeping costs of less than 60 m/s per year are desired. The cost associated with each strategy presented in this section is less than this desired value. Ultimately, a robust, automated stationkeeping strategy that does not rely on a baseline solution is sought for ARTEMIS and other libration point missions in the Earth-Moon system. As a precursor to this goal, this analysis applies a baseline orbit control-point targeting

strategy relying on the current ARTEMIS baseline solution as a means of assessing general sensitivities and maneuver costs at various points along the trajectory.

In this analysis, average costs for several formulations of a control-point targeting stationkeeping strategy are computed for the L_2 Lissajous orbit of the ARTEMIS P_1 spacecraft using Monte Carlo simulations. For purposes of comparison, similar studies are presented for the L_2 Lyapunov and halo orbits computed in Chapter 4, as well. All orbits in this chapter are computed in an Earth-Moon-Sun model incorporating the JPL DE405 ephemerides.

5.1 Baseline Orbit Control-Point Targeting Strategy

The orbit control-point targeting strategy is a straightforward approach in which the spacecraft is maintained near a predefined baseline orbit and has been implemented under different names by Grebow et al. [23] and others. Impulsive maneuvers are implemented at regular intervals to target future points along a nominal reference trajectory. In practice, the targeting is accomplished by first selecting a set of control points along a baseline orbit *a priori*.

To begin each simulation, simulated navigation and modeling errors, $\delta \boldsymbol{r_i}$ and $\delta \boldsymbol{v_i}$, are applied randomly in position and velocity, respectively. The trajectory is integrated forward in time and then, as the spacecraft passes close to each control point, a single shooting Newton Method is used to compute an impulsive ΔV maneuver such that the spacecraft reaches the next control point along the nominal trajectory (assuming no errors). After each maneuver has been calculated, simulated navigation and modeling errors are again added along with burn errors, $\delta \Delta \boldsymbol{v_i}$, and the trajectory is propagated forward. This procedure is repeated for the desired number of control points and is illustrated in Figure 5.1 which is adapted from reference [23]. The blue path denotes the baseline trajectory and the green segments represent the paths targeted from each maneuver location. The inclusion of error, however, implies that the spacecraft does not actually reach each control point and, instead, follows

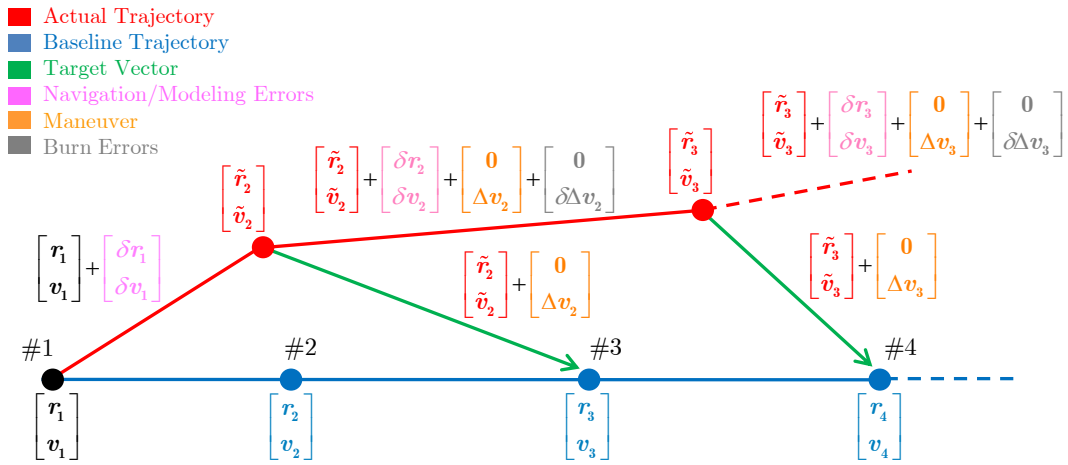

Figure 5.1. Control-Point Stationkeeping Algorithm

the red path. For this analysis, navigation and modeling errors are simulated by introducing random errors in position and velocity with variances of 1 km and 1 cm/s, respectively, after each maneuver is calculated. Burn errors of ±2% are added to each ΔV maneuver, as well. For each case, 300 Monte Carlo simulations are sufficient to determine the average stationkeeping cost. The entire control-point stationkeeping procedure is summarized in the list below.

1. Apply navigation/modeling errors to initial conditions; integrate forward to the vicinity of next control point
2. Calculate ΔV to reach next control point using single shooting
3. Apply navigation/modeling and burn errors; integrate forward to the vicinity of next control point
4. Repeat steps 2 and 3 for desired number of patch points
5. Repeat steps 1–4 for desired number of Monte Carlo simulations

To assess the general costs associated with stationkeeping maneuvers that are implemented in various regions along any libration point orbit, three control-point place-

ment schemes are investigated. (i) In the first scheme, control points are placed at x-axis crossings along the baseline orbit. (ii) A second strategy implements all maneuvers at locations that correspond to maximum y-amplitude. (iii) The final placement concept employs four maneuvers per revolution, placed specifically at all x-axis crossings and locations of maximum y-amplitude.

Sensitivities to errors in Lissajous ephemeris orbits in the Earth-Moon system are quite high. Selection of the "best" stationkeeping strategy is nontrivial. Strategies that do not incorporate a baseline can suffer from a requirement for manual intervention to maintain the vehicle; automated Monte Carlo analyses may not be possible. Control-point methods are very successful in an automated process but require a baseline. Perhaps a hybrid process that can blend an evolving baseline solution with a control-point maneuver design scheme can be investigated.

5.2 Numerical Results: Stationkeeping Cost Comparison

The cost associated with maintaining the L_2 Lissajous orbit for the ARTEMIS P_1 spacecraft (which is similar to the L_2 Lissajous computed in Chapter 4) and the ephemeris L_2 Lyapunov and halo orbits presented in the previous chapter is computed for each control-point placement scheme. The ARTEMIS L_2 trajectory evolves from a highly inclined orbit with a maximum z-amplitude of approximately 0.08 nondimensional units (30,000 km) to one that is nearly planar with a maximum y-amplitude of about 0.16 nondimensional units (62,000 km). Therefore, a Lyapunov orbit is selected such that $A_y \approx 0.16$ and the halo is chosen such that $A_z \approx 0.04$ (since the z-amplitude of the ARTEMIS trajectory ranges from 0 to 0.08 nondimensional units). The control-point stationkeeping algorithm is successfully employed to maintain a spacecraft on each orbit for approximately the same time interval. The ARTEMIS trajectory is maintained for approximately 129 days. The Lyapunov and halo orbits possess similar mission durations of 133 and 139 days, respectively.

5.2.1 Stationkeeping Cost Comparison for ARTEMIS L_2 Lissajous Orbit

The L_2 Lissajous orbit for the ARTEMIS P_1 spacecraft, plotted in Figure 5.2, is successfully maintained for 129 days using each of the three control-point placement strategies. For this study, a Monte Carlo analysis with 300 trials is sufficient to

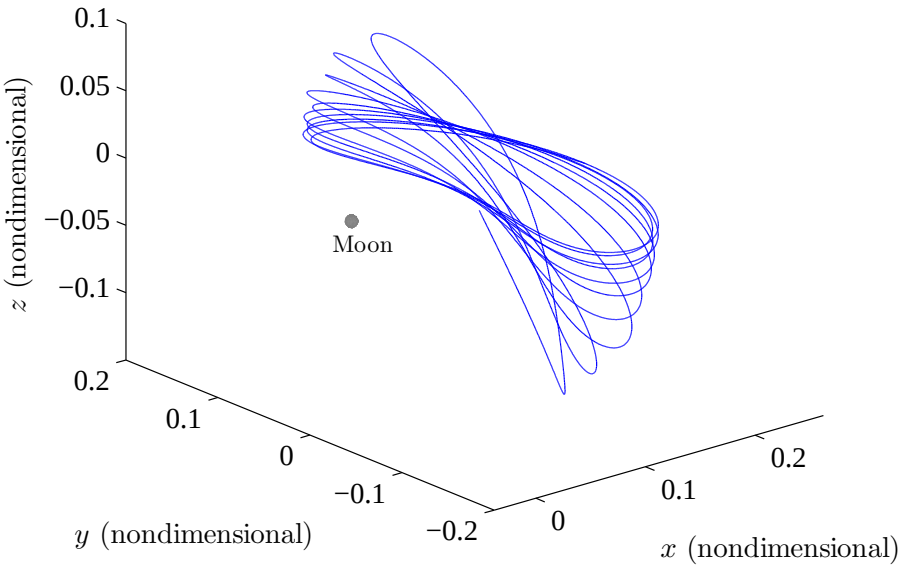

Figure 5.2. L_2 Lissajous Orbit–ARTEMIS P_1 Spacecraft

determine the average stationkeeping cost since performing additional trials does not significantly affect the average. For purposes of illustration, the results from a representative Monte Carlo simulation are presented in Figure 5.3. This case simulates the maintenance of the ARTEMIS L_2 Lissajous orbit using control points along the x-axis only. The blue circles identify the results from each individual trial and the red asterisks denote the moving average computed at that point in the simulation. Note that, after 300 trials, there is minimal change in the moving average.

The results for all three control-point placement schemes appear in Table 5.1. For each case, the number of maneuvers, the average total ΔV for the mission, the corresponding standard deviation, the average ΔV per year, and the average time between maneuvers are computed. For the ARTEMIS L_2 Lissajous orbit, if maneu-

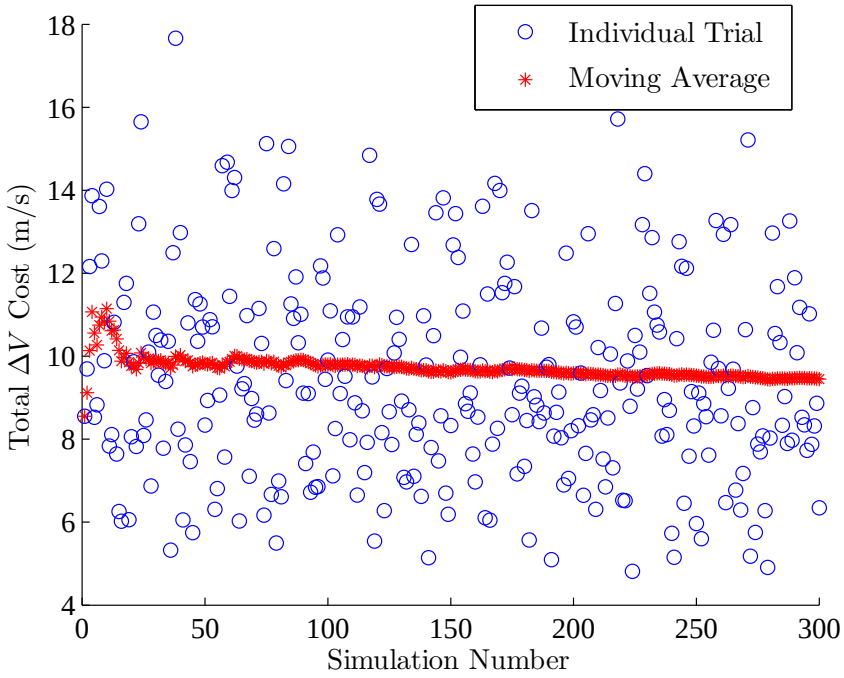

Figure 5.3. Example Monte Carlo Simulation (300 Trials)

vers are implemented approximately once a week, an average total ΔV of 9.45 m/s is required to maintain the orbit if maneuvers occur at the x-axis crossings. It is considerably more expensive from a fuel standpoint to burn at locations of maximum y-amplitude. The standard deviation is much higher for the maximum y-amplitude case, as well, which implies that the stationkeeping cost is highly variable and depends heavily on the errors that are incurred relative to the baseline trajectory. In terms of the ΔV cost, the best option is a scheme based on four maneuvers per orbit (every 3.82 days). This result is intuitive since the error along the trajectory has less chance to accumulate and, therefore, should be less costly to mitigate. However, the ability to successfully implement the maneuvers so close together is heavily contingent upon obtaining adequate orbit determination solutions in only three days.

Table 5.1 Stationkeeping Cost Comparison: L_2 Lissajous Orbit (300 Trials)

	x-axis Crossings	Max. y-Amplitudes	4 Maneuvers per Rev.
No. of Maneuvers	16	17	33
Avg. Tot. ΔV (m/s)	9.45	14.54	2.50
Std. Dev. (m/s)	2.45	7.26	0.32
Avg. ΔV per Year (m/s)	26.59	40.92	7.04
Avg. Time Between Maneuvers (Days)	7.63	7.21	3.82

5.2.2 Stationkeeping Cost Comparison for L_2 Lyapunov Orbit

The same three stationkeeping algorithms are also applied to the planar L_2 Lyapunov orbit in Figure 5.4. A summary of the stationkeeping costs are listed in Table 5.2. The period of the Lyapunov orbit is slightly longer than the period corresponding to the quasi-periodic Lissajous orbit, but the same trends in stationkeeping cost are observed. Implementing a burn approximately every 8 days, substantial fuel savings are realized via maneuvers along the x-axis instead of locations of maximum y-amplitude. A four-maneuver strategy is again the least expensive option with a total average ΔV cost of only 2.54 m/s. Stationkeeping costs for the Lyapunov orbit are less than for the Lissajous orbit with two maneuvers per revolution. When four burns are implemented per revolution, however, the Lyapunov orbit is slightly more expensive to maintain than the Lissajous orbit.

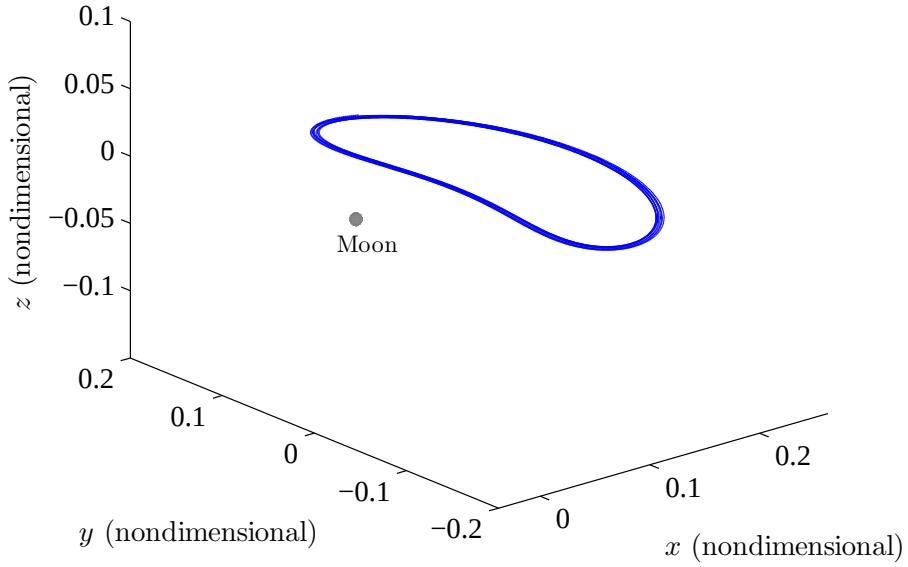

Figure 5.4. L_2 Lyapunov Orbit

Table 5.2 Stationkeeping Cost Comparison: L_2 Lyapunov Orbit (300 Trials)

	x-axis Crossings	Max. y-Amplitudes	4 Maneuvers per Rev.
No. of Maneuvers	16	17	33
Avg. Tot. ΔV (m/s)	6.26	12.72	2.54
Std. Dev. (m/s)	1.25	3.25	0.31
Avg. ΔV per Year (m/s)	16.71	33.96	6.78
Avg. Time Between Maneuvers (Days)	8.04	7.60	4.02

5.2.3 Stationkeeping Cost Comparison for L_2 Halo Orbit

Each stationkeeping strategy is employed to compute the stationkeeping costs associated with the L_2 halo orbit as well. The ephemeris halo orbit, originally computed in Section 4.2.2, appears again in Figure 5.5. The associated stationkeeping costs for

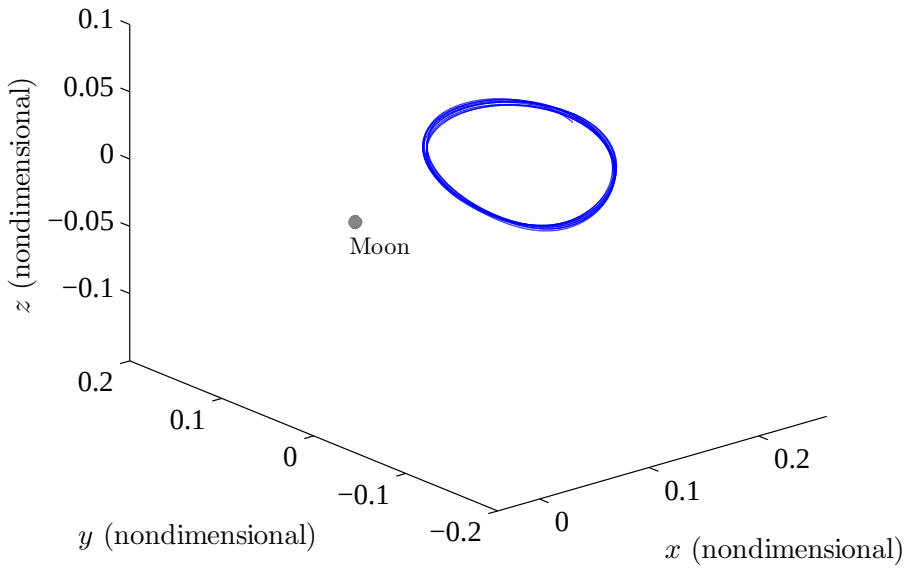

Figure 5.5. L_2 Halo Orbit

this orbit are summarized in Table 5.3. While it is least expensive to implement four maneuvers per revolution (average total $\Delta V = 2.45$ m/s), it is interesting to note that, in contrast with the results for the Lissajous and Lyapunov orbits, the total average ΔV to maintain the L_2 halo orbit is nearly the same if maneuvers occur at either the x-axis crossings or the locations of maximum y-amplitude. This result may be due to the fact that, unlike the Lissajous orbit, the locations of maximum y-amplitude do not correspond to locations of local maximum z-amplitudes in the halo orbits. However, further analysis is necessary to better understand this phenomenon.

Table 5.3 Stationkeeping Cost Comparison: L_2 Halo Orbit (300 Trials)

	x-axis Crossings	Max. y-Amplitudes	4 Maneuvers per Rev.
No. of Maneuvers	16	17	33
Avg. Tot. ΔV (m/s)	8.61	8.78	2.45
Std. Dev. (m/s)	1.90	1.98	0.30
Avg. ΔV per Year (m/s)	23.53	24.03	6.74
Avg. Time Between Maneuvers (Days)	7.85	7.41	3.92

6. MISSION APPLICATION: EARTH–MOON TRANSFER PROBLEM IN AN EPHEMERIS MODEL

In the event that future manned lunar missions lose contact with mission control due to equipment failure or on-board catastrophe, it is critical that trajectory correction maneuvers be computed onboard the spacecraft autonomously. This task was virtually impossible during the Apollo era, but tremendous increases in modern computing power now make this a realistic mission requirement. Nevertheless, despite technological advances, such onboard algorithms must remain relatively simple and offer quick and robust convergence. An eventual goal is the development of an automated process capable of computing high-fidelity ephemeris solutions using analytical expressions and/or banks of pre-calculated solutions as initial guesses [28–31].

This analysis represents a preliminary step toward such a goal. In this application, the basic variable-time multiple shooting algorithm introduced in Section 2.4.5 is adapted to numerically correct Moon-Earth return trajectories in an Earth-Moon-Sun ephemeris model incorporating DE405 ephemerides. The purpose of this algorithm is twofold. First, it is used to demonstrate that Moon-Earth transfer trajectories can be easily transitioned between the circular restricted three-body and full ephemeris models. This capability implies that, in future work, the reduced complexity of the CR3BP could be exploited to generate a wide range of solution options. The most promising trajectory options can then be reliably transitioned to the full ephemeris model. A second use of the multiple shooting algorithm is simply to explore the design space by altering the characteristics of a baseline trajectory using continuation procedures.

The variable-time multiple shooting algorithm incorporates multiple maneuvers, a constraint on total ΔV, and is used to compute Moon-Earth return trajectories

in the CR3B and ephemeris models. To incorporate the time-varying nature of the ephemeris model, a method is discussed to determine the gradient information relating changes in a final integrated state to changes in epoch time. Finally, trajectories are transitioned between the two dynamical models; single-parameter continuation in terms of total ΔV is employed to explore a variety of mission options.

6.1 Strategy for Computing Moon-Earth Transfer Trajectories

6.1.1 Differential Corrections Procedure

The variable-time multiple shooting algorithm is designed to compute a trajectory that, using a series of impulsive maneuvers, departs a lunar polar orbit and satisfies a specific set of entry requirements at Earth arrival. As discussed in Section 3.4, a currently popular design concept for this mission is based on a bi-elliptic transfer from two-body analysis. Initial guess generation is nontrivial in this problem so, for purposes of this study, a converged baseline ephemeris trajectory based on an optimized solution obtained via a grid search is used as an initial guess for the differential corrections algorithm [29, 31]. This trajectory is discretized into a series of patch points to distribute the high numerical sensitivities associated with targeting close to two primaries and to allow for path constraints at various locations along the trajectory.

As in previous chapters, the algorithm is developed by first constructing the free variable vector, $\boldsymbol{X}$. In this formulation, the states, $\boldsymbol{x_i}$, at each patch point and the epochs, t_i, associated with the internal patch points are allowed to vary. The integration times between patch points, T_i, and a slack variable, β, associated with the inequality constraint on total ΔV are also included as free variables. Allowing

the integration time to vary allows the physical length of the segments to vary as well. The free variable vector of length $8n-3$ is summarized,

$$\boldsymbol{X} = \begin{bmatrix} \boldsymbol{x_1} \\ \vdots \\ \boldsymbol{x_n} \\ T_1 \\ \vdots \\ T_{n-1} \\ t_2 \\ \vdots \\ t_{n-1} \\ \beta \end{bmatrix} \tag{6.1}$$

where n is the number of patch points. While the algorithm is sufficiently general to accommodate any number of patch points, only 11 patch points are used to compute all of the trajectories in this analysis. The full trajectory is generated by propagating forward in time from one patch point to the next with one exception: the final segment along the trajectory is integrated backwards in time from the final patch point to mitigate problems resulting from high numerical sensitivities associated with the Earth arrival state.

As mentioned previously, one advantage of multiple shooting algorithms is that constraints are easily implemented at any patch point along the path. For this application, ΔV maneuvers are inserted or removed at any patch point and the *total* ΔV cost is constrained. At patch points where ΔV maneuvers are allowed, the constraint vector, $\boldsymbol{F}(\boldsymbol{X})$, is used to enforce continuity in position only between the final state along the previous integrated segment and the patch point, i.e., the initial point along the next segment. Continuity in both position and velocity is required at patch points where ΔV maneuvers are not implemented. Continuity in time is also enforced at each patch point via the constraint,

$$t_i + T_i - t_{i+1} = 0 \tag{6.2}$$

Additional constraints are added to fix the initial state near the Moon and to enforce a desired altitude and flight path angle at Earth arrival. Ultimately, it is also necessary to consider longitude, latitude, and flight path azimuth as well, but these constraints are not included in the present analysis. The final constraint requires that the total ΔV be below a desired value. The ΔV inequality constraint,

$$\Delta V_{tot} \leq \Delta V_{allowed} \tag{6.3}$$

is rewritten as the equality constraint,

$$\Delta V_{tot} - \Delta V_{allowed} + \beta^2 = 0 \tag{6.4}$$

where ΔV_{tot}, is the sum of the magnitudes of all permitted maneuvers and β is a slack variable. The Jacobian matrix, $D\boldsymbol{F}(\boldsymbol{X})$, is again formulated by evaluating the derivatives of the constraints with respect to the free variables. Consistent with previous applications, the Jacobian matrix is sparse. In the current formulation of the problem, there are more variables than constraints so a minimum norm solution is used to compute the update. Iterations proceed until the norm of the constraint vector is below a desired tolerance. Note that some elements of this matrix include the derivative of a final integrated state with respect to the segment's epoch, i.e., $\frac{\partial \boldsymbol{x_i^t}}{\partial t_{i-1}}$. Determining such derivatives is nontrivial and is discussed in detail in the following section.

6.1.2 Obtaining General Final State Derivative Information

To compute the derivative of a final integrated state with respect to an epoch time, an arbitrary example is first discussed [44]. Generalizing equation (2.37) in Section 2.3.1, the second-order differential equations in either the CR3BP or ephemeris models can be rewritten as a series of first-order differential equations in the form,

$$\dot{\boldsymbol{x}} = \boldsymbol{f}(t, \boldsymbol{x}, \boldsymbol{\lambda}) \tag{6.5}$$

where $\boldsymbol{x}$ is the state vector and $\boldsymbol{\lambda}$ represents a vector of additional parameters that depend on the system model; any parameter in $\boldsymbol{\lambda}$ can be incorporated as a free

variable in a differential corrections process as well. Note that $\boldsymbol{\lambda}$ can include one or multiple parameters. Consider first the general problem of obtaining the derivative information relating a final state, written $\boldsymbol{x}$ for concision, to the parameter(s), $\boldsymbol{\lambda}$, $\frac{d\boldsymbol{x}}{d\boldsymbol{\lambda}}$. A first-order differential equation governing $\frac{d\boldsymbol{x}}{d\boldsymbol{\lambda}}$ can be written,

$$\frac{d}{dt}\left(\frac{d\boldsymbol{x}}{d\boldsymbol{\lambda}}\right) = \frac{d}{d\boldsymbol{\lambda}}\left(\frac{d\boldsymbol{x}}{dt}\right) \tag{6.6}$$

since $\boldsymbol{\lambda}$ and t are independent. Rewriting the time derivative of $\boldsymbol{x}$, substituting equation (6.5), and employing the chain rule yields

$$\frac{d}{dt}\left(\frac{d\boldsymbol{x}}{d\boldsymbol{\lambda}}\right) = \frac{d}{d\boldsymbol{\lambda}}\dot{\boldsymbol{x}} \tag{6.7}$$

$$= \frac{d}{d\boldsymbol{\lambda}}\boldsymbol{f}\left(t, \boldsymbol{x}, \boldsymbol{\lambda}\right) \tag{6.8}$$

$$= \frac{\partial \boldsymbol{f}}{\partial \boldsymbol{x}}\frac{d\boldsymbol{x}}{d\boldsymbol{\lambda}} + \frac{\partial \boldsymbol{f}}{\partial \boldsymbol{\lambda}} \tag{6.9}$$

The term $\frac{\partial \boldsymbol{f}}{\partial \boldsymbol{x}}$ in equation (6.9) relates changes in the vector field, $\boldsymbol{f}\left(\boldsymbol{x}, \boldsymbol{\lambda}\right)$, to changes in the states, $\boldsymbol{x}$, and is defined as the matrix, $A\left(t\right)$. Assuming a state vector is of length 6 and a parameter vector, $\boldsymbol{\lambda}$, of length ν, then the appropriate $6 \times \nu$ equations are represented as,

$$\frac{d}{dt}\left(\frac{d\boldsymbol{x}}{d\boldsymbol{\lambda}}\right) = A\left(t\right)\frac{d\boldsymbol{x}}{d\boldsymbol{\lambda}} + \frac{\partial \boldsymbol{f}}{\partial \boldsymbol{\lambda}} \tag{6.10}$$

Equation (6.10) governs the sensitivity matrix, $\frac{d\boldsymbol{x}}{d\boldsymbol{\lambda}}$, and are subject to the initial conditions,

$$\frac{d\boldsymbol{x}}{d\boldsymbol{\lambda}}\left(0\right) = \mathbf{0}_{\mathbf{6}\times\boldsymbol{\nu}} \tag{6.11}$$

since changes in the parameters cannot cause change in the states in zero integration time. By integrating equation (6.10) and the equations of motion simultaneously, $\frac{d\boldsymbol{x}}{d\boldsymbol{\lambda}}$ is determined at any point along the integrated path.

6.1.3 Obtaining Final State Derivatives with Respect to Epoch Time

The general procedure to develop derivatives relative to an arbitrary parameter is applied to the differential corrections process in the ephemeris model to obtain

the derivative of a final integrated state with respect to epoch time, i.e., $\frac{\partial \boldsymbol{x}}{\partial t_0}$. For purposes of this derivation, t_0 represents an arbitrary epoch time. This derivative is trivial in the CR3BP and is always equal to zero given the time-invariant formulation. Applying the more general approach, the vector field for the N-body ephemeris model is written,

$$\dot{\boldsymbol{x}} = \boldsymbol{f}\left(t, \boldsymbol{x}, \sum_{i=2}^{n-1} \boldsymbol{R_{1i}}\left(t_0\right)\right) \tag{6.12}$$

where $\boldsymbol{R_{1i}}$ is defined as the position vector of a perturbing body relative to the central body, denoted as body 1. This vector information is available directly from planetary ephemeris data and is dependent on the epoch time, t_0. A first-order differential equation governing $\frac{d\boldsymbol{x}}{dt_0}$ can be written,

$$\frac{d}{dt}\left(\frac{d\boldsymbol{x}}{dt_0}\right) = \frac{d}{dt_0}\left(\frac{d\boldsymbol{x}}{dt}\right) \tag{6.13}$$

since t_0 and t are independent. Rewriting the time derivative of $\boldsymbol{x}$, substituting equation (6.12), and employing the chain rule yields the following three equations, respectively,

$$\frac{d}{dt}\left(\frac{d\boldsymbol{x}}{dt_0}\right) = \frac{d}{dt_0}\dot{\boldsymbol{x}} \tag{6.14}$$

$$= \frac{d}{dt_0}\boldsymbol{f}\left(t, \boldsymbol{x}, \sum_{i=2}^{n-1} \boldsymbol{R_{1i}}\left(t_0\right)\right) \tag{6.15}$$

$$= \frac{\partial \boldsymbol{f}}{\partial \boldsymbol{x}}\frac{d\boldsymbol{x}}{dt_0} + \sum_{i=2}^{n-1} \frac{\partial \boldsymbol{f}}{\partial \boldsymbol{R_{1i}}}\frac{\partial \boldsymbol{R_{1i}}}{\partial t_0} \tag{6.16}$$

In equation (6.16), the term $\frac{\partial \boldsymbol{R_{1i}}}{\partial t_0}$ is rewritten,

$$\frac{\partial \boldsymbol{R_{1i}}}{\partial t_0} = \frac{\partial \boldsymbol{R_{1i}}}{\partial t} = \boldsymbol{V_{1i}} \tag{6.17}$$

where $\boldsymbol{V_{1i}}$ is simply the velocity of perturbing body i relative to the central body and is obtainable from planetary ephemeris data. The term $\frac{\partial \boldsymbol{f}}{\partial \boldsymbol{R_{1i}}}$ is determined directly from the equations of motion via analytical or finite differencing methods. Substituting the definition of the matrix, $A\left(t\right)$, and the result from equation (6.17) into equation (6.16), yields the differential equation,

$$\frac{d}{dt}\left(\frac{d\boldsymbol{x}}{dt_0}\right) = A\left(t\right)\frac{d\boldsymbol{x}}{dt_0} + \sum_{i=2}^{n-1} \frac{\partial \boldsymbol{f}}{\partial \boldsymbol{R_{1i}}}\boldsymbol{V_{1i}} \tag{6.18}$$

In this formulation, $\frac{d}{dt}\left(\frac{d\boldsymbol{x}}{dt_0}\right)$ is a 1×6 vector that is subject to the initial condition,

$$\frac{d\boldsymbol{x}}{dt_0}(0) = \mathbf{0_{1\times 6}} \tag{6.19}$$

Integrating equation (6.18), simultaneously with the equations of motion, allows the partial, $\frac{d\boldsymbol{x}}{dt_0}$, to be determined at any point along the integrated trajectory.

6.2 Numerical Example: Earthbound Return Leg for a Mission to the Lunar Poles

The variable-time multiple shooting algorithm described in Section 6.1.1 is sufficiently general to complete differential corrections procedure in either the circular restricted three-body problem or a full ephemeris model by modifying only the equations of motion and the formulation of the two Earth arrival constraints. This approach is employed within a continuation process based on known solutions to significantly reduce total ΔV cost. Additionally, different types of solutions are generated by removing the deterministic plane change maneuver entirely. Most importantly, it is demonstrated that the algorithm preserves the general characteristics of a trajectory while transitioning a solution between the CR3BP and ephemeris models. Each transfer in this section departs a lunar polar orbit from an initial perilune altitude of 100 km and terminates with an altitude and flight path angle at Earth arrival of 121.9 km and $-5.86°$, respectively [31]. All ephemeris trajectories are computed using a Moon-centered inertial reference frame.

6.2.1 Three-Burn Transfer, $\Delta V_{tot} = 1.5$ km/s

The first set of trajectories are computed using three deterministic burns and an allowable ΔV_{tot} of 1.5 km/s. Orthogonal views of the transfer arcs appear in Figure 6.1 and an isometric view in the lunar vicinity is plotted in Figure 6.2 in which the locations of ΔV maneuvers are denoted with magenta asterisks. The Earth and Moon are plotted to scale in both figures. The purpose of these figures is to demonstrate

changes in the trajectory caused by transitioning between the CR3B and ephemeris models. In each figure, the baseline trajectory appears in blue and is computed from a previously known solution in reference [29]. The red trajectory is generated by re-converging the baseline ephemeris solution in the CR3BP. Finally, the CR3BP solution is transitioned back to the Earth-Moon-Sun ephemeris model and is depicted in green.

A comparison of the ΔV costs and times of flight for the three trajectories appears in Table 6.1. While the two ephemeris trajectories require the maximum allowable ΔV_{tot} of 1.500 km/s, the circular restricted three-body solution is computed with a ΔV_{tot} of 1.478 km/s. The difference in time of flight between the three transfers varies by up to approximately one day. Despite these differences, it is important to note that the basic characteristics of the trajectory remain the same in each of the converged solutions.

Table 6.1 Maneuver Costs and Time of Flight Comparison: Three-Burn Transfer, $\Delta V_{tot} = 1.5$ km/s

	Ephem (Baseline)	CR3BP (from Ephem Baseline)	Ephem (from CR3BP)
ΔV_1 (km/s)	0.601	0.641	0.604
ΔV_2 (km/s)	0.466	0.412	0.415
ΔV_3 (km/s)	0.433	0.425	0.481
ΔV_{tot} (km/s)	**1.500**	**1.478**	**1.500**
TOF (days)	5.57	4.64	5.04

6.2.2 Three-Burn Transfer, $\Delta V_{tot} = 1.0$ km/s

A single-parameter continuation scheme is completed in both dynamical models to reduce the total maneuver cost from 1.5 km/s to 1.0 km/s. Various views of

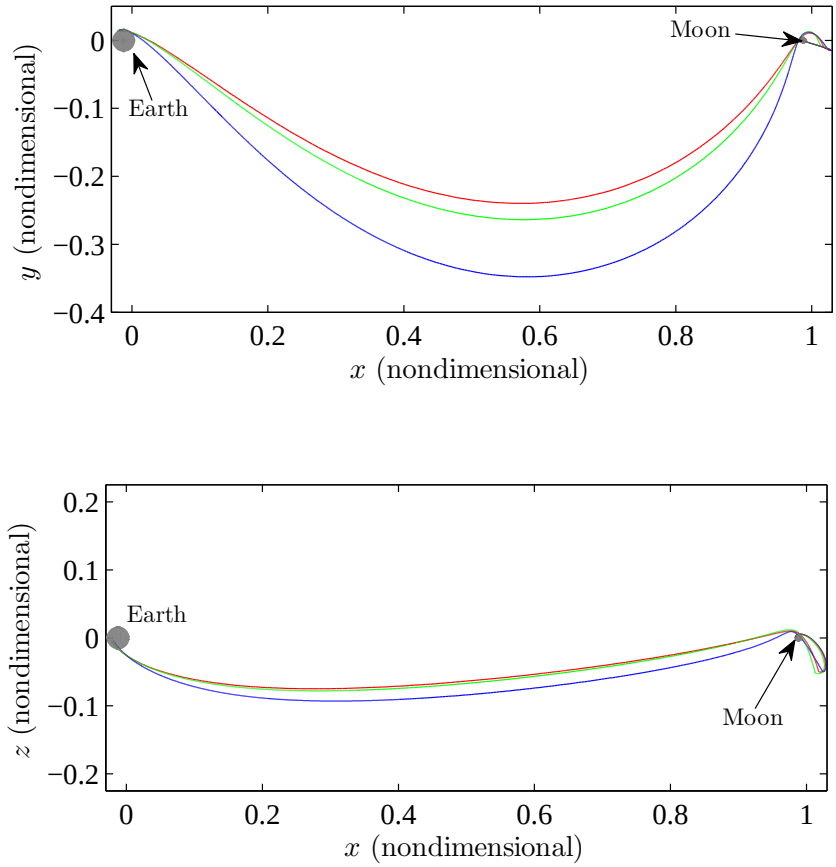

Figure 6.1. Orthogonal Views of Three-Burn Transfer, $\Delta V_{tot} = 1.5$ km/s

several three-burn trajectories with a ΔV_{tot} cost of 1.0 km/s appear in Figures 6.3 and 6.4. Beginning with the baseline solution from Section 6.2.1, the blue trajectory is computed via a continuation procedure in ΔV_{tot} in the full ephemeris model. The red trajectory is obtained by first transitioning the baseline solution to the CR3BP and then proceeding with the continuation process in that model. The converged CR3BP trajectory with a ΔV_{tot} of 1.0 km/s is simply transitioned back to the Earth-Moon-Sun ephemeris model to produce the green ephemeris trajectory.

The ΔV costs and times of flight associated with the three trajectories are compared in Table 6.2. The values in the table correspond to the transfer trajectories in Figures 6.3 and 6.4. While the total maneuver cost is the same for all three tra-

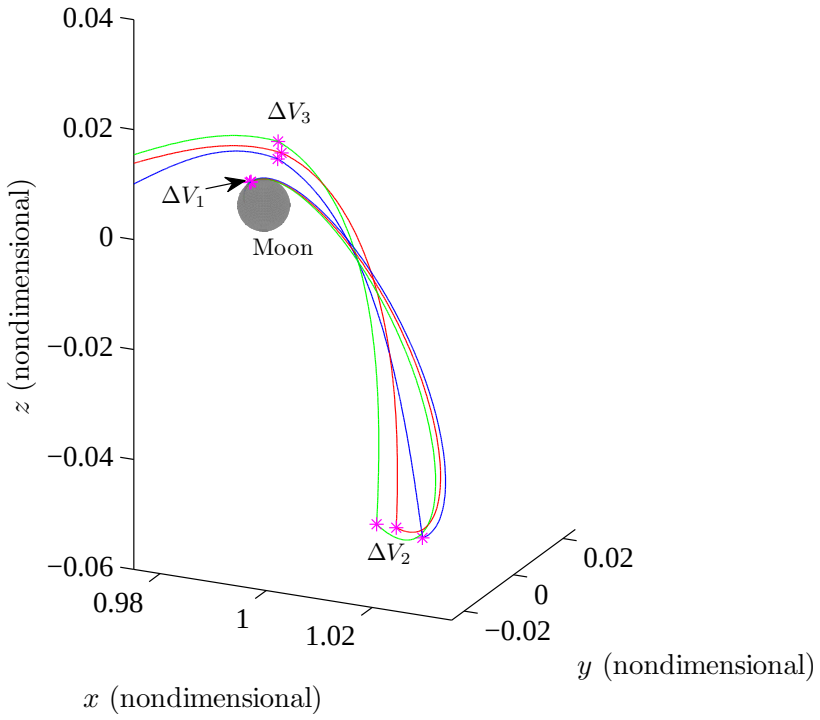

Figure 6.2. Three-Burn Transfer, $\Delta V_{tot} = 1.5$ km/s

jectories, the cost is not distributed across the three maneuvers in exactly the same way. From Figure 6.4, it is clear that the red and green trajectories possess noticeably larger apolune radii. Consequently, the deterministic plane change maneuver, ΔV_2, is smaller for these two trajectories since the maneuvers are implemented farther from the Moon. The flight time increases for these two solutions as a result. Note that the characteristics reflected in the CR3BP transfer are preserved particularly well when transitioned to the full ephemeris model.

6.2.3 Two-Burn Transfer, $\Delta V_{tot} = 1.0$ km/s

As the location of a plane change maneuver shifts away from the Moon, the influence of other gravity fields, e.g. the Earth, increase and can be exploited. In Table 6.2, it is apparent that, in the process of reducing the total maneuver cost in the

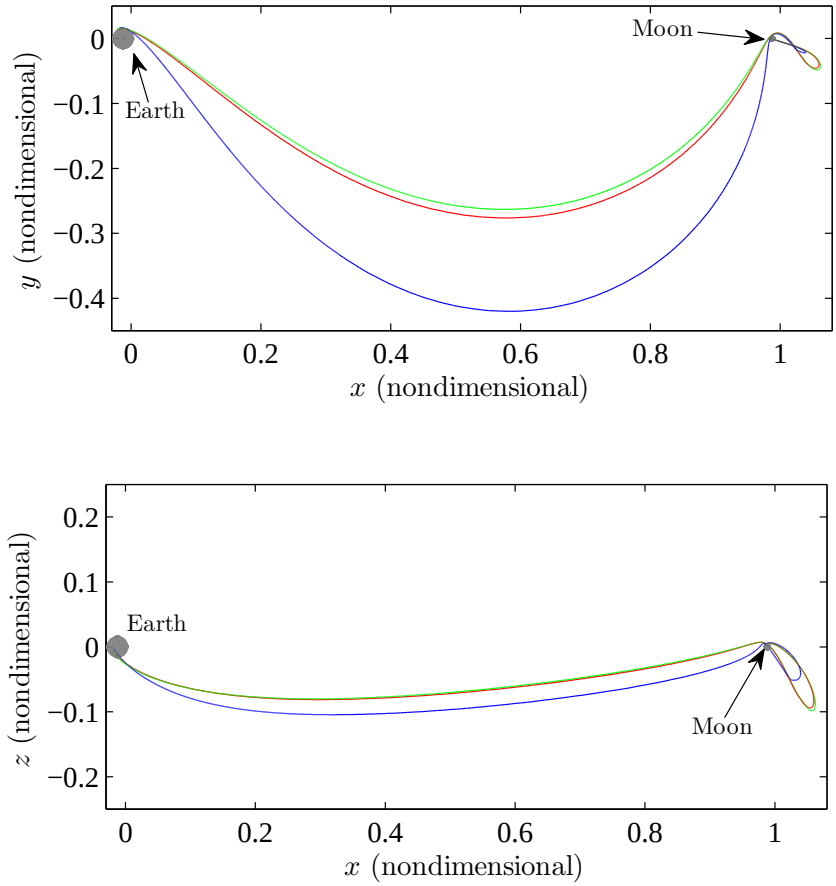

Figure 6.3. Orthogonal Views of Three-Burn Transfer, $\Delta V_{tot} = 1.0$ km/s

CR3BP case, the deterministic plane change maneuver, ΔV_2, is reduced considerably. In fact, it is sufficiently small (only 0.041 km/s) that a new solution in the CR3BP is obtainable by removing this maneuver entirely. This two-burn trajectory, with an allowable ΔV_{tot} of 1.0 km/s, appears in red in Figures 6.5 and 6.6. Transitioning this solution to a full ephemeris model produces a transfer with very similar characteristics that is depicted in green. In each case, the natural dynamics change the inclination in lieu of a deterministic maneuver. This important observation is not predicted by conventional two-body analysis.

The maneuver costs and times of flight associated with the two-burn transfers are summarized in Table 6.3. The CR3BP solution requires the entire allowable ΔV_{tot} of

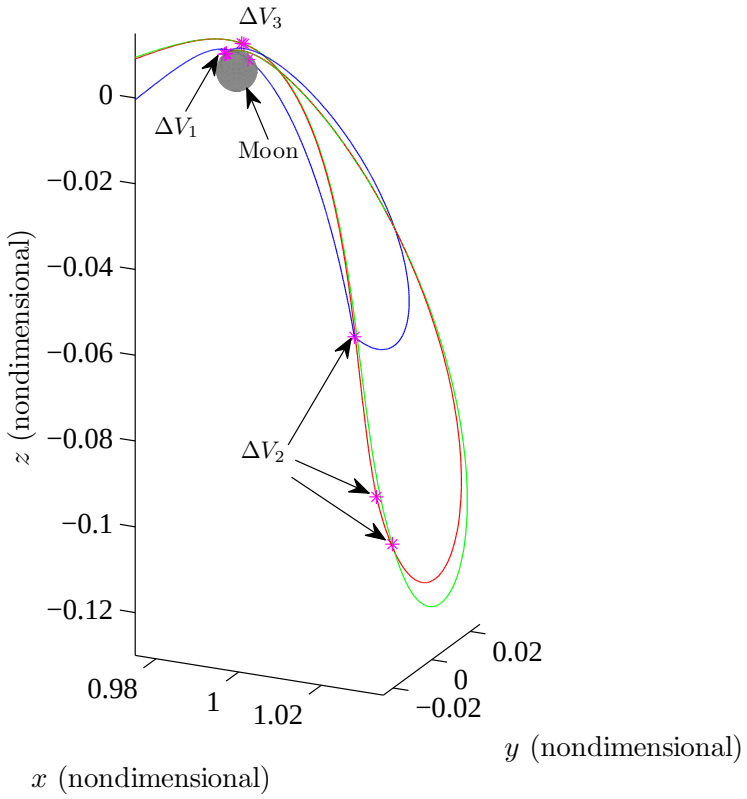

Figure 6.4. Three-Burn Transfer, $\Delta V_{tot} = 1.0$ km/s

Table 6.2 Maneuver Costs and Time of Flight Comparison: Three-Burn Transfer, $\Delta V_{tot} = 1.0$ km/s

	Ephem (Continuation)	CR3BP (Continuation)	Ephem (from CR3BP)
ΔV_1 (km/s)	0.607	0.673	0.659
ΔV_2 (km/s)	0.141	0.041	0.053
ΔV_3 (km/s)	0.252	0.285	0.288
ΔV_{tot} (km/s)	**1.000**	**1.000**	**1.000**
TOF (days)	6.62	7.65	7.63

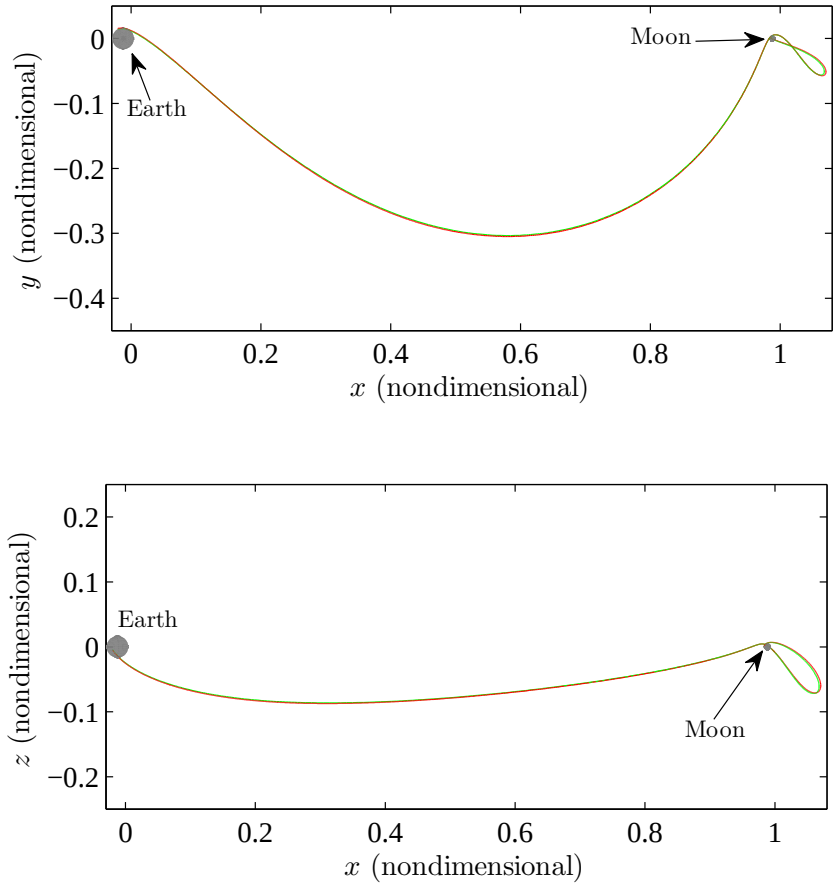

Figure 6.5. Orthogonal Views of Two-Burn Transfer, $\Delta V_{tot} = 1.0$ km/s

1.00 km/s while the ephemeris solution uses only 0.964 km/s. Both trajectories possess a time of flight that is approximately two days longer than the three-burn baseline solution. Clearly, maneuver costs are reduced at the expense of flight time. This important mission design trade-off must be carefully considered for human spaceflight missions, in particular.

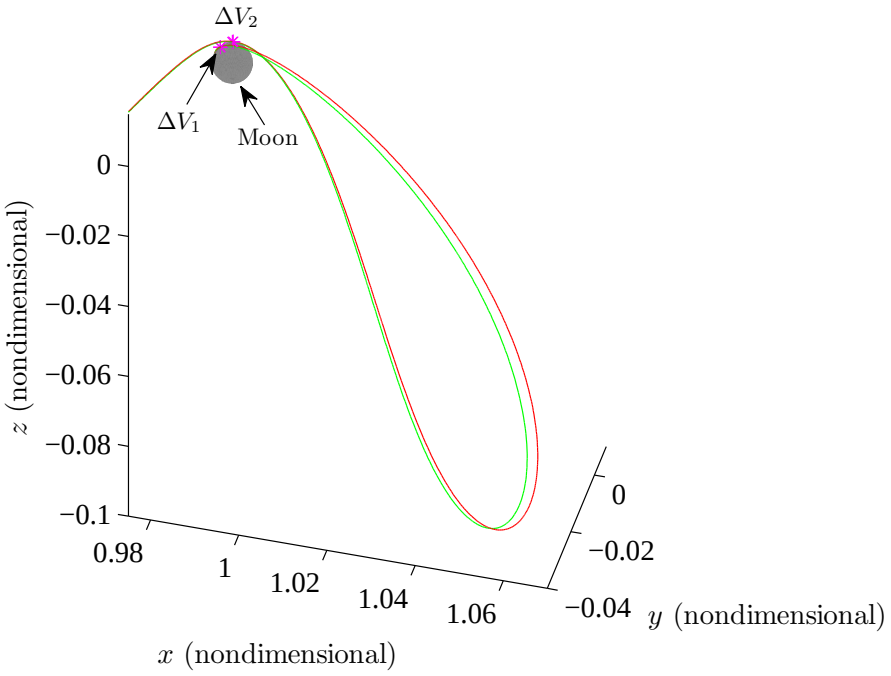

Figure 6.6. Two-Burn Transfer, $\Delta V_{tot} = 1.0$ km/s

Table 6.3 Maneuver Costs and Time of Flight Comparison: Two-Burn Transfer, $\Delta V_{tot} = 1.0$ km/s

	CR3BP (Continuation)	Ephem (from CR3BP)
ΔV_1 (km/s)	0.732	0.713
ΔV_2 (km/s)	0.268	0.251
$\boldsymbol{\Delta V_{tot}}$ **(km/s)**	**1.000**	**0.964**
TOF (days)	7.65	7.63

7. SUMMARY AND RECOMMENDATIONS

7.1 Summary

Multi-body design methodologies are introduced and applied to a variety of problems in the Earth-Moon system. Dynamical models are first developed for both the circular restricted three-body problem and a higher-fidelity N-body ephemeris model that incorporates JPL DE405 planetary ephemerides. A basic method of constraints and free variables is introduced and serves as the foundation for the numerical differential corrections algorithms that are used throughout the analysis.

The fact that the circular restricted three-body problem incorporates multiple gravity fields simultaneously makes it a powerful tool during the early stages of trajectory design. Numerical corrections procedures are developed and are implemented to target a variety of orbits in the CR3BP. Families of periodic Lyapunov and halo orbits are computed in the vicinity of the L_1 and L_2 libration points using simple shooting techniques and pseudo-arclength continuation. An intuitive method for computing quasi-periodic Lissajous orbits is presented. Earth-Moon free return trajectories are computed and combined with a bi-elliptic transfer strategy to produce a trajectory from a low Earth parking orbit to a polar lunar orbit in the CR3BP as well.

A variety of orbits are computed in a higher-fidelity ephemeris model by exploiting the versatility of multiple shooting algorithms. Select periodic and quasi-periodic libration point orbits are successfully transitioned to an Earth-Moon-Sun ephemeris model. These orbits are inherently unstable and orbit maintenance is required. A control-point stationkeeping algorithm is explored for three ephemeris orbits about the L_2 libration point, most notably the L_2 Lissajous orbit for the ARTEMIS P_1 spacecraft. Preliminary analysis indicates that the overall stationkeeping costs are

reduced significantly if four maneuvers are performed per revolution instead of two using a control-point stationkeeping strategy and a baseline orbit.

An algorithm to compute Moon-Earth transfers for manned missions to and from the lunar poles, incorporating impulsive maneuvers, is also developed using multiple shooting in an ephemeris model. Single-parameter continuation is used to reduce the total maneuver cost for a baseline three-burn transfer. An innovative two-burn transfer scheme that does not emerge using only analytical two-body techniques is determined as well. Most importantly, it is demonstrated that the characteristics of solutions designed within the context of the circular restricted-three body problem are well-maintained when the trajectories are transitioned to an ephemeris model. Thus, the CR3BP is a valuable tool during the preliminary design phases for missions in multi-body regimes.

7.2 Recommendations for Future Work

This analysis is only preliminary and there are many avenues to further explore with regard to mission design in the Earth-Moon system. At present, no spacecraft has been inserted into an Earth-Moon libration point orbit; also, the last manned lunar mission occurred nearly 40 years ago so it is anticipated that interest in the Earth-Moon regime will continue to increase.

An overarching goal is to gain a better understanding of the overall dynamical environment in the lunar vicinity. The gravitational influence of the Earth, Moon, and Sun can all significantly impact a trajectory near the Moon and taking advantage of these simultaneous effects can dramatically increase the number of mission design options available. In the libration point stationkeeping problem, the problem of transitioning from a libration point orbit to end-of-life lunar orbits is in need of further study. In the Earth-Moon transfer problem, the current analysis is rooted primarily in two-body analysis, but it seems likely, however, that new mission design options are possible if the multi-body dynamics can be exploited.

More specifically, it has been demonstrated that path constraints can be applied via a differential corrections procedure to restrict a spacecraft to a specific region of space [45]. By establishing a bounding box near a collinear libration point, it may be possible to simplify libration point orbit stationkeeping strategies using multiple shooting techniques. Additionally, such constraints may also aid in the elimination of the reliance on a baseline solution for missions such as ARTEMIS whose sole objective is to maintain an orbit in the general vicinity of a libration point for as long as fuel allows.

Improvements to the differential corrections algorithms used to determine manned Moon-Earth return trajectories can be made as well. Alternative computational schemes may offer advantages over the explicit integration scheme in the present analysis. Additionally, by better understanding the general dynamical structure in the Earth-Moon vicinity – including the impact of solar gravity – it is possible that solutions can be rapidly generated in the CR3BP and then transitioned to an ephemeris model as part of an automated, onboard corrections algorithm.

LIST OF REFERENCES

LIST OF REFERENCES

[1] W. E. Burrows, *This New Ocean: The Story of the First Space Age*. Random House, Inc., 1st ed., 1998.

[2] V. Sundararajan, "Strategic Perspectives and Technical Architecture Overview of Indian Space Exploration Missions," Paper No. AIAA-2010-973, *48th AIAA Aerospace Sciences Meeting Including the New Horizons Forum and Aerospace Exposition*, Orlando, Florida, January 4-7, 2010.

[3] A. Christensen, H. Eller, J. Reuter, and L. Sollitt, "Ice on the Moon? Science Design of the Lunar Crater Observation and Sensing Satellite (LCROSS) Mission," Paper No. AIAA-2006-7421, *Space 2006*, San Jose, California, September 19-21, 2006.

[4] R. W. Farquhar, "The Flight of ISEE-3/ICE: Origins, Mission history, and a Legacy," Paper No. AIAA-1998-4464, *AIAA/AAS Astrodynamics Specialist Conference and Exhibit*, Boston, Massachusetts, August 10-12, 1998.

[5] H. Franz, P. Sharer, K. Ogilvie, and M. Desch, "WIND Nominal Mission Performance and Extended Mission Design," Paper No. AIAA-1998-4467, *AIAA/AAS Astrodynamics Specialist Conference and Exhibit*, Boston, Massachusetts, August 10-12, 1998.

[6] C. E. Roberts and R. Short, "Injection Contingency Recovery Strategies for Halo Orbit Transfer Trajectories," Paper No. AIAA-1996-3600, *AIAA/AAS Astrodynamics Conference*, San Diego, California, July 29-31, 1996.

[7] P. Sharer and T. Harrington, "Trajectory optimization for the ACE Halo Orbit Mission," Paper No. AIAA-1996-3601, *AIAA/AAS Astrodynamics Conference*, San Diego, California, July 29-31, 1996.

[8] F. Markley, S. Andrews, J. O'Donnell, and D. Ward, "The Microwave Anisotropy Probe (MAP) Mission," Paper No. AIAA-2002-4578, *AIAA Guidance, Navigation, and Control Conference and Exhibit*, Monterey, California, August 5-8, 2002.

[9] M. W. Lo, B. G. Williams, W. E. Bollman, D. Han, Y. Hahn, J. L. Bell, E. A. Hirst, R. A. Corwin, P. E. Hong, K. C. Howell, B. T. Barden, and R. S. Wilson, "Genesis Mission Design," Paper No. AIAA-1998-4468, *AIAA/AAS Astrodynamics Specialist Conference and Exhibit*, Boston, Massachusetts, August 10-12, 1998.

[10] J. Mather, "James Webb Space Telescope," Paper No. AIAA-2004-5985, *Space 2004 Conference and Exhibit*, San Diego, California, September 28-30, 2004.

[11] M. Woodard, D. Folta, and D. Woodfork, "ARTEMIS: The First Mission to the Lunar Libration Points," *21st International Symposium on Space Flight Dynamics*, Toulouse, France, September 28-October 2, 2009.

[12] V. Angelopoulos, "The THEMIS Mission," *Space Science Reviews*, vol. 141, no. 1-4, pp. 5-34, December 2008.

[13] D. C. Folta, T. A. Pavlak, K. C. Howell, M. A. Woodard, and D. W. Woodfork, "Stationkeeping of Lissajous Trajectories in the Earth-Moon System with Applications to ARTEMIS," Paper No. AAS 10-113, *20th AAS/AIAA Space Flight Mechanics Meeting*, San Diego, California, February 14-17, 2010.

[14] J. Barrow-Green, *Poincaré and the Three Body Problem*, vol. 11 of *History of Mathematics*. American Mathematical Society, 1997.

[15] F. Moulton et al., *Periodic Orbits*. Washington: Carnegie Institution of Washington, 1920.

[16] V. Szebehely, *Theory of Orbits: The Restricted Problem of Three Bodies*. New York: Academic Press, 1967.

[17] R. Farquhar, "The Utilization of Halo Orbits in Advanced Lunar Operations," NASA X-551-70-449, GSFC, Greenbelt, Maryland, 1970.

[18] J. V. Breakwell, A. A. Kamel, and M. J. Ratner, "Station-Keeping for a Translunar Communications Station," *Celestial Mechanics*, vol. 10, no. 3, pp. 357–373, 1974.

[19] C. Simó, G. Gómez, J. Libre, R. Martínez, and J. Rodríguez, "On the Optimal Station Keeping Control of Halo Orbits," *Acta Astonautica*, vol. 15, no. 6/7, pp. 391–197, 1987.

[20] K. C. Howell and T. M. Keeter, "Station-Keeping Strategies for Libration Point Orbits: Target Point and Floquet Mode Approaches," *Proceedings of the AAS/AIAA Spaceflight Mechanics Conference 1995*, Advances in the Astronautical Sciences, Vol. 89, R. Proulx, J. Liu, P. Seidelmann, and S. Alfano (editors), 1995, pp. 1377-1396.

[21] G. Gómez, J. J. Masdemont, and C. Simó, "Quasihalo Orbits Associated with Libration Points," *Journal of the Astronautical Sciences*, vol. 46, no. 2, pp. 135–176, 1998.

[22] L. Janes and M. Beckman, "Stationkeeping Maneuvers for James Webb Space Telescope," *Goddard Flight Mechanics Symposium*, 2005.

[23] D. J. Grebow, M. T. Ozimek, K. C. Howell, and D. C. Folta, "Mutlibody Orbit Architectures for Lunar South Pole Coverage," *Journal of Spacecraft and Rockets*, vol. 45, no. 2, pp. 344–358, 2008.

[24] P. Penzo, "An Analysis of Free-Flight Circumular Trajectories," *Proceedings of the AIAA Astrodynamics Conference*, New Haven, Connecticut, 1963.

[25] A. Schwaniger, "Trajectories in the Earth-Moon Space with Symmetrical Free Return Properties," NASA Marshall Space Flight Center, Huntsville, Alabama, 1963.

[26] T. Gibson, "Application of the Matched Conic Model in the Study of Circumlunar Trajectories," NASA Manned Spacecraft Center, Houston, Texas, 1963.

[27] M. C. Jesick and C. A. Ocampo, "Automated Lunar Free Return Trajectory Generation," Paper No. AAS 09-192, *19th AAS/AIAA Space Flight Mechanics Meeting*, Savannah, Georgia, February 8-12, 2009.

[28] C. A. Ocampo and R. R. Saudemont, "Initial Trajectory Model for a Multi-Maneuver Moon to Earth Abort Sequence," Paper No. AAS 09-195, *19th AAS/AIAA Space Flight Mechanics Meeting*, Savannah, Georgia, February 8-12, 2009.

[29] B. G. Marchand, M. W. Weeks, C. W. Smith, and S. Scarritt, "Onboard Autonomous Targeting for the Trans-Earth Phase of Orion," *Journal of Guidance, Control, and Dynamics,* In Press, 2009.

[30] S. Scarritt, B. G. Marchand, and M. W. Weeks, "An Autonomous Onboard Targeting Algorithm Using Finite Thrust Maneuvers," Paper No. AIAA 2009-6104, *AIAA Guidance, Navigation, and Control Conference*, Chicago, Illinois, August 10-13, 2009.

[31] B. G. Marchand, S. Scarritt, T. A. Pavlak, and K. C. Howell, "Investigation of Alternative Return Strategies for Orion Trans-Earth Injection Design Options," Paper No. AAS 10-128, *20th AAS/AIAA Space Flight Mechanics Meeting*, San Diego, California, February 14-17, 2010.

[32] H. K. Khalil, *Nonlinear Systems*. Prentice Hall, 3rd ed., 2002.

[33] D. J. Grebow, "Trajectory Design in the Earth-Moon System and Lunar South Pole Coverage," PhD Thesis, School of Aeronautics and Astronautics, Purdue University, West Lafayette, Indiana, May 2010.

[34] H. B. Keller, *Numerical Solution of Two Point Boundary Value Problems*. Society for Industrial and Applied Mathematics, Philadelphia, 1976.

[35] H. B. Keller, "Numerical Solutions of Bifurcations and Nonlinear Eigenvalue Problems," in *Applications of Bifurcation Theory* (P. H. Rabinowitz, ed.), pp. 359–384, Academic Press, 1977.

[36] E. J. Doedel and V. A. Romanov, "Elemental Periodic Orbits Associated with the Libration Points in the Circular Restricted 3-Body Problem," *International Journal of Bifurcation and Chaos*, vol. 17, no. 8, 2007.

[37] D. J. Grebow, "Generating Periodic Orbits in the Circular Restricted Three-Body Problem with Applications to Lunar South Pole Coverage," M.S. Thesis, School of Aeronautics and Astronautics, Purdue University, West Lafayette, Indiana, May 2006.

[38] D. L. Richardson and N. D. Cary, "A Uniformly Valid Solution for Motion about the Interior Libration Point of the Perturbed Elliptic-Restricted Problem," Paper No. AAS 75-021, *AAIA/AAS Astrodynamics Conference*, Nassau, Bahamas, July 28-30, 1975.

[39] K. C. Howell and H. J. Pernicka, "Numerical Determination of Lissajous Trajectories in the Restricted Three-Body Problem," *Celestial Mechanics*, vol. 41, pp. 107–124, 1988.

[40] R. Farquhar and A. Kamel, "Quasi-Periodic Orbits About the Translunar Libration Point," *Celestial Mechanics*, vol. 7, pp. 458–473, 1973.

[41] Z. P. Olikara and K. C. Howell, "Computation of Quasi-Periodic Invariant Tori in the Restricted Three-Body Problem," Paper No. AAS 10-120, *20th AAS/AIAA Space Flight Mechanics Meeting*, San Diego, California, February 14-17, 2010.

[42] G. L. Condon, T. F. Dawn, R. S. Merriam, R. R. Sostaric, and C. H. Westhelle, "CEV Trajectory Design Considerations for Lunar Missions," Paper No. AAS 07-075, *30th Annual AAS Guidance and Control Conference*, Breckenridge, Colorado, February 3-7, 2007.

[43] Crew Exploration Vehicle Project, Flight Dynamics Team, "Lunar Orbit Insertion Targeting and Associated Outbound Mission Design for Luar Sortie Missions," NASA Johnson Space Center, Houston, Texas, March, 2007.

[44] F. J. Muñoz-Almaraz, E. Freire, J. Galán, E. Doedel, and A. Vanderbauwhede, "Continuation of Periodic Orbits in Conservative and Hamiltonian Systems," *Physica D: Nonlinear Phenomena*, vol. 181, no. 1-2, pp. 1-38, July 2003.

[45] M. T. Ozimek, D. J. Grebow, and K. C. Howell, "Design of Solar Sail Trajectories with Applications to Lunar South Pole Coverage," *Journal of Guidance, Control, and Dynamics*, vol. 32, no. 6, pp. 1884–1897, 2009.